The Application of Automated Perturbation Theory to Lattice QCD

Christopher John Monahan

Trinity College, Cambridge

Supervisor R.R. Horgan

Declaration

This dissertation is the result of my own work and includes nothing which is the outcome of work done in collaboration except where specifically indicated in the text. No part of this thesis has been, or is being, submitted for any degree other than that of the Doctor of Philosophy at the University of Cambridge.

Acknowledgements

Abstract

Predictions of heavy quark parameters are an integral component of precision tests of the Standard Model of particle physics. Experimental measurements of electroweak processes involving heavy hadrons provide stringent tests of Cabibbo-Kobayashi-Maskawa (CKM) matrix unitarity and serve as a probe of new physics. Hadronic matrix elements parameterise the strong dynamics of these interactions and these matrix elements must be calculated nonperturbatively.

Lattice quantum chromodynamics (QCD) provides the framework for nonperturbative calculations of QCD processes. Current lattices are too coarse to directly simulate b quarks. Therefore an effective theory, nonrelativistic QCD (NRQCD), is used to discretise the heavy quarks. High precision simulations are required so systematic uncertainties are removed by improving the NRQCD action. Precise simulations also require improved sea quark actions, such as the highly-improved staggered quark (HISQ) action. The renormalisation parameters of these actions cannot be feasibly determined by hand and thus automated procedures have been developed. In this dissertation I apply automated lattice pertubartion theory to a number of heavy quark calculations.

I first review the fundamentals of lattice QCD and the construction of lattice NRQCD. I then motivate and discuss lattice perturbation theory in detail, focussing on the tools and techniques that I use in this dissertation.

I calculate the two-loop tadpole improvement factors for improved gluons with improved light quarks. I then compute the renormalisation parameters of NRQCD. I use a mix of analytic and numerical methods to extract the one-loop radiative corrections to the higher order kinetic operators in the NRQCD action. I then employ a fully automated procedure to calculate the heavy quark energy shift at two-loops. I use this result to extract a new prediction of the mass of the b quark from lattice NRQCD simulations by the HPQCD collaboration. I also review the calculation of the radiative

corrections to the chromo-magnetic operator in the NRQCD action. This computation is the first outcome of our implementation of background field gauge for automated lattice perturbation theory.

Finally, I calculate the heavy-light currents for highly-improved NRQCD heavy quarks with massless HISQ light quarks and discuss the application of these results to nonperturbative studies by the HPQCD collaboration.

Contents

List of Tables

List of Figures

Chapter 1

Introduction and overview

Lattice quantum chromodyanmics (QCD) is the reigning approach for non-perturbative computations in QCD, the gauge theory of the strong interaction. Two other fundamental forces, the weak and electromagnetic interactions, are unified with QCD into the hugely successful Standard Model of particle physics. This theory describes the subatomic constituents of the Universe within the mathematical framework of a relativistic quantum field theory with $SU(3) \times SU(2) \times U(1)$ local gauge symmetry.

So far the Standard Model has largely withstood the challenge of experimental verification. There are, however, a number of theoretical reasons to expect the Standard Model to be an incomplete description of the fundamental degrees of freedom of the observable universe and it will almost certainly fail at energy scales near the Planck scale. One of the great projects of 21st Century theoretical physics is the understanding of possible Beyond the Standard Model (BSM) physics. An important aspect of this endeavour is a more complete understanding of QCD.

QCD exhibits two features that complicate the calculation of hadronic processes. The first is asymptotic freedom, the decreasing strength of QCD interactions as the energy scale increases. At high energies the coupling constant is much smaller than unity and is a good expansion parameter for perturbative calculations of QCD processes. At the low energies of typical hadrons, the coupling constant is too large for perturbation theory to converge and nonperturbative techniques must be used. Secondly, quark confinement ensures that quarks do not occur singly, but only in colour singlet bound states. Thus weak interaction processes cannot be measured without first disentangling the QCD dynamics of the bound states in which they occur. This too requires nonperturbative calculations.

Direct searches for new BSM particles have so far failed. The Large Hadron Collider (LHC) is now collecting data and in a few years will run

with a centre of mass energy of approximately 14 TeV. At these energies the LHC may be able to observe new particles in the TeV regime, but, despite hints of new particles at the Tevatron, no discovery has been announced. An alternative approach to uncovering BSM physics studies the effect of BSM particles on known Standard Model processes. These indirect searches require both precise experimental measurements and precise theoretical predictions from the Standard Model.

One particularly promising avenue for discovering BSM physics is the weak interaction of heavy quarks. The Cabibbo-Kobayashi-Maskawa (CKM) matrix parameterises the weak eigenstates of quarks in terms of the mixing of the mass eigenstates. In the Standard Model the CKM matrix is unitary. Deviations from unitarity may indicate new physics. Current tests of the unitarity of the CKM matrix suggest that the measurements from a wide range of observables are mutually consistent. However, the constraints on many of these processes are poorly known and the dominant uncertainties are theoretical

One of these dominant theoretical uncertainties comes from the CKM element $|V_{ub}|$, extracted from B meson decays. To compute this matrix element, nonperturbative hadronic form factors characterising the strong dynamics of the interaction must be calculated. The HPQCD collaboration has used a nonrelativistic formulation for heavy quarks on the lattice, NRQCD, to predict a value of $|V_{ub}| = (3.55 \pm 0.25 \pm 0.50) \times 10^{-3}$, where the first error is experimental and the second is theoretical [1]. This result is in good agreement with a number of other lattice calculations of comparable or larger error size, collected in [2].

Theoretical predictions of nonperturbative quantities have improved vastly over the last twenty years as a result of increased computer power and improved simulation algorithms. Calculations of 'gold-plated' hadronic quantities involving only one final state hadronic particle are now of a precision that may be compared to experiment [3]. The development and refinement of automated lattice perturbation theory has contributed considerably to the improved precision of lattice predictions. Next to leading order perturbative calculations have now been carried out for perturbative quantities in both

the light [4] and heavy quark sectors [5].

Whilst progress over the last three decades has been impressive, further work needs to be done. A recent update by the HPQCD and UKQCD collaborations [6] found good agreement between the lattice prediction and experiment results for the decay constant f_D, but a 3σ difference for f_{D_s}. Recent updates by the Fermilab/MILC collaboration [7], on the other hand, obtained good agreement with experiment for both f_D and f_{D_s} [8].

Moreover, determinations of both of the CKM matrix elements $|V_{ub}|$ and $|V_{cb}|$ from inclusive and exclusive decays are currently in tension. Recent studies of the $B \to D\tau\nu_\tau$ and $B \to D^*\tau\nu_\tau$ decays, on which some determinations of $|V_{cb}|$ are based, have suggested an almost 2σ excess above the expected Standard Model behaviour. These results, if confirmed, would hint at the presence of new BSM physics such as a charged Higgs boson [9].

The significance of these discrepancies is currently not clear, highlighting the need for continued progress in heavy quark physics on the lattice (for a review of recent B and D meson physics on the lattice, see [10]). In particular, continued improvement in the precision of lattice predictions is required to tighten the unitarity constraints on the CKM matrix.

Lattice perturbation theory will play an important role in this improvement programme. Lattice perturbation theory can be effectively employed to calculate lattice renormalisation parameters, match lattice and continuum calculations and compute the radiative corrections to lattice actions, all of which are required to further improve lattice simulation results. In this dissertation I present a number of related lattice perturbation theory calculations under the aegis of this improvement programme. I organise this dissertation as follows.

In Chapter 2 I outline the lattice formulation of QCD, first for the gauge sector and then for the fermionic sector. I briefly explore some of the problems associated with marrying light quarks and the lattice, before describing heavy quark effective theories for the lattice, and in particular lattice NRQCD.

I describe lattice perturbation theory in more detail in Chapter 3. I motivate the use of lattice perturbation theory as part of the programme to extract precise results from lattice simulations. I justify the use of lattice

3

perturbation theory with renormalisation group arguments. I introduce a number of tools used in this dissertation: the HiPPy and HPsrc implementation of automated lattice perturbation theory; twisted boundary conditions; and background field gauge.

In Chapter 4 I calculate the Landau and plaquette tadpole improvement factors. I determine these factors at one-loop and reproduce results in the literature. I then extend my calculation to the fermionic contributions at two-loops. I combine my results with data from high-β simulations carried out by Lee [11] and with results from [12] to present the first determination of the full two-loop Landau and plaquette tadpole improvement factors for Symanzik-improved gluons with ASQTad light quarks. I then calculate the one-loop corrections to the $\mathcal{O}(a^4 p^4)$ kinetic operators in the NRQCD action. I perform this calculation using both analytic and numerical integration and confirm results obtained by Müller using a fully automated procedure [13]. I also review the calculation of the one-loop correction to the chromo-magnetic operator in the NRQCD action. This calculation, undertaken by Hammant [14], is the first outcome of our implementation of background field gauge in the automated perturbation routines.

In Chapter 5 I compute the heavy quark renormalisation parameters in NRQCD for a number of different lattice NRQCD discretisations. I calculate the fermionic contributions to the two-loop heavy quark energy shift. I combine my results with data extracted from quenched high-β simulations, undertaken by Lee [11], to calculate the full two-loop energy shift. I then use this result to obtain a new prediction of the mass of the b quark from lattice NRQCD simulations by the HPQCD collaboration.

In Chapter 6 I calculate the matching coefficients for the temporal coefficient of the axial-vector and vector heavy-light currents in continuum QCD and NRQCD with massless HISQ light quarks. I confirm previous results using NRQCD with massless ASQTad light quarks as a check of my calculation. Finally, I summarise my results in Chapter 7.

Chapter 2

Lattice QCD

Lattice QCD is a natural approximation to QCD: we replace continuum spacetime with a hypercubic lattice, with quarks on the lattice sites and gluons on the link variables joining those sites. Spacetime points become lattice nodes, $x \rightarrow x_i = n_i a$, separated by lattice spacing a. For a lattice of side length L, the physical volume of the lattice is $(aL)^4$. The lattice spacing directly introduces an ultraviolet cutoff of π/a in momentum space and serves as a nonperturbative, gauge invariant regulator of the theory.

We relate the Euclidean hypercubic lattice to Minkowski spacetime by a Wick rotation of the temporal coordinate from Minkowski time, t, to Euclidean time, τ:

$$t \rightarrow -i\tau. \tag{2.1}$$

This coordinate change introduces an extra factor of i into the action,

$$S_M = \int \mathrm{d}^4 x \, _M \mathcal{L} \rightarrow S_E = i \int \mathrm{d}^4 x_E \, \mathcal{L}, \tag{2.2}$$

which in turn propagates into the path integral exponent,

$$\Gamma_M = \int \mathcal{D}\phi \, \exp(iS_M) \rightarrow \Gamma_E = \int \mathcal{D}\phi \, \exp(-S_E). \tag{2.3}$$

We can now interpret the path intergal exponent as the Boltzmann weight factor for a field configuration with Euclidean action S_E. Moreover, lattice fields are defined at only a discrete set of lattice nodes and links. Therefore we can replace the functional integral over field configurations by ordinary multidimensional integrals over the set of sites and links. Thus the expectation value of an operator O is

$$\langle O \rangle = \frac{1}{Z} \int \mathcal{D}\phi \, O e^{iS[\phi]} \rightarrow \frac{1}{Z} \int \prod_{x_i} \mathrm{d}\phi \, O e^{-S[\phi]}. \tag{2.4}$$

Here Z is the path integral normalisation factor,

$$Z = \int \mathcal{D}\phi \, e^{iS[\phi]} \rightarrow \int \prod_{x_i} \mathrm{d}\phi \, e^{-S[\phi]}. \tag{2.5}$$

With our intepretation of the path integral exponent as a Boltzmann weight factor, the path integral normalisation becomes the partition function for the theory. We can assign each field configuration a probability, $\exp(-S_E)$, and consequently quantum field theory is accessible to the powerful techniques of statistical field theory.

Most importantly, we can exploit the discrete nature of the lattice formulation to perform lattice simulations on a computer. In particular, numerical computations can take advantage of the statistical interpretation of the path integral to use Monte Carlo sampling approaches and other tools imported from statistical mechanics.

2.1 Gluons on the lattice

Our first attempt at formulating gauge fields on the lattice might proceed by simply placing the fields themselves at each lattice site. Unfortunately this method fails to preserve gauge invariance. Without gauge invariance, radiative corrections renormalise each of the quark-gluon, three-gluon and four-gluon couplings differently. Each vertex renormalisation factor would then have to be independently tuned using different physical quantities. This tuning would incur a computation cost much greater than that required to maintain gauge invariance and reduces the predictive power of the lattice theory.

Instead of transcribing the gauge fields directly onto the lattice, we build the gauge action from link variables that run between lattice sites. I denote a link variable between lattice sites x and $x + a\hat{\mu}$ as $U_\mu(x)$. The link variables are elements of the $SU(N)$ gauge group and given in terms of the gauge field, A_μ, by

$$U_\mu(x) = \mathcal{P}\left[\exp\left(iag \int_x^{x+a\hat{\mu}} \mathrm{d}z \, \tau \cdot A_\mu(z)\right)\right]. \tag{2.6}$$
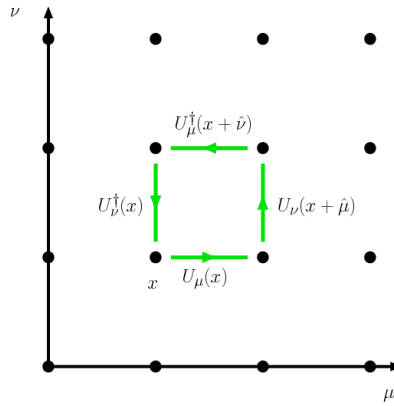
Figure 2.1: The plaquette operator, $P_{\mu\nu}(x)$.

Here $\mathcal{P}$ is the path-ordering operator, g the bare coupling constant, and τ a generator of the gauge group.

Under a gauge transformation, $\Lambda(x)$, the link variables transform as

$$U_\mu^\Lambda(x) = \Lambda(x)U_\mu(x)\Lambda^{-1}(x + a\hat{\mu}). \tag{2.7}$$

Gauge invariant quantities can thus be constructed from the trace of closed loops of link variables – Wilson loops – or from a line of link variables terminating in fermion fields at each endpoint lattice site.

Wilson's original gluon action [15] is built from closed loops of link variables, called plaquettes,

$$P_{\mu\nu}(x) = U_\mu(x)U_\nu(x + a\hat{\mu})U_\mu^\dagger(x + a\hat{\nu})U_\nu^\dagger(x). \tag{2.8}$$

The plaquette $P_{\mu\nu}$ is a one-by-one loop in the (μ, ν)-th plane, as shown in Figure 2.1. We can conveniently express the Wilson gauge action, S_G, in terms of the inverse coupling $\beta = 2N/g^2$ as

$$S_G = \beta \sum_P \left(1 - \frac{1}{2N}\text{Tr}\left[P + P^\dagger\right]\right) = \beta \sum_P \left(1 - \frac{1}{2N}\text{Re}\text{Tr}P\right). \tag{2.9}$$

This action reproduces the correct Yang-Mills action in the continuum limit. We can study the continuum limit by writing the link variables in

terms of exponentials of the gauge potential,

$$U_\mu(x) \simeq \exp\left[iag\tau \cdot A_\mu\left(x + \frac{a}{2}\hat{\mu}\right)\right], \qquad (2.10)$$

and then using the Baker-Campbell-Hausdorff formula

$$e^A e^B = e^{A+B+1/2[A,B]+1/12[A,[A,B]]+\cdots}. \qquad (2.11)$$

The derivation of the continuum action is straightforward, but slightly algebraically involved. See, for example, the detailed exposition in [16].

2.2   Light quarks on the lattice

We have now seen that we can transcribe gluon fields onto the lattice relatively easily, by replacing gauge fields with link variables. Fermionic fields do not translate to the lattice as simply. To formulate a relativistic lattice quark action our starting point is the continuum Dirac action:

$$S_D = \int d^4x\, \bar{\psi}(x)\left(i\slashed{D} - m\right)\psi(x). \qquad (2.12)$$

We can rewrite this action as a lattice quark action that reproduces the correct continuum Dirac action by directly replacing the covariant derivative with the symmetrised difference operator

$$\Delta_\mu^\pm \psi(x) = \frac{1}{2a}\left(U_\mu(x)\psi(x+\hat{\mu}) - U^\dagger\mu(x-\hat{\mu})\psi(x-\hat{\mu})\right), \qquad (2.13)$$

and introducing Euclidean gamma matrices that obey

$$\{\widehat{\gamma}_\mu, \widehat{\gamma}_\nu\} = 2\delta_{\mu\nu}. \qquad (2.14)$$

The result is

$$S_F = \sum_x \bar{\psi}(x)\left(\sum_\mu \widehat{\gamma}_\mu \Delta_\mu^+ + am\right)\psi(x). \qquad (2.15)$$

Easy! Unfortunately this is too easy. To understand why this naive action

fails, we can consider the form of the quark propagator, which is

$$G(p)^{-1} = \left(i \sum_{\mu} \widehat{\gamma}_{\mu} \sin(ap_{\mu}) + am \right). \tag{2.16}$$

Whilst $G(p)^{-1}$ reproduces the correct (Euclidean) propagator in the continuum limit within one sixteenth (in four dimensions) of the Brillouin zone, we immediately see that the presence of the $\sin(ap_{\mu})$ term introduces additional unphysical degrees of freedom. The dominant contributions to the propagator occur at the zeroes of $G(p)^{-1}$. The expected continuum-like zero occurs at $p_{\mu} = 0$, but there are also zeroes of $\sin(ap_{\mu})$ at $p_{\mu} = \pm\pi/a$. These extra contributions to the quark propagator represent 15 spurious fermion "doublers" that, even if they are projected out in external states, can still occur in virtual states by absorption of gluons with momenta $\mathcal{O}(\pi/a)$.

The presence of troublesome doublers is not a consequence of the naive choice of discretisation procedure. Doublers arise from the invariance of the fermion action under

$$\psi(x) \rightarrow \prod_{\nu} (i\widehat{\gamma}_5 \widehat{\gamma}_{\nu})^{n_{\nu}} e^{ix \cdot n\pi/a} \psi(x) \tag{2.17}$$

where $n_{\nu} = \{0, 1\}$ (see, for example, [17]). In fact, solving the doubler problem is only possible by breaking chiral symmetry [18]. Under some general assumptions about the action, such as locality and translational invariance, the Nielsen and Ninomiya no-go theorem states that it is not possible to formulate a chirally invariant and doubler-free fermion action on the lattice. This celebrated theorem is one of the principal difficulties of lattice QCD.

2.2.1 Circumventing the fermion doubling problem

A number of distinct approaches exist to combat the fermion doubling problem. Wilson's original solution was to add an irrelevant term to the action to lift the mass of the doublers to $\mathcal{O}(\pi/a)$. In the continuum limit the massive doublers decouple from the theory. Wilson's extra term introduces $\mathcal{O}(a)$ errors, which can be removed by including yet another operator of the same

dimension, the "clover" term [19]. Whilst Wilson's solution overcomes the doubling problem, it does so at the expense of explicitly breaking chiral symmetry. Preserving chiral symmetry forbids additive mass renormalisations, prevents operators with different chirality from mixing (which simplifies the calculations of matrix elements for weak interactions) and allows the Ward-Takahashi identities to be fully exploited in computations [17].

A distinct approach evades the no-go theorem by modifying the definition of chiral rotation. The usual continuum prescription for chiral transformations is $\delta\psi = i\epsilon\gamma_5\psi$, $\delta\bar{\psi} = i\epsilon\bar{\psi}\gamma_5$. The chiral symmetry of the massless Dirac operator, D, under this rotation can be expressed by $\{D, \gamma_5\} = 0$. If we redefine chiral rotation on the lattice for quark and antiquark fields as

$$\delta\psi = i\epsilon\gamma_5\left(1 - \frac{a}{2}D\right)\psi, \qquad \delta\bar{\psi} = i\epsilon\bar{\psi}\left(1 - \frac{a}{2}D\right)\gamma_5, \qquad (2.18)$$

then we can retain a remnant of the original symmetry. The operator D now satisfies the Ginsparg Wilson relation [19, 20]

$$\{D, \gamma_5\} = aD\gamma_5 D. \qquad (2.19)$$

One implementation of this relation is Neuberger's "overlap" operator [19], which necessarily preserves the modified chiral symmetry on the lattice, but at the cost of being nonlocal and consequently computationally very expensive. A second realisation extends the hypercubic lattice to five dimensions. Gauge fields are constant in the fifth dimension, whilst massless fermions of opposite chirality are bound to the four-dimensional "domain walls". Chiral symmetry breaking terms die off exponentially in the fifth dimension and the full theory reduces to an overlap-like four-dimensional effective theory as the fifth dimension grows large. This domain wall realisation is also computationally expensive and only preserves exact chiral symmetry as the size of the fifth dimension tends to infinity.

2.2.2 Staggered fermions

An alternative approach to reducing the number of doublers that does not attempt to implement an action satisfying the Ginsparg-Wilson relation is the "staggered fermion" formulation. In this approach, the fermion fields are locally transformed under

$$\psi(x) \to \Gamma(x)\chi(x), \quad \bar{\psi}(x) \to \bar{\chi}(x)\Gamma(x)^{\dagger}, \tag{2.20}$$

to give a spin-diagonalised action in terms of the four-component field $\chi(x)$. We can write the lattice action as

$$
\begin{aligned}
S &= \sum_x \bar{\chi}(x)\Gamma(x)^{\dagger}\gamma_{\mu}\Gamma(x+\hat{\mu})\left[U_{\mu}(x)\chi(x+\hat{\mu}) - U_{\mu}(x-\hat{\mu})\chi(x-\hat{\mu})\right] \\
&\quad + m\sum_x \bar{\chi}(x)\chi(x) \\
&= \sum_x \bar{\chi}(x)\alpha_{\mu}(x)\left[U_{\mu}(x)\chi(x+\hat{\mu}) - U_{\mu}(x-\hat{\mu})\chi(x-\hat{\mu})\right] + m\sum_x \bar{\chi}(x)\chi(x),
\end{aligned}
$$

where, for the choice of transformation $\Gamma(x) = \gamma_0^{x_0}\gamma_1^{x_1}\gamma_2^{x_2}\gamma_3^{x_3}$, the vector $\alpha_{\mu}(x)$ is

$$\alpha_{\mu}(x) = \begin{cases} 1 & \text{if } \mu = 0, \\ (-1)^{x_0+x_1+\cdots+x_{\mu-1}} & \text{otherwise.} \end{cases} \tag{2.21}$$

We now interpret the sixteen degrees of freedom as four copies of four-component Dirac spinors. By simulating only one component of the field we reduce the degeneracy of the degrees of freedom to only four "tastes"[1]. These tastes are not independent, but can transform into each other by exchanging high momentum gluons with momenta $\mathcal{O}(\pi/a)$ [20]. The staggered formulation has a remnant of the original chiral symmetry and the spin degrees of freedom have been been removed, leaving only colour degrees of freedom at each site. Generating gauge configurations with staggered sea quarks is therefore very cost efficient and this allows simulations to be performed near the physical light quark masses.

There are a number of formal objections to the use of staggered quarks

---

[1] An obvious kin to flavour.

as an ab initio method for calculating nonperturbatice QCD quantities. In staggered quark simulations, the remaining four tastes are removed by dividing each quark loop by four, equivalent to taking the fourth root of the quark determinant. Without taste-changing interactions this procedure is formally valid, as the determinant is block-diagonal in taste-space. However, taste-changing processes do occur and it is not yet clear if the "rooting trick" leads to a lattice action with the correct continuum limit. At finite lattice spacing rooted staggered fermions are nonlocal and not unitary.

The issues are reviewed in some detail in [21] and more recently, albeit more briefly, in [22]. Current numerical evidence, combined with some theoretical justification, seems to suggest that rooted staggered fermions have the correct continuum limit at zero temperature and chemical potential [21, 22, 23, 24]. This conclusion is far from undisputed and is unlikely to be fully resolved without progress towards a formal proof that the rooted staggered fermions have the correct physical continuum limit.

The dispute over the formal validity of rooted staggered fermions notwithstanding, staggered fermions have been widely used in precision lattice simulations (see for example, [3], [25] and [26]) and are amenable to the techniques of lattice perturbation theory. I use the staggered quark discretisation for relativistic quarks thoughout this dissertation, in Chapters 4, 5 and 6.

2.3   Improving lattice QCD

Using a lattice with finite lattice spacing to perform QCD calculations introduces discretisation errors that occur because the lattice regularisation scheme removes all momenta larger than π/a.

In principle, we could simply reduce the lattice spacing until we've decreased the errors to our desired level of precision. Unfortunately this method is currently prohibitively expensive. We must fix the physical lattice size to be larger than the correlation length of the lightest particles in the simulation or the improvement of the discretisation errors is swamped by unmanageable uncertainties from finite size effects. In general, finite size effects are estimated to be $< 1\%$ if the lattice size, L, is large enough for the pion mass

to obey $m_\pi L \geq 4$. For current lattice pion masses of ~ 300 MeV, this corresponds to lattice sizes of $L \sim 2.5$ fm. Thus we need ever-increasing lattice sizes as the continuum limit is approached. Since simulation cost scales as approximately $1/a^6$ [27, 28], this solution remains computationally unfeasible in practice.

A more sophisticated approach is to "improve" lattice actions by including new terms in the action that directly remove discretisation errors. I outline this process, generally referred to as Symanzik improvement, below.

2.3.1 Symanzik improvement

The Symanzik improvement procedure systematically removes both discretisation and cutoff errors at finite lattice spacing by adding irrelevant operators to the lattice action. These operators are arranged according to their mass dimension, using power counting rules. For example, we can remove the discretisation errors at $\mathcal{O}(a^2)$ in Wilson's gauge action by introducing operators built from six-link loops. I explain the construction of improved gauge actions in more detail in Section 2.3.3.

We replicate the high-momentum contributions removed by the lattice cutoff by adding local operators that give the same contribution to physical amplitudes as modes with momenta larger than π/a in continuum QCD [27]. These operators are nonrenormalisable but do not diverge at finite lattice spacing, because the lattice spacing serves as an ultraviolet regulator. These new terms in the lattice action are local in the sense that they are polynomials in the lattice fields and in the derivatives of the fields. We can always Taylor expand any nonlocal contributions in the external momentum, which is much less than the lattice cutoff, leaving only local interactions. Our use of local operators makes sense physically, because the additional terms correct for high momentum modes, These additional operators therefore represent highly virtual interactions, which, owing to the uncertainty principle, must be local in extent [27]. I review the construction of such a Symanzik-improved effective theory, NRQCD, in Section 2.4.1.

We fix the coupling constant for each additional operator by perturba-

tively matching the lattice theory with its continuum counterpart order-by-order in the strong coupling constant. Radiative corrections induce errors at $\mathcal{O}(\alpha_s a^2)$ and these higher order contributions modify the tree-level improvement coefficients. We can calculate these corrections using nonperturbative tuning or with lattice perturbation theory. I discuss lattice perturbation theory in greater detail in Chapter 3 and present a perturbative improvement calculation – for the kinetic operators in the NRQCD action – in Section 4.4.

2.3.2 Tadpole improvement

In an important paper from 1993, Lepage and Mackenzie [29] showed that a significant proportion of the radiative corrections to operator coefficients can be removed by dividing each link variable by its mean field value. Until the early 1990s lattice perturbation theory had been plagued by unexpectedly slow convergence. Lepage and Mackenzie demonstrated that this was a byproduct of a poor choice of expansion parameter and that by dividing the link variables by their mean field value, the convergence of lattice perturbation theory was greatly improved.

We formulate gluon actions in terms of link variables, which give rise to vertices with an arbitrary number of gluons. These vertices are suppressed by powers of the lattice spacing, but the gluon fields can be contracted together to give tadpole loops with ultraviolet divergences that precisely cancel the powers of the lattice spacing. Tadpole diagrams are therefore only suppressed by powers of the coupling constant, not the lattice spacing, and lead to large scale-independent renormalisations of lattice operators relative to their continuum counterparts.

Divergent tadpole contributions arise from the high momentum modes and are largely process independent, so we can remove these contributions by integrating out the high energy modes. We split the link variables into low momentum and high momentum modes

$$U_\mu(x) = e^{iagA_\mu(x)} \equiv e^{iag[A_\mu^{IR}(x) + A_\mu^{UV}(x)]} \rightarrow u_0 e^{iagA_\mu^{IR}(x)} \equiv u_0 \widetilde{U}_\mu(x). \quad (2.22)$$

In lattice simulations, each bare link variable in the action is divided

14

by u_0. There are a number of choices for the calculation of u_0, the only condition being that the process chosen is dominated by high momentum modes. Two common options are the expectation value of the link variable in Landau gauge or the fourth root of the plaquette. We fix the value of u_0 by requiring that the value measured in simulations agrees with the value of the parameter in the action. Unfortunately the numerical tuning that this self-consistency requires is computationally expensive. Alternatively we can use lattice perturbation theory to calculate the tadpole factor to a given order in the coupling constant. I calculate the two-loop Landau and plaquette tadpoles in Section 4.1.

Without tadpole improvement the operator renormalisations lead to large logarithmic shifts in the coupling constant. Consequently the bare lattice coupling constant is a crude choice of expansion parameter. Perturbative series convergely poorly because the bare coupling constant is anomalously small at the scales $\simeq \pi/a$ that dominate the renormalisation constants (which account for momenta excluded by the lattice cutoff). The bare lattice coupling, $\alpha_L(\pi/a)$, deviates considerably from, for example, $\alpha_{\overline{MS}}(\pi/a)$.

Instead of using the bare lattice coupling, we define an improved coupling constant. We first fix the scheme, for example the "V-scheme", defined through the heavy quark potential, and then choose a characteristic scale at which to evaluate the coupling [30]. It is natural and convenient to tie the scale to the coupling of a gluon with momentum equal to the loop momentum flowing through the graphs. Brodsky, Lepage and Mackenzie (BLM) developed a systematic procedure for determining the appropriate scale in [30], which was then extended to higher orders in [31]. I briefly discuss the BLM procedure as my work in Chapter 5 employs both the V-scheme and scale setting using the BLM procedure.

We first must choose a scheme in which to define our coupling constant. We typically choose a coupling constant defined via the heavy quark potential [29, 30]. Defining the coupling constant in terms of a physical process is equivalent to imposing a renormalisation scheme. In the $\overline{MS}$ scheme, the

heavy quark potential is [30]

$$V(q^2) = -\frac{4\pi c_f \alpha_{\overline{\mathrm{MS}}}(q)}{q^2} \left[1 + \frac{\alpha_{\overline{\mathrm{MS}}}}{\pi} \left(\frac{5}{12}\beta_0 - 2 \right) + \cdots \right]. \tag{2.23}$$

This leads naturally to a choice of scheme for defining the coupling constant: the effective potential,

$$V(q^2) \equiv -\frac{4\pi c_f \alpha_V(q)}{q^2}, \tag{2.24}$$

defines the V-scheme coupling constant, α_V, which is related to the $\overline{MS}$ scheme by $\alpha_V(q) = \alpha_{\overline{\mathrm{MS}}}(e^{-5/6}q)(1 - 2\alpha_{\overline{\mathrm{MS}}}/\pi + \cdots)$ [30]. The relation between $\alpha_{\overline{MS}}$ and α_V has been calculated to two-loops in [32, 33] and [34].

Our next task is to set the scale. At one-loop the natural choice for the scale $q^\star$ is a value that replicates the effect of a fully dressed gluon within the diagram. For a one-loop contribution, with gluon momentum q,

$$I = \alpha_V(q^\star) \int \mathrm{d}q\, f(q). \tag{2.25}$$

In the V-scheme, the apparently natural choice of $q^\star$ would be

$$\alpha_V(q*) \int \mathrm{d}q\, f(q) = \int \mathrm{d}q\, \alpha_V(q) f(q) \tag{2.26}$$

except that $\alpha_V(q)$ is singular [29, 31].

We can see why the right-hand side of Equation (2.26) diverges by considering the one-loop solution of the renormalisation group equation for the running of the coupling, which is

$$\alpha_V(q) = \frac{\alpha_V(\mu)}{1 + \alpha_V(\mu)\beta_0 \log(q^2/\mu^2)}. \tag{2.27}$$

This solution has a pole at

$$q = \Lambda_V \equiv \mu \exp\left(-\frac{1}{2\beta_0 \alpha_V(\mu)} \right). \tag{2.28}$$

This singularity arises because we are implicitly attempting to sum the

perturbative logarithms in $\alpha_V(q)$ to all-orders. Perturbative QCD is an asymptotic series, as I discuss in Section 3.2.2, and consequently it is incorrect to undertake an all-orders summation of the series. The divergence in the coupling constant can be removed by keeping only a finite number of terms in the series.

We choose $q^\star$ by setting $\mu = q^\star$ in Equation (2.27) and expanding the right-hand side to give

$$\alpha_V(q) \sim \alpha_V(q^\star) - \alpha_V^2(q^\star)\beta_0 \log\left(\frac{q^2}{(q^\star)^2}\right) + \cdots , \qquad (2.29)$$

which has solution

$$\log((q^\star)^2) = \frac{\int \mathrm{d}\, q f(q) \log(q^2)}{\int \mathrm{d}\, q} \equiv \frac{\langle f(q) \log(q^2) \rangle}{\langle f(q) \rangle}. \qquad (2.30)$$

So far this discussion has been strictly first order. There are instances in which $\langle f(q) \rangle$ vanishes or is anomalously small and $q^\star$ is undefined. Hornbostel, Lepage and Morningstar generalised the BLM method to cover such cases, which are properly second order processes and require contributions from higher moments of $f(q)$ [31]. The scale is then set by

$$\log((q^\star)^2) = \frac{\langle f \log(q^2) \rangle \pm \left[\langle f \log(q^2) \rangle^2 - \langle f \rangle \langle f \log^2(q^2) \rangle \right]^{1/2}}{\langle f \rangle}. \qquad (2.31)$$

The sign is chosen to ensure $q^\star$ is continuous and physically sensible, though it can be obtained unambiguously using higher moments [31].

I now review some of the applications of Symanzik and tadpole improvement to the gauge and light quark actions I introduce in Sections 2.1 and 2.2.2. My discussion of improved gauge actions is largely taken from [17] and [19].

2.3.3 Improved gluon actions

As I discuss in the previous section, the Wilson gauge action has discretisation errors at $\mathcal{O}(a^2)$. Gauge invariance restricts the possible operators at a given

dimension. There is one dimension four operator,

$$O^{(4)} = \sum_{\mu\nu} \text{Tr}\left(F_{\mu\nu}F_{\mu\nu}\right), \tag{2.32}$$

so the leading-order term in the expansion of the plaquette is $O^{(4)}$. There are no gauge invariant operators of dimension five, so the lattice artifacts begin at $\mathcal{O}(a^2)$. We can remove these artifacts by including dimension six operators in the gauge action. There are three operators of dimension six, which are

$$O_1^{(6)} = \sum_{\mu,\nu} \text{Tr}\left(D_\mu F_{\mu\nu} D_\mu F_{\mu\nu}\right), \tag{2.33}$$

$$O_2^{(6)} = \sum_{\mu,\nu,\rho} \text{Tr}\left(D_\mu F_{\nu\rho} D_\mu F_{\nu\rho}\right), \tag{2.34}$$

$$O_3^{(6)} = \sum_{\mu,\nu,\rho} \text{Tr}\left(D_\mu F_{\mu\rho} D_\nu F_{\nu\rho}\right). \tag{2.35}$$

On the lattice there are three six-link operators, the planar loop $\mathcal{P}_1^{(6)}$, the twisted loop $\mathcal{P}_2^{(6)}$, and the L-shaped loop $\mathcal{P}_3^{(6)}$. I show these operators in Figure 2.2. We can then write the lattice gauge action as

$$S_g = \beta\left(c^{(4)}\mathcal{L}_1^{(4)} + \sum_i c_i^{(6)}\mathcal{L}_i^{(6)}\right), \tag{2.36}$$

where $\mathcal{L}_i^{(j)} = \text{Re}\,\text{Tr}(1 - \mathcal{P}_i^{(j)})/N$ and $\mathcal{P}_1^{(4)}$ is the usual plaquette. Note that the usual convention, unlike the Wilson action, is that β is related to the bare coupling, g^2, by $\beta = 10/g^2$. At tree-level we can normalise the coefficients $c_i^{(j)}$ so that in the continuum limit the action reduces to $F_{\mu\nu}F_{\mu\nu}/4$. The normalisation condition was first obtained by Lüscher and Weisz [35, 36]:

$$c_1^{(4)} + 8c_1^{(6)} + 8c_2^{(6)} + 16c_3^{(6)} = 1. \tag{2.37}$$

We fix these coefficients by enforcing the absence of $\mathcal{O}(a^2)$ errors in, for example, the static charge potential. At tree-level, a convenient choice is the
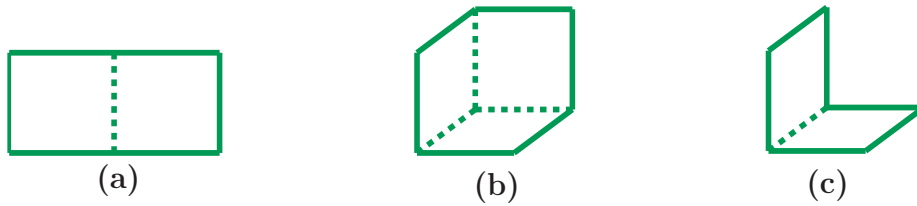
Figure 2.2: The three six-link lattice operators. From left to right: (a) the planar loop $\mathcal{P}_1^{(6)}$, (b) the twisted loop $\mathcal{P}_2^{(6)}$ and (c) the L-shaped loop $\mathcal{P}_3^{(6)}$.

"tree-level Lüscher-Weisz" action, with coefficients

$$c_1^{(4)} = 1, \qquad c_1^{(6)} = -\frac{1}{20}, \qquad c_2^{(6)} = c_3^{(6)} = 0. \tag{2.38}$$

The one-loop improvement coefficients were obtained by Lüscher and Weisz in [37] and then extended to include tadpole-improvement by Alford *et al.* in [28]. The fermionic contributions were included by Hao *et al.* using the full set of lattice perturbation theory techniques that I describe in the next chapter [38]. The unquenched tadpole-improved one-loop coefficients are

$$c_1^{(4)} = 1, \qquad c_1^{(6)} = -\frac{1}{20u_0^2}\left(1 + 0.4805\alpha_s - 0.3637(14)n_f\right) \tag{2.39}$$

$$c_2^{(6)} = -\frac{1}{u_0^2}\left(0.03325\alpha_s - 0.009(1)n_f\alpha_s\right), \qquad c_3^{(6)} = 0, \tag{2.40}$$

where n_f is the number of sea quarks.

Throughout this dissertation I use the term Symanzik-improved gluons to denote the tree-level Lüscher and Weisz action with improvement coefficients defined in Equation (2.38). The one-loop coefficients are not required for my calculations as the corresponding improvements are always at non-leading order.

2.3.4 Improved staggered quark actions

Staggered quarks suffer from taste-changing interactions that arise from the exchange of highly virtual gluons. We can suppress these high momenta processes by adding irrelevant four-quark operators to the action in much the

same way that Wilson corrected his original fermion action by adding a higher dimension operator. This method, however, is not the most efficient solution [27].

Rather than adding irrelevant operators to improve the action, we replace the simple link variables by sums of link variables over different paths, usually known as "fat link variables". This modification changes the quark-gluon coupling to suppress gluon momenta near $\mathcal{O}(\pi/a)$. A number of choices of "smearing" operators exist, but the most heavily used choice of fat link is the "Fat7" smearing [19]. Each link variable U_μ is replaced by $\mathcal{F}_\mu U_\mu$ where

$$\mathcal{F}_\mu = \prod_{\nu \neq \mu} \left(1 + \frac{a^2 \Delta_\nu^{(2)}}{4} \right) \Bigg|_{\mathrm{sym}}, \qquad (2.41)$$

and $a^2 \Delta_\nu^{(2)}$ is the lattice Laplacian acting on the link U_μ [39]. The fattened link variables now have discretisation errors at $\mathcal{O}(a^2)$, which we remove by first improving the smearing operator:

$$\mathcal{F}_\mu^{\mathrm{ASQ}} = \mathcal{F}_\mu - \sum_{\nu \neq \mu} \frac{a^2 (\Delta_\nu)^2}{4}. \qquad (2.42)$$

We must also correct the covariant derivative by including a third-order derivative

$$\Delta_\mu \to \Delta_\mu^{\mathrm{ASQ}} = \Delta_\mu^F - \frac{a^2}{6} (\Delta_\mu)^3. \qquad (2.43)$$

The additional term is usually referred to as the "Naik" term. Here the extra superscript F in Δ_μ^F indicates that the fattened link variables are used in the covariant derivative instead of the simple link variables. Tadpole improvement of the link variables leads finally to the ASQTad (a-SQuared, TADpole-improved) action [39],

$$S_{\mathrm{ASQTad}} = \sum_x \bar{\psi}(x) \left(\gamma_\mu \Delta_\mu^{\mathrm{ASQTad}} + m \right) \psi(x), \qquad (2.44)$$

where $\Delta_\mu^{\mathrm{ASQTad}}$ is the $\Delta_\mu^{\mathrm{ASQ}}$ operator with all link variables replaced by tadpole-improved links. The ASQTad action has tree-level errors at $\mathcal{O}(a^4)$

and errors at $\mathcal{O}(\alpha_s a^2)$ are strongly reduced.

The ASQTad action has been used extensively by the HPQCD and MILC collaborations; see for example [3] for a review of precision results obtained using ASQTad sea quarks. I calculate the fermionic contributions to both the two-loop tadpole improvement factor, u_0, and the heavy quark renormalisation parameters using ASQTad quarks in Chapters 4 and 5.

Whilst the ASQTad action has negligible tree-level errors for light quarks, this is not true for c quarks. Charm quarks are generally nonrelativistic in typical mesons, so the rest energy of the quark is much larger then its momentum. The dominant errors are therefore $\mathcal{O}(a^4 m^4)$. These errors can be removed by tuning the coefficient of the Naik term

$$\frac{a^2}{6}(\Delta_\mu)^3 \to \frac{a^2}{6}(1 + \epsilon)(\Delta_\mu)^3. \tag{2.45}$$

We can further reduce taste-exchange interactions by repeatedly smearing the links. One such action is the HISQ (Highly Improved Staggered Quarks) action [23], which sandwiches a reunitarisation operation, $\mathcal{U}$, between two smearing operations,

$$\mathcal{F}_\mu^{\text{HISQ}} = \mathcal{F}_\mu^{\text{ASQTad}} \mathcal{U} \mathcal{F}_\mu^{\text{ASQTad}}. \tag{2.46}$$

The reunitarisation operator projects the smeared link variables back to $SU(3)$. The resulting HISQ action is

$$S_{\text{ASQTad}} = \sum_x \bar\psi(x) \left(\gamma_\mu \Delta_\mu^{\text{HISQ}} + m \right) \psi(x), \tag{2.47}$$

where

$$\Delta_\mu^{\text{HISQ}} = \Delta_\mu \left[\mathcal{F}_\mu^{\text{HISQ}} U_\mu(x) \right] - \frac{a^2}{6}(1 + \epsilon)(\Delta_\mu)^3 \left[\mathcal{U} \mathcal{F}_\mu^{\text{HISQ}} U_\mu(x) \right]. \tag{2.48}$$

In the first derivative, the HISQ-smeared link variables are used, whilst in the second, only one-level of smearing is used.

The HISQ action is particularly suited to the simulation of charmed mesons (see, for example, [6] for some recent c quark results). HISQ smear-

ing reduces taste-splittings by approximately another factor of three. The relative simplicity and low computational cost of the HISQ action allows the simulation of sea quarks near their physical masses [6, 23, 25].

2.4 Heavy quarks on the lattice

Current HPQCD and MILC lattice simulations use physical lattice spacings from around 0.18 fm down to 0.05 fm, generally referred to as "extracoarse" and "ultrafine" respectively [22]. Unfortunately for heavy quark physics, these are too large to reliably simulate the b quark, which has a Compton wavelength of $\sim$0.01 fm. We can overcome this difficulty by introducing an effective theory for the heavy quarks that separates the long and short distance physics. Recently, the HISQ action has been used to simulate b quarks on the lattice, but this result incorporated an extrapolation up to the physical b quark mass, because simulaion at the b quark mass is not yet possible [25]. Effective theories remain the prevalent method for heavy quark physics on the lattice.

There are two commonly used effective theories: heavy quark effective theory (HQET) and nonrelativistic QCD (NRQCD). HQET requires nonperturbative renormalisation, as I discuss in greater detail in Section 3.2.2, so the role of lattice perturbation theory in HQET is very limited. In this dissertation I use the NRQCD action for perturbative calculations involving heavy quarks.

Heavy quark bound states are characterised by the small relative velocity of their constituent quarks. In heavy quarkonium bound states, such as the η_b and Υ mesons, the relative velocity is approximately $v^2 \simeq 0.1$. The relative velocity naturally induces three well-separated energy scales in heavy bound states. These are the mass, $\mathcal{O}(M)$, the momentum, $\mathcal{O}(Mv)$, and the kinetic energy, $\mathcal{O}(Mv^2)$. In NRQCD we decouple the quark and antiquark fields and then expand the quark fields using a nonrelativistic expansion. We then integrate out the high energy modes of $\mathcal{O}(M)$ to obtain an effective theory with nonrelativistic, low energy degrees of freedom. We can systematically correct discretisation and nonrelativistic errors at each order in $1/M$ by adding ir-

relevant operators to the action using power counting rules. Power counting rules are presented in detail in [40] for NRQCD and in [41] for a discretisation of NRQCD appropriate for a moving reference frame (mNRQCD).

NRQCD is not renormalisable, even at leading order, because the $\mathcal{O}(1/M)$ corrections are already included in the propagator and the non-leading terms are all higher order in the inverse heavy quark mass. There are consequently an infinite number of divergences that cannot be absorbed into the low energy constants. However, at finite lattice spacings, the theory is regularised by the lattice cutoff and the cutoff dependence of physical quantities can be reduced by including terms of sufficiently high order in the action. In practice, NRQCD simulations are restricted to a range of lattice spacings given by $1/M \lesssim a \lesssim 1/\Lambda_{QCD}$, where Λ_{QCD} is the scale parameter of QCD characterising nonperturbative behaviour.

My presentation of the derivation of the NRQCD action largely follows the development laid out in the excellent review in [40]. Historically, NRQCD was developed from nonrelativistic QED [42] by Peter Lepage and others in [43] and [44]. Improved NRQCD followed shortly after in [45], with the first full analysis of heavy quarkonium annihilation and production using improved NRQCD given in [46]. An alternative derivation of NRQCD, more suited to the extension to mNRQCD, is presented in [41] and [47].

2.4.1 Building the NRQCD action

To build NRQCD we start by constructing a nonrelativistic Lagrangian describing free quark fields. We then add interaction terms to the desired order of accuracy, using power counting rules to systematically organise the extra terms as an expansion in the relative quark velocity v.

We first decouple the quark and antiquark fields using the Foldy-Wouthuysen-Tani (FWT) transformation (see, for example, [48]). In the continuum, the lowest order action is just the nonrelativistic Schrödinger action

$$S^0 = \int \mathrm{d}^4x \, \psi^\dagger(x) \left(iD_t + \frac{D^2}{2M_Q} \right) \psi(x). \qquad (2.49)$$

One possible discretisation of the Schrödinger action is the Davies and Thacker action [49]

$$S_{\mathrm{DT}} = a^3 \sum_x \psi^\dagger(\mathbf{x}, t) \left(\Delta_4^{(+)} - \sum_{j=1}^{3} \frac{\Delta_j^{(+)} \Delta_j^{(-)}}{2aM} \right) \psi(\mathbf{x}, t), \qquad (2.50)$$

where the elementary forward and backward difference operators are

$$\Delta_\mu^+ \psi(x) = U_\mu \psi(x + a\hat{\mu}) - \psi(x), \qquad (2.51)$$

$$\Delta_\mu^- \psi(x) = \psi(x) - U_\mu^\dagger \psi(x - a\hat{\mu}). \qquad (2.52)$$

I define the link variable U_μ in Equation (2.7). Alternative discretisations are possible, such as

$$S_H = a^3 \sum_{x,t} \psi^\dagger(x) \left[\psi(\mathbf{x}, t) - U_4^\dagger(\mathbf{x}, t-1) \left(1 + H_0\right) \psi(\mathbf{x}, t-1) \right], \qquad (2.53)$$

where the leading order kinetic term is

$$H_0 = \sum_{j=1}^{3} \frac{\Delta_j^{(+)} \Delta_j^{(-)}}{2aM}. \qquad (2.54)$$

I use the Davies and Thacker action in the calculation of kinetic renormalisation coefficients outlined in Section 4.4 and derive Feynman rules for both actions in Appendix B.

So far so good. We now have a leading-order NRQCD action, S_H, which we systematically improve by specifying the desired symmetries of NRQCD. A partial list of these symmetries includes: gauge invariance; parity; rotational and translational symmetry; locality and unitarity (a more complete list is given in [40]). These symmetries severely constrain our choice of additional irrelevant operators at a given order in v. Power counting rules for NRQCD are discussed in detail in [40] and [45] (and for mNRQCD in [41]) so I will not repeat them here. Rather, I will discuss the origin of each of the correction terms in the full action, which is correct to $\mathcal{O}(a^2, v^4, 1/M^2)$.

The nonrelativistic expansion introduces relativistic errors that we can

correct by including the next-to-leading order contribution from the nonrelativistic expansion of the relativistic energy-momentum relation

$$\delta H_{\mathrm{kin}} = -c_1 \frac{(\Delta^{(2)})^2}{8a^3 M^3}, \qquad (2.55)$$

where

$$\Delta^{(2)} = \sum_{j=1}^{3} \Delta_j^{(+)} \Delta_j^{(-)}. \qquad (2.56)$$

We first need to remove the leading order discretisation errors. In principle we could reduce discretisation errors by improving $\Delta^{(2)}$ to $\widetilde{\Delta}^{(2)}$ in the leading order kinetic operator H_0, but in practise it is preferable for performance reasons to leave H_0 alone and to include this improvement in a term δH that includes all correction operators [47].

We therefore include the correction term

$$\delta H_{\mathrm{s}} = c_5 \frac{\Delta^{(4)}}{24aM} \qquad (2.57)$$

in δH. This correction removes discretisation errors up to $\mathcal{O}(a^4 p^4)$ in the spatial direction. The operator $\Delta^{(4)}$ is defined by

$$\Delta^{(4)} = \sum_{j=1}^{3} \left(\Delta_j^{(+)} \Delta_j^{(-)} \right)^2. \qquad (2.58)$$

Similarly, we improve the temporal derivative by including the correction term

$$\delta H_{\mathrm{t}} = -c_6 \frac{(\Delta^{(2)})^2}{16na^2 M^2}. \qquad (2.59)$$

Our formulation of the NRQCD action uses the fact that we are chiefly interested in onshell quantities. We can therefore use the Shrödinger equation to replace the temporal derivative with the approximate expression

$$iD_t \approx -\frac{D^2}{2aM}, \qquad (2.60)$$

through a field redefinition. This field redefinition method is a general ap-

proach applicable to all field theories and allows us to remove operators that vanish by the equations of motion.

Removing the temporal derivatives from the action using this expression greatly reduces the complexity of the numerical evaluation of quark propagators. Since the Schrödinger equation is linear in the time derivative the quark propagator obeys an evolution equation that can be specified as an initial-value problem. The initial conditions on a single timeslice of the lattice are specified and the system simply evolved time step by time step. This configuration update method is computationally far cheaper than the relativistic case. For the relativistic Dirac equation, the temporal difference operator is constrained by Hermiticity to be the symmetric forward and backward operator, which means that the evolution of the quark propagator is a boundary-value problem, requiring multiple sweeps through the lattice for each configuration update.

Finally, we include the spin-dependent terms, the "Darwin" term,

$$\delta H_{\mathrm{D}} = c_2 \frac{ig}{8a^2M^2} \left(\widetilde{\boldsymbol{\Delta}}^{(\pm)} \cdot \widetilde{\mathbf{E}} - \widetilde{\mathbf{E}} \cdot \widetilde{\boldsymbol{\Delta}}^{(\pm)} \right), \tag{2.61}$$

the "spin-orbit" interaction

$$\delta H_{\mathrm{SO}} = -c_3 \frac{g}{8a^2M^2} \sigma \cdot \left(\widetilde{\boldsymbol{\Delta}}^{(\pm)} \times \widetilde{\mathbf{E}} - \widetilde{\mathbf{E}} \times \widetilde{\boldsymbol{\Delta}}^{(\pm)} \right), \tag{2.62}$$

and the chromo-magnetic contribution,

$$\delta H_{\sigma \cdot B} = -c_4 \frac{1}{2aM} \sigma \cdot \widetilde{\mathbf{B}}. \tag{2.63}$$

The improved chromo-electric and chromo-magnetic fields are given in terms of the improved field-strength tensor by

$$\widetilde{E}_i = \widetilde{F}_{i4}, \qquad \widetilde{B}_i = -\frac{1}{2}\epsilon_{ijk}\widetilde{F}_{jk}. \tag{2.64}$$

I give an expression for the full improved field-strength tensor, taken from

[50], in Appendix A. The $\mathcal{O}(a^4 v^4)$ improved derivatives are

$$\widetilde{\Delta}_i = \Delta_i - \frac{1}{6}\Delta_j^3. \tag{2.65}$$

The δH_D, δH_{SO} and $\delta H_{\sigma \cdot B}$ corrections are the $\mathcal{O}(v^2)$ chromo-electric and chromo-magnetic interactions. The terms containing the Pauli matrices σ_i break the spin symmetry of the unimproved NRQCD actions in Equation (2.50) and (2.53), which are invariant under the $SU(2)$ mixing of the heavy quark spin components [40]. These Pauli matrix terms induce spin splittings that scale like Mv^2. Splittings of radial and orbital-angular-momentum excitations occur with the introduction of higher order $\mathcal{O}(v^4)$ correction terms [40].

Thus the fully $\mathcal{O}(a^2, v^4, 1/M^2)$-improved lattice NQRCD action is

$$S_{\mathrm{NRQCD}} = \sum_{\mathbf{x},\tau} \psi^+(\mathbf{x},\tau)\left[\psi(\mathbf{x},\tau) - \kappa(\tau)\psi(\mathbf{x},\tau-1)\right], \tag{2.66}$$

where

$$\kappa(\tau) = \left(1 - \frac{\delta H}{2}\right)\left(1 - \frac{H_0}{2n}\right)^n U_4^\dagger \left(1 - \frac{H_0}{2n}\right)^n \left(1 - \frac{\delta H}{2}\right), \tag{2.67}$$

and the δH contribution includes all interaction terms and higher order operators

$$\delta H = \delta H_{\mathrm{kin}} + \delta H_{\mathrm{s}} + \delta H_{\mathrm{t}} + \delta H_{\mathrm{D}} + \delta H_{\mathrm{SO}} + \delta H_{\sigma \cdot B}. \tag{2.68}$$

We introduce the stability parameter n to stabilise the time evolution of the propagator for small quark masses. This requires $|1 - H_0/2n| < 1$ [45] and typically I use $n = 2$ or $n = 4$ in this dissertation.

Throughout this dissertation I refer to the action in Equation (2.66), without radiative corrections to the operator coefficients, as "highly-improved NRQCD". I do not include radiative corrections in the operator coefficients in the lattice perturbation theory calculations in this dissertation because these improvements always contribute at the next order in the strong coupling constant.

2.4.2 Perturbative improvement for NRQCD

In general the operator coefficients, c_i, are free parameters of the NRQCD action. At tree-level they are equal to unity, but at higher orders they are modified by radiative corrections. The ultraviolet behaviour of NRQCD differs from QCD and so these radiative corrections will produce $\mathcal{O}(\alpha_s)$ errors in predictions of physical observables.

In principle we could tune the parameters of the action nonperturbatively, but this process is time-consuming, as it requires independent tuning for each simulation, and reduces the predictive power of the theory. For lattice NRQCD, lattice perturbation theory is a more effective way to calculate the radiative corrections.

The operator coefficients are calculated by matching an onshell quantity in NRQCD to a corresponding onshell quantity in QCD, order-by-order in the coupling constant. The general procedure for the calculation of one-loop improved operator coefficients is:

1. Calculate the one-loop radiative corrections $c_i^{\mathrm{Latt}} = 1 + \alpha c_i^{(1),\mathrm{Latt}} + \cdots$ to an onshell lattice quantity.

2. Determine the one-loop expansion of the corresponding continuum coefficients $c_i^{\mathrm{Cont}} = 1 + \alpha_s c_i^{(1),\mathrm{Cont}} + \cdots$.

3. Correct the coefficient of the operator in the lattice action by replacing

$$c_i^{\mathrm{Latt}} \rightarrow c_i^{\mathrm{Latt}} \left[1 + \alpha_s \left(c_i^{(1),\mathrm{Cont}} - c_i^{(1),\mathrm{Latt}} \right) + \cdots \right].$$

I illustrate the conceptual basis for the matching procedure schematically in Figure 2.3. There are two methods for extracting nonrelativistic operators at one-loop, corresponding to the the clockwise and counter clockwise directions indicated by the arrows. The starting point for both methods is continuum QCD in the top left.
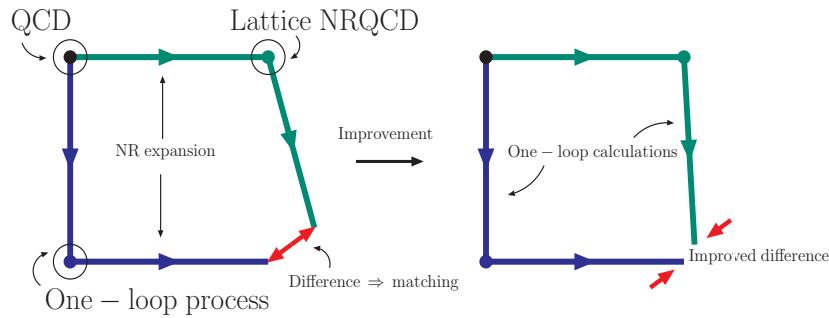
Figure 2.3: Schematic representation of the matching procedure. The starting point is continuum QCD in the top left. There are two methods for extracting nonrelativistic operators at one-loop, corresponding to the the clockwise and anticlockwise directions indicated by the arrows. I discuss each method in more detail in the text in Section 2.4.2.

Following the arrows counter clockwise, we first calculate a process at one-loop in continuum QCD. We then expand the result in a nonrelativistic expansion. The second method follows the arrows clockwise. We first expand (and discretise) the continuum QCD action to obtain lattice NRQCD. We then calculate the same process as in the first method. The two results exhibit different ultraviolet behaviour, represented by the failure of the "square" to close. By improving operators we reduce the difference between the results and bring the lattice NRQCD result, obtained via method two, closer to the continuum result. This corresponds to reducing the gap between the two methods, schematically illustrated by the "square" on the right of Figure 2.3.

In the next chapter I discuss lattice perturbation theory in more detail and introduce some of the techniques required to undertake such matching calculations.

Chapter 3

Lattice perturbation theory

3.1 Why use lattice perturbation theory?

Lattice QCD is primarily a tool for understanding the nonperturbative regime of QCD—so why develop lattice perturbation theory? Beyond serving as an explicit test of simulations in the weak-coupling regime, there are three main reasons to use lattice perturbation theory when studying heavy quark systems.

Firstly, we can use perturbative calculations to determine the renormalisation of the bare parameters of lattice actions, such as the mass and wavefunction renormalisation. The lattice serves as an ultraviolet regulator by excluding all momenta greater than π/a and therefore we can view lattice QCD as simply another regularisation scheme. The renormalised parameters of the bare lattice action can be calculated relatively easily in perturbation theory. I present this procedure in more detail for the example of the heavy quark energy shift and the mass and wavefunction renormalisations for lattice NRQCD in Chapter 5.

Secondly, lattice perturbation theory provides a method for systematically matching regularisation schemes. Experimental results are typically expressed in the Modified Minimal Subtraction ($\overline{MS}$) scheme. As with any other regularisation scheme, the effects of excluded momenta must be included via the introduction of counterterms in the lattice action.

To compare lattice simulations with experimental results, lattice parameters, such as the coupling constant and renormalisation constants, must be related to the equivalent parameters in the $\overline{MS}$ scheme. This matching process is often most easily performed perturbatively. In Chapter 5 I discuss the example of the two-loop heavy quark mass renormalisation, which relates the bare lattice mass to the $\overline{MS}$ mass. I use the mass renormalisation and heavy quark energy shift to extract a prediction of the b quark mass from

lattice NRQCD simulations. As another example, I compute the matching coefficients for heavy-light currents with NRQCD heavy quarks in Chapter 6.

Thirdly, lattice perturbation theory allows us to perturbatively improve the bare operator coefficients of the lattice action. This forms an integral part of the Symanzik improvement program, which I discuss in more detail in Section 2.3.1. For example, the lattice NRQCD actions of the previous chapter define effective theories for heavy quarks at finite lattice spacing. NRQCD is an expansion in irrelevant operators with coefficients chosen by matching to continuum QCD so that continuum results can be determined from simulations on the lattice. At tree-level, these coefficients are defined to be unity, but beyond tree-level, radiative corrections modify the coefficients and the ultraviolet behaviour of the nonrelativistic action differs from the behaviour of continuum QCD. This difference introduces $\mathcal{O}(\alpha_s)$ errors. In principle we could tune the coefficients of these additional operators nonperturbatively to reproduce the correct continuum results. In practise, however, nonperturbative tuning is time-consuming and reduces the predictive power of the lattice theory. Lattice perturbation theory is therefore often a better method for determining the lattice action parameters. In Section 4.4 I describe the improvement process for the specific case of higher order kinetic operators in the NRQCD action.

Whilst these three reasons motivate lattice perturbation theory, they do not justify its use. Lattice QCD is essentially a nonperturbative tool. We may justifiably ask: is it reasonable or appropriate to apply perturbative techniques to a nonperturbative formulation of QCD? A justification for the use of lattice perturbation theory is provided in [27]: the perturbative renormalisation factors account for the momenta excluded by the lattice cutoff. This hard ultraviolet cutoff is typically at least 6 GeV for current lattice spacings of around 0.1 fm. The coupling constant is certainly small at these energies, $\alpha_s(\pi/a) \approx 0.2$, and perturbation theory is likely to be valid. We therefore expect the effects of the excluded momenta are to be well described by perturbation theory.

In fact, we can view lattice perturbation theory as a classic example of the

application of the renormalisation group to separate the physics of different energy scales. Long distance phenomena are modelled nonperturbatively on the lattice, whilst the effects of the asymptotically free short distance modes are simply "integrated out" and rolled up into the renormalisation parameters. Lattice perturbation theory thus provides the connection between the low and high energy regimes of QCD.

3.2 Perturbation theory and renormalons

Lattice perturbation theory is not the only method for determining renormalisation parameters for lattice actions. Perturbative renormalisation can, in fact, introduce ambiguities, "renormalons", into lattice quantities. For effective theories such as HQET, nonperturbative renormalisation is required to avoid these difficulties. Before reviewing some of the tools of lattice perturbation theory that I use in this dissertation, I briefly describe some of the issues associated with renormalons and lattice perturbation theory. In particular I discuss the interplay between NRQCD, renormalons, and lattice perturbation theory.

3.2.1 Mathematical preliminaries

Renormalons are singularities in the Borel transformation of an asymptotic series [51]. If a function has the power series expansion

$$f(x) = \sum_{n=0}^{\infty} a_n x^n, \tag{3.1}$$

then we define the Borel transformation $\tilde{f}$ as

$$\tilde{f}(t) = \sum_{n=0}^{\infty} a_n \frac{t^n}{n!}. \tag{3.2}$$

Provided the Borel transform doesn't have any singularities on the real positive axis of the Borel plane (the plane of the Borel parameter t) and is

sufficiently convergent at large t, then we can recover the original function from the inverse Borel transform,

$$f(x) = \int_0^\infty \mathrm{d}t \, \exp(-t/x) \tilde{f}(t). \tag{3.3}$$

The inverse Borel transform has the same series expansion as the original function and defines the Borel sum of the original function, but is not guaranteed to exist.

If the Borel integral has singularities on the real axis, then the inverse Borel transform is not well-defined. There is no unique prescription for deforming the contour along the real axis – do we close the contour above or below the real axis? – to avoid the renormalon poles, so an inherent ambiguity in the Borel sum arises. The divergent behaviour of the original series is encoded in these singularities, referred to as renormalons. Instantons also give rise to singularities in the Borel plane, but they are higher order ambiguities in the perturbation series [52].

The contribution to the function $f(x)$ from a pole at $t = t^\star$, with residue $R^\star$, is

$$f(x) \sim -R^\star \sum_n n! \frac{x}{t^\star}^{n+1}. \tag{3.4}$$

Renormalons are therefore associated with $n!$ growth in the power series coefficients of the original function [53].

3.2.2 Renormalons and NRQCD

Perturbative QCD is generally believed to be an asymptotic series approximation to nonperturbative QCD, as first argued by Dyson [54]. Purely perturbative calculations of nonperturbative processes are therefore likely to suffer from renormalon ambiguities, though the observables themselves are of course well-defined. We may worry, then, that renormalon ambiguities may afflict lattice perturbation theory calculations. In particular, perturbative parameters, such as the pole mass, suffer from such renormalon ambiguities [55, 56] and we must be sure that we understand any subtleties involving

renormalons when extracting precise results from lattice perturbation theory. I use the pole mass in my calculation of the mass of the b quark in Chapter 5, but I prove there that any ambiguities in the pole mass must vanish in the final result.

In fact, renormalon ambiguities necessarily disappear from physical observables computed in effective field theories such as NRQCD and HQET. This was first shown by Neubert and Sachrajda [57] and Luke *et al.* [58] for HQET and for NRQCD by Bodwin and Chen [59]. The domain of integration of full QCD is split between the short-distance coefficients and the long-distance matrix elements, controlled by a ultraviolet regulator that is imposed on the matrix elements. The choice of ultraviolet regulator, which serves as a factorisation scale, is known as the "factorisation scheme". The consistency of the effective field theory ensures that observables are factorisation scale independent, provided sufficient accuracy in the effective field theory is maintained.

Bodwin and Chen observed that hard dimensionful ultraviolet regulators (for example momentum cutoff and lattice regularisations) guarantee that short-distance coefficients are infrared renormalon ambiguity free (provided, again, sufficient accuracy in the effective field theory is maintained). Correspondingly, because matrix elements are completely determined in principle by observables and short-distance coefficients, the matrix elements are renormalon ambiguity free in a cutoff-like factorisation scheme. This is consistent with the unambiguous nonperturbative definition of matrix elements in terms of Euclidean path integrals in the lattice formulation of the effective field theory. In such factorisation schemes, ultraviolet divergences appear as power dependencies on the cutoff in the matrix elements. Dimensional regularisation, on the other hand, does not guarantee the short-distance coefficients are infrared ambiguity free, as the infrared finite parts of the coefficients are integrated down to zero momentum (this point was first raised in [60] and [61]).

A hard ultraviolet cutoff introduces divergences in the matrix elements in powers of the cutoff [62]. In general we cannot subtract these divergences perturbatively as this reintroduces renormalon ambiguities. In lattice formu-

lations of HQET and NRQCD, the hard ultraviolet cutoff is provided by the inverse lattice spacing a^{-1} and the continuum limit corresponds to a diverging ultraviolet cutoff. At leading order, HQET is renormalisable, so HQET calculations usually involve extrapolation to the continuum limit. Thus the divergence of HQET matrix elements is a real issue and requires nonperturbative renormalisation of HQET for precise results. However, this argument does not apply to NRQCD. NRQCD is not renormalisable, so we do not take the continuum limit, $a \to 0$. The NRQCD matrix elements do not diverge, but are finite and scale as a known function of a^{-1}, and therefore have errors that can be quantified at a given lattice spacing.

Braaten and Chen [53] studied the large-order behaviour of the short-distance coefficients for two different quarkonium decays, $J/\psi \to e^+e^-$ and $\eta_c \to \gamma\gamma$. The renormalon ambiguities of the decay coefficients are hypothesised to cancel with corresponding ambiguities in the nonperturbative matrix elements at relative order v^2. To put this more explicitly, infrared renormalons at the Borel parameter $u = k/2$ (with k an integer) give rise to ambiguities of order $(\Lambda_{\text{QCD}}/M)^k$. Braaten and Chen hypothesised that these ambiguities can be absorbed into NRQCD matrix elements that are suppressed by v^{2k} or less. They confirmed this hypothesis for the individual cases of the $J/\psi \to e^+e^-$ and $\eta_c \to \gamma\gamma$ decays [53].

Bodwin and Chen [59] presented a method to explicitly calculate the infrared renormalon ambiguities in the NRQCD matrix elements. Combined with the results of Braaten and Chen, this explicitly demonstrated the cancellation of renormalon ambiguities in physical decay rates calculated with NRQCD [59].

Thus, whilst we should be aware that renormalon ambiguities may be present in perturbative calculations, we generally do not need to nonperturbatively renormalise NRQCD to avoid renormalon ambiguities and we are free to use lattice perturbation theory for NRQCD calculations. I now discuss some of the tools and techniques that we use in lattice perturbation theory.

3.3 The tools of lattice perturbation theory

Lattice perturbation theory is, unfortunately, rather more complicated than its continuum cousin. In principle the perturbative techniques are analogous to those in the continuum. We extract Feynman rules from the action by splitting the action into the free-field terms – quadratic in the fields – and the interacting terms – everything else. We build Feynman diagrams from these rules and evaluate them by integrating over phase space. This simple prescription rather hides the details, wherein lies the devil.

Georg von Hippel suggested that a useful "rule of thumb is that lattice perturbation theory is 'one-loop' more complicated than continuum [perturbation theory]" [63]. This statement indeed gives a fair reflection of the difficulties involved. Lattice actions are almost always considerably more complicated than continuum actions: deriving the Feynman rules by hand is rarely possible for improved actions and automation is usually required. The resulting Feynman integrals are accordingly more arduous. The lattice explicitly breaks Poincaré symmetry and consequently there are few of the handy tricks and assorted variable changes that are available to the continuum perturbation theorist. Multidimensional numerical integration is the order of the day. VEGAS, an adaptive Monte Carlo algorithm developed by Lepage [64], is particularly suited to evaluating lattice integrals.

Beyond the obstacle of extra lattice action terms, lattice perturbation theory is complicated by additional vertices with an arbitrary number of gluons. These interactions are generated by the use of link variables rather than gauge fields. Finally there are lattice artifacts arising from gauge-fixing using the Faddeev-Popov determinant and integration over the invariant Haar measure.

I now discuss the automated lattice perturbation theory routines that I use throughout this dissertation, HiPPy and HPsrc. Calculations with these routines proceed in two steps. We first extract the Feynman rules from the action using the HiPPy routines. We then construct the construct Feynman diagrams using the HPsrc routines and evaluate the resulting diagram numerically with VEGAS.

3.3.1 Automated lattice perturbation theory

Lüscher and Weisz developed the original idea for automated extraction of Feynman rules from lattice gauge actions in [65]. HiPPy is an implementation of the Lüscher-Weisz algorithm, extended to include quark actions, written in Python [66, 67]. Whilst automated methods for evaluating Feynman diagrams exist [68, 69, 70], these tend to be symbolic algebra packages, and do not generate the Feynman rules automatically. This method undoubtedly speeds up perturbative calculations, but the manual derivation of Feynman rules for highly-improved actions is cumbersome. To my knowledge, the HiPPy and HPsrc routines are the only automated lattice perturbation theory packages that allow fully automated calculations using modern, highly-improved lattice actions such as HISQ and mNRQCD.

The gauge action is built from closed loops of link variables, or "Wilson lines". We expand the link variables in powers of the bare coupling constant, g, as

$$U_{\mu>0}(x) = \exp\left(agA_\mu\left(x + \frac{a}{2}\hat{\mu}\right)\right) = \sum_{r=0}^{\infty} \frac{1}{r!}\left(agA_\mu\left(x + \frac{a}{2}\hat{\mu}\right)\right), \quad (3.5)$$

and define $U_{-\mu}(x) = U_\mu^\dagger(x - a\hat{\mu})$. By convention, the generators of the gauge field are anti-Hermitian. In momentum space the Wilson lines are given by

$$L(x, y; U) = \sum_r \frac{(ag)^r}{r!} \sum_{k_1,\mu_1,a_1} \cdots \sum_{k_r,\mu_r,a_r} \widetilde{A}_{\mu_1}^{a_1}(k_1)\ldots\widetilde{A}_{\mu_r}^{a_r}(k_r)$$
$$\times V_r(k_1, \mu_1, a_1; \ldots; k_r, \mu_r, a_r), \quad (3.6)$$

where the V_r are referred to as "vertex functions". These vertex functions are further decomposed into a matrix encoding the colour structure, C_r, and a "reduced vertex", Y_r, that depends only on the momenta and positions of the links:

$$V_r(k_1, \mu_1, a_1; \ldots; k_r, \mu_r, a_r) = C_r(a_1, \ldots, a_r)Y_r(k_1, \mu_1; \ldots; k_r, \mu_r). \quad (3.7)$$

Finally we write the reduced vertices as products of exponentials,

$$Y_r\left(k_1, \mu_1; \ldots; k_r, \mu_r\right) = \sum_{n=1}^{n_r} f_n \exp\left[\frac{i}{2}\left(k_1 \cdot v_1^{(n)} + \ldots k_r \cdot v_r^{(n)}\right)\right], \qquad (3.8)$$

where the f_n are the amplitudes associated with each term and the $v^{(n)}$ are the locations of each of the r factors of the gauge potential. Thus for each combination of r Lorentz vertices there are n_r terms, each with an associated amplitude f_n and location $v_r^{(n)}$.

Written in this form, the Feynman rules can be encoded in ordered lists of "entities", E, which have the form

$$E = \left(\mu_1, \ldots, \mu_r; x, y; v_1, \ldots, v_r; f\right). \qquad (3.9)$$

The complete set of entities at all orders in the expansion of a path is referred to as a "field", $F\{E\}$.

The reduced vertices are stored as list of entities in the "vertex file" generated by HIPPY. HIPPY generates the vertex file by repeatedly applying the convolution formulae derived in [71]. For example, for an action of the form $\psi A B \psi$, the Feynman rule for one-gluon emission is the convolution of the Feynman rules for one-gluon emission from operator A with no-gluon emission from B plus the corresponding convolution for no-gluon emission from A with one-gluon emission from B. In some cases, for very complicated actions, such as the highly-improved mNRQCD action, the convolution is performed within the HPSRC code to avoid very large vertex files, which would otherwise lead to memory leak issues.

The colour structure is handled in the HPSRC routines, when the Feynman diagrams are constructed. All derivatives can be obtained by algebraic manipulation of the reduced vertices, so no numerical derivatives are required. This avoids possible numerical instabilities that might arise when using finite derivatives to approximate derivatives and ensures the same vertex files can be used for both periodic and twisted boundary conditions. I discuss twisted boundary conditions in more detail in the next section.

I construct and evaluate all Feynman diagrams using HPSRC, a set of

FORTRAN routines described in [66, 67]. The routines build the fundamental vertices from the vertex files. For example, the function `vert_ggg(k_i,a_i)` returns the vertex function associated with the three-gluon vertex. In this case, the arguments of the routine are the set of initial and final momenta, `k_i`, and the set of colour indices, `a_i`, associated with the gluons. The function `vert_ggg` returns a `TaylUR` object, which carries the derivatives of the function with respect to the particle momenta [72, 73].

One subtlety of the HiPPy /HPsrc routines that is pertinent to the calculations in this dissertation is the inversion of the gluon propagator. The HPsrc module `vert_gg` constructs the gluon propagator by inverting the two-point function from the vertex files. In Feynman gauge, this inversion can be carried out directly. For singular gauges, such as Coulomb or Landau gauge, the two-point function is not invertible. To overcome this difficulty, an intermediate gauge correction added, the two-point function is inverted and then the correction is subtracted. The inversion routines in HPsrc can be cumbersome for a large number of iterations, so to speed up the code hardwired propagators exist for a variety of gauge actions, including Wilson and Symanzik-improved gluons. I use the hardwired propagators in my calculations of the Landau tadpole parameter in Section 4.1 and of the wavefunction renormalisation in Sections 5.1.4 and 6.3.

Finally, I evaluate the Feynman diagrams using the adaptive Monte Carlo algorithm VEGAS. VEGAS generates points in the interval $(0, 1)$ with a distribution that is inversely proportional to the magnitude of the integrand to be evaluated. Initially the distribution is uniform, and a new distribution is iteratively refined to reflect the structure of the integrand. For this algorithm to work, the integrand must be neither too peaked nor exactly uniform. These exceptions notwithstanding, the VEGAS algorithm is applicable to a very wide range of integrands. Infrared divergences in the integrand can be handled by introducing an infrared subtraction function, which I discuss in more detail in Sections 5.1 and 6.3. Alternatively, we can handle the infrared behaviour by introducing twisted boundary conditions, to which I now turn.

3.3.2 Twisted boundary conditions

The inverse lattice spacing serves as an ultraviolet regulator in lattice perturbation theory, but infrared divergences may still occur. In fact, in effective theories, such as NRQCD, the infrared divergences are guaranteed to match those in continuum QCD. In many calculations, such as the vector current matching computation of Chapter 6, we can introduce a gluon mass as an infrared cutoff. However, if there are ghost contributions, then this is no longer possible. In this case twisted boundary conditions, introduced by 't Hooft in [74] and first applied to lattice calculations in [65], can serve as an infrared regulator for lattice Feynman diagrams. For example, Hao *et al.* used twisted boundary conditions to understand the effect of including fermionic loops on the improvement coefficients of the Lüscher and Weisz gluon action (see Section 2.3.3). My presentation is mostly based on [16] and [75].

For twisted boundary conditions we replace the standard link variables with periodic boundary conditions,

$$U_\mu(x + L\hat{\nu}) = U_\mu(x), \tag{3.10}$$

with twisted link variables that satisfy

$$U_\mu(x + L\hat{\nu}) = \Omega_\nu U_\mu(x)\Omega_\nu^\dagger. \tag{3.11}$$

The twist matrices are field-independent $SU(N)$ matrices that obey

$$\Omega_1\Omega_2 = z\Omega_2\Omega_1, \tag{3.12}$$

where $z = e^{2\pi i/N}$ is an element of the centre of the group, $\mathbb{Z}(N)$. This relation only fixes the twist matrices up to a unitary transformation, which guarantees that any choice of twist results in the same physical amplitude. A second useful property of the twist matrices is that any matrix that commutes with both Ω_1 and Ω_2 is a multiple of the identity matrix.

The twisted gauge fields satisfy the same twist algebra as the twisted links. Introducing twisted link variables corresponds to expanding the gauge

fields in a new basis of twisted periodic plane waves

$$A_\mu(x) = \frac{1}{L^3 T N} \sum_k \Gamma(k) e^{ik \cdot x} e^{iak_\mu/2} \widetilde{A}_\mu(k) \qquad (3.13)$$

The $\Gamma(k)$ are complex $N \times N$ matrices in $SU(N)$ that obey the condition

$$\Omega_\nu \Gamma(k) \Omega_\nu^\dagger = e^{ik_\nu L} \Gamma(k). \qquad (3.14)$$

Condition (3.14) has a nonzero solution if

$$k_\nu = \left(\frac{2\pi}{NL}\right) n_\nu = m n_\nu. \qquad (3.15)$$

Here the twist vector n_ν is defined modulo N. We can conveniently split the momentum into an untwisted component ℓ, which is a multiple of $2\pi/L$ and a twisted component $(2\pi/NL)n_\nu$. For two twisted directions, we can write the twist vector as

$$n_\nu = (n_1, n_2, 0, 0), \qquad (3.16)$$

where n_1 and n_2 take values between 0 and $N - 1$. The gauge fields must be traceless and this imposes the condition that $(n_1, n_2) \neq (0, 0)$. Twisted boundary conditions therefore act as an infrared regulator by removing the zero momentum modes. This condition also ensures that the number of degrees of freedom is unchanged. The sum over the colour indices of the gluons, in the range $a \in [1, \ldots, N^2 - 1]$, is replaced by the sum over the $(N^2 - 1)$ possible twist vectors.

The matrices $\Gamma(k)$ depend only on the twist vector n_ν so I follow the usual convention of writing $\Gamma(k)$ as Γ_n. The general solution of Equation (3.14) is

$$\Gamma_n = c\Omega_1^{-n_2} \Omega_2^{n_1}, \qquad (3.17)$$

where c is a complex phase. There are a number of choices for the phase factor and I present them in Table 3.1.

Three useful properties that are independent of the phase factor choice

are

$$\Gamma_{n'} = \Gamma_n \quad \text{if } n'_1 = n_1 \quad \text{and} n'_2 = n_2 \pmod{N},$$
$$\Gamma_{n=0} = \mathbb{I},$$
$$\text{Tr}\Gamma_n = 0 \quad \text{unless } n = 0.$$

Two more phase-dependent properties are important: the "dagger phase" relating $\Gamma_n^\dagger$ to Γ_{-n},

$$\Gamma_n^\dagger = d_n \Gamma_{-n}, \tag{3.18}$$

and the "composition phase" defined by

$$\Gamma_{n'}\Gamma_n = z_n \Gamma_{n'+n}. \tag{3.19}$$

These phase factors may be conveniently written in terms of the symmetric and antisymmetric products

$$(n, m) \equiv n_1 m_1 + n_2 m_2 + (n_1 + m_1)(n_2 + m_2), \tag{3.20}$$
$$\langle n, m \rangle \equiv n_1 m_2 - n_2 m_1. \tag{3.21}$$

I present a number of values for the dagger and composition phases for various choices of c in Table 3.1. I updated the twisted colour factor routines in the `HPSRC` code to use the phase factor given in the bottom row of Table 3.1.

Twists can be extended to more than two directions. In general the twist matrices then satisfy

$$\Omega_\mu \Omega_\nu = z_{\mu\nu} \Omega_\nu \Omega_\mu, \tag{3.22}$$

with $z_{\mu\nu} = e^{2\pi i n_{\mu\nu}/N}$ an element of the centre of the $SU(N)$ gauge group [47]. We can also include fermionic variables by introducing an additional $SU(N)$ "smell" group. Quark fields are represented by replacing the usual $SU(N)$ spinors with $N \times N$ matrices in colour-smell space.

Automated lattice perturbation theory and twisted boundary conditions are two characteristic tools of lattice perturbation theory. Before I introduce one final piece of lattice perturbation theory machinery, background field

Phase factor c	Dagger phase d_n	Composition phase z_n
1	$z^{n_1 n_2}$	$z^{n_1 m_2}$
$z^{-n_1 n_2}$	1	$z^{-\langle n,m \rangle}$
$z^{[n_1+n_2][(n_1+n_2-1)/2]}$	$z^{-(n,n)/2}$	$z^{[\langle n,m \rangle - (n,m)]/2}$
$z^{-[n_1+n_2-n_1 n_2]/2}$	1	$z^{\langle n,m \rangle}$

Table 3.1: Phase factors for twisted boundary conditions. The first three rows are taken from [75]. I give the dagger phase (Equation (3.18)) in column two and the composition phase (Equation (3.19)) in column three. The symmetric and antisymmetric products are defined in Equations (3.20) and (3.21) respectively.

gauge, I set the scene and motivate the use of background field gauge by surveying its conceptual underpinnings, grounded in the quantum effective action.

3.4 The quantum effective action

My discussion of the quantum effective action is taken primarily from [48] and [76]. For a quantum field theory defined by the action $S[\phi]$, the complete set of vacuum-vacuum amplitudes of fields, $\phi^r(x)$, coupled to external classical currents, $J^r(x)$, is

$$Z[J] = \int \mathcal{D}\phi \, \phi \exp \left(-S[\phi] + \int \mathrm{d}^4 x \, \phi^r(x) J_r(x) \right). \qquad (3.23)$$

We relate the sum of connected vacuum-vacuum amplitudes, $W[J]$, to $Z[J]$ by

$$Z[J] = \exp \left(i W[J] \right). \qquad (3.24)$$

I denote the vacuum expectation value of the operator $\Phi^r(x)$ in the presence of a current J as $\phi_J^r(x)$. We obtain the vacuum expectation value by

functional differentiation of $W[J]$:

$$\phi_J^r(x) = \frac{\delta W[J]}{\delta J_r(x)}. \tag{3.25}$$

To define the quantum effective action, $\Gamma[\phi]$, we use the Legendre transform of $W[J]$,

$$\Gamma[\phi] = -\int \mathrm{d}^4 x\, \phi^r(x) J_{\phi_r}(x) + W[J_\phi], \tag{3.26}$$

where $J_{\phi_r}(x)$ is the current for which $\phi_J^r(x)$ has the value $\phi^r(x)$, that is

$$\phi_J^r(x) = \phi^r(x) \quad \text{if} \quad J_r(x) = J_{\phi_r}(x). \tag{3.27}$$

In the absence of external currents, the external fields are given by the stationary points of $\Gamma[\phi]$, since

$$\frac{\delta \Gamma[\phi]}{\delta \phi^r(x)} = -J_{\phi_r}(x). \tag{3.28}$$

We can conveniently express the effective action as

$$i\Gamma[\phi_0] = \int_{\mathrm{1PI}} \mathcal{D}\phi \exp\left(S[\phi + \phi_0]\right). \tag{3.29}$$

The "1PI" indicates that only one-particle irreducible connected diagrams are included in the integration. This notation is schematic. There is no way to calculate such a path integral beyond perturbation theory. If the one-particle reducible diagrams were included in the path integral then all dependence on ϕ_0 would vanish, by simple change of variable in the integration. We interpret the field ϕ_0 as a background field, conjugate to an external source.

We can calculate the functional $W[J]$ using the tree-level expansion of the vacuum-vacuum amplitude if we replace the quantum action, S, by the quantum effective action, Γ. This replacement is possible because any diagram can be constructed from a tree-level expansion of one-particle irreducible diagrams.

The quantum effective action carries all the quantum information of a quantum field theory. Therefore, when we match different effective theories,

we are interested in comparing the quantum effective action associated with each theory. If two quantum theories have the same quantum effective action, they will give the same prediction for physical processes. But what are the symmetries of the effective action?

3.4.1   Symmetries of the effective action

The symmetries of the original quantum action are also symmetries of the quantum effective action, provided the transformations are linear in the fields. Under an infinitesimal field transformation

$$\phi(x) \rightarrow \phi(x) + \epsilon F[x; \phi] \tag{3.30}$$

that leaves the original action invariant (that is, $S[\phi + \epsilon F] = S[\phi]$) the quantum effective action is invariant under the associated transformation

$$\phi(x) \rightarrow \phi(x) + \epsilon \langle F[x; \phi] \rangle_{J_\phi}. \tag{3.31}$$

The angled brackets $\langle \dots \rangle_J$ indicate the quantum average in the presence of source J. For linear transformations, we have

$$\langle F[x; \phi] \rangle_{J_\phi} = F[x; \phi], \tag{3.32}$$

so the quantum effective action is invariant under the same transformation as the original action.

Perturbative calculations require gauge-fixing. This naturally obscures the underlying gauge symmetry of the theory, which we can no longer use to constrain the form of the effective action. However, if we include new, nonlinear transformations of the ghost fields, we can preserve a reduced form of gauge symmetry in the theory – BRST invariance (named after Becchi, Rouet, Stora and Tyutin). The quantum effective action is not automatically invariant under the BRST symmetry, because of the nonlinear ghost field transformations. However, we can overcome this obstacle by introducing new

auxiliary sources, K, that couple to the BRST-transformed fields, $s * \phi$,

$$
\begin{aligned}
\exp\left(iW[J, K]\right) = \int \mathcal{D}\phi \, \exp\Big(&-S[\phi] + \int \mathrm{d}^4x \, \phi^r(x) J_r(x) \\
&+ \int \mathrm{d}^4x \, s * \phi_r(x) K_r(x) \Big)
\end{aligned}
\tag{3.33}
$$

In this form, the effective action is constrained by the Zinn-Justin equation

$$
(\Gamma, \Gamma) = 0,
\tag{3.34}
$$

where we define the Zinn-Justin anti-bracket as

$$
(F, G) = \int \mathrm{d}^4x \left(\frac{\delta F[\phi, K]}{\delta \phi^r} \frac{\delta G[\phi, K]}{\delta K^r} - \frac{\delta F[\phi, K]}{\delta K^r} \frac{\delta G[\phi, K]}{\delta \phi^r} \right).
\tag{3.35}
$$

The Zinn-Justin equation does not constrain the effective action to a simple form. However, the Zinn-Justin equation is sufficient, when coupled with power-counting arguments and various other symmetries such as Lorentz and global gauge invariance, to show that the divergent terms in the quantum effective action are related by Ward identities. These Ward identities imply that the divergent terms are in fact gauge invariant.

Furthermore, the renormalised quantum effective action, $\Gamma_R = \Gamma - \Gamma_{\mathrm{div}}$, also satisfies

$$
(\Gamma_R, \Gamma_R) = 0.
\tag{3.36}
$$

Thus Ward identities relating the renormalisation parameters will also hold for the renormalised quantum effective action. This logic reverses the usual argument, which is presented in, for example, [48]. This argument requires the renormalised quantum effective action to be repackaged in a gauge invariant manner, from which requirement we derive the Ward identities.

We obtain the renormalised quantum effective action from the original action by multiplicative field and coupling constant renormalisation. This is equivalent to the traditional view of renormalisation as adding counter-terms

to the original action. The renormalised fields are

$$A_R = Z_3^{-1/2} A_0, \quad \eta_R = \widetilde{Z}_3^{-1/2} \eta_0, \quad \overline{\eta}_R = \widetilde{Z}_3^{-1/2} \overline{\eta}_0,$$
$$\psi_R = Z_2^{-1/2} \psi_0, \quad \overline{\psi}_R = Z_2^{-1/2} \overline{\psi}_0, \quad g_R = Z_{1F}^{-1} Z_2 Z_3^{1/2}. \tag{3.37}$$

Here I denote the gauge fields by A; the quark and antiquark fields by ψ and $\overline{\psi}$ respectively; the ghost and antighost by η and $\overline{\eta}$; and the coupling constant by g. We define the renormalisation constants through the quantum effective action, which we write, before imposing Ward identities, as

$$\Gamma[A_0, \eta_0, \overline{\eta}_0] = \frac{1}{2} \mathrm{Tr} \Big(Z_3^{-1} \left(\partial_\mu A_{0\nu} - \partial_\nu A_{0\mu} \right) \left(\partial^\mu A_0^\nu - \partial_\nu A_0^\mu \right) + \lambda f^2[A_0]$$
$$- 2g Z_1^{-1} \left(\partial_\mu A_{0\nu} - \partial_\nu A_{0\mu} \right) [A_0^\mu, A_0^\nu] + g^2 Z_4^{-1} [A_{0\mu}, A_{0\nu}][A_0^\mu, A_0^\nu] \Big)$$
$$- Z_2^{-1} \overline{\psi}_0 \slashed{D} \psi_0 + g Z_{1F}^{-1} \overline{\psi}_0 \slashed{A}_0 \psi_0 - Z_m^{-1} m \overline{\psi}_0 \psi_0$$
$$+ \widetilde{Z}_3^{-1} \partial_\mu \overline{\eta}_0 \partial^\mu \eta_0 + g \widetilde{Z}_1^{-1} \partial_\mu \overline{\eta}_0^b A_0^{\mu,a} \eta_0^c f^{abc}. \tag{3.38}$$

The gauge-fixing functional in this expression is $f[A]$.

The Ward Identities for the divergent terms in the quantum effective action are

$$\frac{Z_{1F}}{Z_2} = \frac{Z_1}{Z_3} = \frac{Z_4}{Z_1} = \frac{\widetilde{Z}_1}{\widetilde{Z}_3} = \text{constant}. \tag{3.39}$$

The value of the constant is theory-dependent. In QED, the constant is equal to unity, so that only the photon field renormalisation renormalises the coupling constant g. The combination gA is automatically renormalised and we need only subtract the wavefunction renormalisation to render the quark-antiquark-gluon vertex finite.

Thus, for the case of quantum electrodynamics (QED) and nonrelativistic QED (NRQED), we can match relativistic lattice calculations with numerical NRQED calculations in the continuum limit to determine matching coefficients without ultraviolet divergences causing a problem. In QCD, however, the coupling constant is gauge dependent and the cancellation of ultraviolet divergences is not guaranteed. The extra constraints provided by background field gauge simplify such calculations in QCD.

3.4.2 Background field gauge

Background field gauge is a choice of gauge that preserves a form of gauge invariance in such a way that the divergences in the unrenormalised quantum effective action are tied together in a gauge invariant manner. This ensures that the constant in the Ward identity is equal to unity, reducing the complexity of many calculations, such as the computation of the quark-antiquark-gluon vertex renormalisation factor. In a general gauge, three independent calculations must be carried out to separate Z_{1F} from Z_1, Z_2 and Z_3, as is done, for example, in [48]. On the other hand, in background field gauge, only one renormalisation constant is required, the wavefunction renormalisation, Z_2, as demonstrated in [76].

For the particular case of NRQCD, we require background field gauge to constrain the number of operators that appear in the quantum effective action. In lattice perturbation theory, background field gauge greatly simplifies calculations such as the perturbative improvement of the chromo-magnetic operator in the NRQCD action [14], which I discuss in greater detail in Section 4.5.

In background field gauge we only require the renormalisation factor Z_3 to calculate the coupling constant renormalisation for the chromo-magnetic operator. This ensures that all the relevant diagrams are finite, since we calculate only one-particle irreducible diagrams. The continuum QCD process can therefore be calculated in any scheme, which allows us to perform the continuum calculation numerically on fine lattices. If the diagrams were not finite, then the matching calculation would introduce logarithmic terms $\log(\mu a)$ that involve the continuum regularisation scale, μ, and the lattice spacing, a.

More generally, the Zinn-Justin equation guarantees that only gauge invariant operators appear in the effective action for any operator of engineering dimension four or less. NRQCD is an expansion in irrelevant operators with dimension greater than four, so without background field gauge we cannot guarantee that we can expand the NRQCD action on a gauge invariant operator basis. In matching calculations, such as the computation of the radiative

corrections to the chromo-magnetic operator in the NRQCD action, we would need to include gauge non-invariant operators with scale-dependent logarithmic coefficients. This would seriously complicate the matching procedure.

We introduce background field gauge by decomposing the gauge fields into a smooth external source field, B, and a quantum field, q,

$$A_\mu(x) = B_\mu(x) + gq_\mu. \tag{3.40}$$

We calculate the quantum effective action $\Gamma[B, \psi, \eta, \overline{\eta}]$ by expanding the original action, $S[B + q, \psi + \psi', \eta + \eta', \overline{\eta} + \overline{\eta}']$ up to quadratic terms in the fields and integrating over the primed quantum fields.

We are free to choose the gauge-fixing function as we wish, so we take

$$f^a = D^\mu q_\mu^a, \tag{3.41}$$

where D is the background field covariant derivative,

$$D_\mu q_\nu^a = \partial_\mu q_\nu^a + f^{abc} B_\mu^b q_\nu^c. \tag{3.42}$$

We can view this gauge as parameterised by the background field, B. The gauge-fixing term, $f^a f^a$, is invariant under the formal transformation

$$\delta B_\mu^a = \partial_\mu \epsilon^a - f^{abc} \epsilon^b B_\mu^c$$
$$\delta q_\mu^a = - f^{abc} \epsilon^b q^c, \tag{3.43}$$

where ϵ parameterises the transformation. This formal transformation is not a true gauge transformation, which would not act on the classical field B. However the original action is only a functional of the sum of fields, $(B + q)$, which does transform as a true gauge transformation

$$\delta(B_\mu^a + q_\mu^a) = \partial_\mu \epsilon^a - f^{abc} \epsilon^b (B_\mu^c + q_\mu^c). \tag{3.44}$$

The sum of the matter fields, $(\psi + \psi')$, also transforms according to a true gauge transformation, so the original action is invariant under our formal

gauge transformation.

We assume the path integral measure is invariant under the formal gauge transformation and since this formal transformation is linear in the fields, the quantum effective action is also invariant. Thus we can expand the unrenormalised quantum effective action on a basis of gauge invariant operators. This is the key to the success of background field gauge. We demand gauge invariance in the quantum effective action before renormalisation and this ties the renormalisation constants together in such a way that the constant in the Ward identities expressed in Equation (3.39) is just unity. Background field gauge is the only gauge that guarantees all higher order terms are gauge invariant, which strongly restricts the number of terms that need to be included in the action. Such higher order terms are necessarily generated in an effective theory such as NRQCD.

The lattice formulation of an $SU(3)$ gauge action in background field gauge is much the same as the continuum case and was first presented in two companion papers, [77] and [78]. In the lattice formulation of lattice background field gauge, we split the link variable into the external field, $B_\mu(x)$, and the quantum field, $q_\mu(x)$ and define the link variable as

$$U_\mu(x) = e^{g_0 q_\mu(x+\hat{\mu}/2)} e^{B_\mu(x+\hat{\mu}/2)}. \tag{3.45}$$

We then build the gauge action from plaquettes as usual.

On the lattice, we replace the background field gauge covariant derivatives with lattice operators that act on (Lie algebra valued) lattice functions, $f(x)$ as

$$D_\mu f(x) = \frac{1}{a} \left\{ e^{B_\mu(x)} f(x + a\hat{\mu}) e^{-B_\mu(x)} - f(x) \right\}$$
$$D_\mu^\star f(x) = \frac{1}{a} \left\{ f(x) - e^{-B_\mu(x)} f(x - a\hat{\mu}) e^{B_\mu(x)} \right\}. \tag{3.46}$$

The full lattice QCD action in background field gauge is the sum of the usual Wilson gauge action, defined in terms of background field gauge pla-

quettes

$$S_{\mathrm{W}}^{\mathrm{BF}}[U] = \frac{1}{g_0^2} \sum_x \sum_P \mathrm{Re}\, \mathrm{Tr}\, \{1 - P_{\mu\nu}(x)\}, \tag{3.47}$$

a gauge-fixing term,

$$S_{\mathrm{GF}}^{\mathrm{BF}}[B, q] = -\lambda_0 a^4 \sum_x \mathrm{Tr}\, \left\{ D_\mu^\star q_\mu(x) D_\nu^\star q_\nu(x) \right\} \tag{3.48}$$

and the ghost contribution,

$$S_{\mathrm{FP}}^{\mathrm{BF}}[B, q, \bar{c}, c] = -2a^4 \sum_x \mathrm{Tr}\, \left\{ D_\mu \bar{c}(x) \left[J\left(g_0 q_\mu(x)\right)^{-1} D_\mu + g_0 \mathrm{Ad}[q_\mu](x) \right] c(x) \right\}. \tag{3.49}$$

In the above expressions I define the adjoint representation of a vector field X, which takes values in the Lie algebra $su(N)$, as

$$\mathrm{Ad}[X] \cdot Y = [X, Y], \tag{3.50}$$

for all Y in $su(N)$. Equivalently, in terms of the structure constants, the matrix $(\mathrm{Ad}[X])^{ab}$ associated with a given basis T^a is

$$(\mathrm{Ad}[X])^{ab} = -f^{abc} X^c \tag{3.51}$$

or

$$(\mathrm{Ad}[X] \cdot Y)^a = f^{abc} X^b Y^c. \tag{3.52}$$

The functional $J(X)$ is the exponential of the differential mapping, which we define through the linear mapping $J(X) : su(N) \mapsto su(N)$, with

$$J(X) \cdot Y = e^{-X} \frac{\mathrm{d}}{\mathrm{dt}} e^{X+tY} \Big|_{t=0} \tag{3.53}$$

for all Y in $su(N)$, and is given explicitly by

$$J(X) = 1 + \sum_{k=1}^{\infty} \frac{(-1)^k}{(k+1)!} \mathrm{Ad}[X]^k. \tag{3.54}$$

Thus the complete lattice QCD action in background field gauge is

$$S^{\mathrm{BF}}[B, q, \overline{c}, c] = S^{\mathrm{BF}}_{\mathrm{W}}[U] + S^{\mathrm{BF}}_{\mathrm{GF}}[B, q] + S^{\mathrm{BF}}_{\mathrm{FP}}[B, q, \overline{c}, c]. \qquad (3.55)$$

3.4.3 Background field gauge in HiPPy and HPsrc

We have extended the HiPPy and HPsrc code to include background field gauge [79]. This was necessary to calculate the perturbative improvement of the chromo-magnetic operator in the NRQCD action, which I discuss in greater detail in Section 4.5.

To implement background field gauge in HiPPy routines, the identification and ordering of the quantum and background fields is important. The routine `vert_ggg(k,a)` that I introduce in Section 3.3.1 now includes an additional boolean argument that specifies whether gluons are background or quantum gluons. We use the convention that the value `.TRUE.` represents background fields. Thus we specify the interaction of two background fields with a quantum field by calling the three-gluon vertex with the additional argument `bfg=(/.TRUE.,.TRUE.,.FALSE./)`, that is, we would call the function as `vert_ggg(k,a,bfg)`.

The HPsrc routines now handle the symmetrisation of the vertices separately for both background and quantum fields. The Feynman rules for background field gauge are given in the Appendix to [78] and I independently rederive them in Appendix B as part of the development of our implementation of background field gauge. The vertices with background fields have gauge-fixing terms that we have hardwired in the appropriate HPsrc vertex functions. These additions were extensively checked in the calculation of the radiative corrections to the chromo-magnetic operator in the NRQCD action.

I also hardwired the ghost and antighost vertices in background field gauge in an HPsrc module as part of our implementation of background field gauge. I present the Feynman rules for the ghost and antighost vertices in Appendix B. I extended the ghost routines to include an additional boolean argument, analogous to that of the `vert_ggg(k,a,bfg)` function. In this case, however, the argument `bfg` is a scalar. This argument is used to deter-

mine whether to implement background field gauge via a simple `IF` construct within the routine. An array is not required for the ghost and antighost vertices, because calculations planned for the foreseeable future will need vertices with either background fields or quantum fields but not both simultaneously. No vertices involving ghosts, quantum fields and background fields occur at one-loop.

We plan to reproduce the results given in the collection of papers by Lüscher and Weisz [77, 78, 80, 81] for the relation between the QCD scale parameter in the $\overline{MS}$ scheme, $\Lambda_{\overline{MS}}$, and on the lattice, Λ_L. The QCD scale parameter characterises the energy scale of the strong coupling constant. Whilst the energy dependence of the coupling constant can be determined from the renormalisation group equations, the exact value of the coupling constant at a given energy must be obtained from experimental measurements. The current world average is $\alpha_{\overline{MS}}(M_Z^0) = 0.1184(7)$, which corresponds to a four-loop scale parameter of $\Lambda_{\overline{MS}} = 213$ MeV for five flavours of sea quarks [82].

We define the beta function for a running coupling constant, $\alpha(\mu^2) = g^2(\mu)/(4\pi^2)$, that depends on the scale μ, as

$$\beta(g(\mu)) = \mu \frac{\partial g(\mu)}{\partial \mu} \tag{3.56}$$

We can write the beta function perturbatively as

$$\beta(g(\mu)) = -g^3(\mu) \sum_{n=0}^{\infty} b_n g^{2n}(\mu). \tag{3.57}$$

Here the first two coefficients for N colours and n_f fermion flavours are

$$b_0 = \frac{1}{(4\pi)^2} \left(\frac{11N}{3} - \frac{4n_f T_f}{3} \right), \tag{3.58}$$

$$b_1 = \frac{1}{(4\pi)^4} \left(\frac{34}{3} N^2 - \frac{20}{3} N T_f - 4 C_f T_f \right), \tag{3.59}$$

and the Casimir operators are $C_f = (N^2 - 1)/(2N)$ and $T_f = 1/2$ for $SU(N)$.

We then define the QCD scale parameter, Λ, by

$$\Lambda = \lim_{\mu \to \infty} \mu (b_0 g^2(\mu))^{-b_1/2b_0^2} \exp\left(-\frac{1}{2b_0 g^2(\mu)}\right). \tag{3.60}$$

The scale introduced by renormalisation, μ, and the coupling constant, g, are both scheme dependent and hence the scale parameter is also scheme dependent, but renormalisation group invariant. For example, $\Lambda_{\mathrm{MOM}}/\Lambda_{\mathrm{MS}} = 5.73$, where Λ_{MS} is the scale parameter in the minimal subtraction scheme and Λ_{MOM} is the scale parameter defined in the momentum subtraction scheme [83]. On the lattice, the scale parameter also depends on the choice of gauge and fermion actions.

We may relate the scale parameters, $\widetilde{\Lambda}$ and Λ, associated with two coupling constants, g and $\tilde{g}$, via

$$\widetilde{\Lambda} = \Lambda \exp\left(\frac{a_1}{2b_0}\right), \tag{3.61}$$

where the coefficient a_1 is the first coefficient in the expansion of $\tilde{g}$ in terms of g:

$$\tilde{g}^2 = g^2 + a_1 g^4 + \ldots \tag{3.62}$$

We can extract the coefficient a_1, and hence the ratio between the scale parameters in different regularisation schemes, from the gluon two-point function in background field gauge. In general the two-point functions are related by the gluon and ghost wavefunction renormalisations but in background field gauge the product of the renormalisation constants is unity and the two-point functions are equal, up to $\mathcal{O}(a)$ corrections.

This computation will extend my work on the Ward identities of the gluon selfenergy that I review in Appendix C and will serve as a cross-check of our implementation of background field gauge for the ghosts. This calculation is currently underway. The routines developed for this calculation can then be easily extended to include the effects of sea quarks on the ratio of the QCD scales.

I have now reviewed the machinery employed in lattice perturbation the-

ory calculations: automation, twisted boundary conditions and background field gauge. In the next three chapters I apply these techniques to several different calculations at both one- and two-loops. I first calculate the two-loop tadpole improvement factors, then the perturbative improvement of higher order kinetic coefficients the NRQCD action in Chapter 4. I calculate the heavy quark renormalisation parameters at one- and two-loops in Chapter 5 and use my two-loop results to extract a new prediction of the b quark mass from lattice NRQCD simulations. In Chapter 6 I compute the matching coefficients between heavy-light vector and axial-vector currents in continuum QCD and lattice NRQCD.

Chapter 4

Perturbative improvement

In the previous chapter I reviewed the three main reasons for developing and implementing automated lattice perturbation theory: perturbative improvement, perturbative renormalisation and operator matching. With the precision of lattice simulations now reaching the level of a few percent, the role of lattice perturbation theory in constructing highly-improved actions, and implementing them effectively in calculations, is increasingly important.

In this Chapter I apply the techniques of lattice perturbation theory to three calculations that fall under the aegis of this improvement programme. I use fully automated lattice perturbation theory to compute tadpole improvement factors to two-loops. I then employ a mixed analytic and numerical approach for the radiative corrections to higher order kinetic terms in simple NRQCD actions. Finally I review the calculation of the radiative corrections to the chromo-magnetic operator in the highly-improved NRQCD action.

4.1   Tadpole improvement

I first present my calculation of the two-loop fermionic contributions to the tadpole improvement factor, u_0, for both Landau and plaquette tadpoles. I combine my results with quenched perturbative data from [12] and from quenched high-β simulations undertaken by Lee [11] to extract the first determination of unquenched two-loop tadpole improvement factors for Symanzik-improved gluons with ASQTad light quarks.

4.2   Landau tadpoles

In Section 2.3.2 I introduce two commonly-used definitions for the tadpole improvement factor, the Landau and plaquette tadpoles. We define the Landau tadpole, u_0^L, to be the expectation value of the link operator in Landau
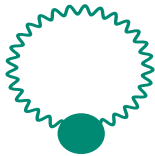
Figure 4.1: Contributions to the Landau and plaquette tadpole parameter at one-loop. Green wiggly lines indicate gluons and the large green blob represents the definition dependent part of the diagram.

gauge:

$$u_0^L = \frac{1}{N} \mathrm{Re}\, \mathrm{Tr} \langle U_\mu \rangle_{\mathrm{Landau}}. \qquad (4.1)$$

We choose Landau gauge because it is the axis-symmetric gauge that maximises the value of u_0 and therefore minimises tadpole contributions [27].

At one-loop there is a single diagram, given in Figure 4.1, that contributes to the Landau tadpole. I calculated the corresponding Feynman integral using HPSRC and evaluated the integral numerically with VEGAS. The inversion routines in HPSRC do not cope well with singular gauges, so for this calculation I used hardwired gluon propagators. However, I generated the quark propagators and quark-gluon vertices required for the two-loop contributions using HiPPy. I discuss the combined HiPPy and HPSRC implementation of automated lattice perturbation theory in more detail in Section 3.3.1.

I show the two-loop fermionic contributions in Figure 4.2. With the code for the one-loop calculation in hand, the extension to two-loops is straightforward: I replace the bare gluon propagator by the "dressed" gluon propagator, which includes the one-loop fermionic contributions. In all other respects the calculation is the same. I calculate the one-loop gluon propagator using the HPSRC module `gluon_sigma`, based on code written by Alistair Hart. I extended the module to include computation of derivatives of the selfenergy using the TaylUR derived-type [73], implemented numerical evaluation with VEGAS and compatibility with background field gauge. I made extensive use of these additions to the `gluon_sigma` module in the calculations set out in Chapter 5.

The `gluon_sigma` module evaluates the gluon selfenergy for a given set of external gluon momenta, Lorentz indices and colours. A `namelist` input

(a) (b)
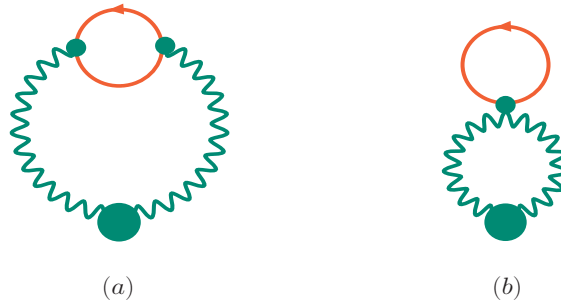
Figure 4.2: Contributions to the Landau and plaquette tadpole parameter at two-loops: (a) is the fermion "bubble" and (b) the fermion "tadpole". Green wiggly lines indicate gluons, red lines are light quarks and the large green blob represents the definition dependent part of the diagram.

selects which contributions, for example the fermion "tadpole" or "bubble" diagrams (see Figure 4.2 for notation), are included in the calculation. The full two-loop calculation is an eight-dimensional integral over the double loop momenta.

I use zero gluon mass in all calculations that I describe in this section and regulate the low momenta behaviour with the external gluon momentum, aq. I confirmed that all results were independent of the gluon momentum for a wide range of values between $aq = 0.01$ and $aq = 0.9$.

Throughout this chapter I use the convention for both Landau and plaquette tadpoles that

$$u_0 = 1 - u_0^{(2)}\alpha_L - u_0^{(4)}\alpha_L^2 - \mathcal{O}(\alpha_L^3). \tag{4.2}$$

4.2.1   Landau tadpole results

I present my results for the one- and two-loop Landau tadpole parameters in Table 4.1 for both unimproved Wilson gluons and for Symanzik-improved gluons. I obtained the one-loop results with 10^5 function evaluations and 10 VEGAS iterations, which took about five minutes wall-clock time on six processors. In this dissertation, whenever I refer to the time elapsed for a given calculation this should be understood to refer to wall-clock time and not CPU time. I carried out these calculations on the Cambridge High Performance

Figure 4.3: The Light quark mass-dependence of the two-loop Landau tadpoles. I plot the fit to a function quadratic in the light quark mass in blue. I use Symanzik-improved gluons with ASQTad light quarks. Note the small scale on the y-axis.

Computing Cluster, which consists of 2094 3.0 GHz Intel Woodcrest cores.

I calculated the two-loop contributions on 128 processors, with 10^7 function evaluations and 15 VEGAS iterations, which took approximately 2.5 hours for the unimproved fermions and five hours for the ASQTad fermions. I present results for six different light quark masses, from $am_q = 0.005$ to $am_q = 0.10$ and extrapolate these results to zero light quark mass using a function quadratic in the light quark mass. Including quartic terms did not alter the result at zero quark mass within the quoted errors. I plot my data and the quadratic fit for the light quark mass extrapolation, shown by the blue line, in Figure 4.3.

I quote uncertainties for each result that are the statistical errors from numerical integration of the Feynman diagrams, except in the massless light quark two-loop result. In this case, I give the uncertainty from the fit to the light quark mass.

I present a large number of tables of data in this dissertation and, unless otherwise stated, the uncertainties I quote for my results are the statistical errors from numerical integration.

59

Action	$u_0^{(2),L}$	am_q	$u_0^{(4),L}$	
			Unimproved	ASQTad
Wilson	0.9739(2)	0.005	-0.0703(3)	-0.1238(3)
		0.01	-0.0704(3)	-0.1238(3)
		0.03	-0.0701(3)	-0.1238(4)
		0.05	-0.0698(3)	-0.1241(6)
		0.08	-0.0692(3)	-0.1230(4)
		0.10	-0.0688(3)	-0.1226(4)
		0.20	-0.0651(3)	-0.1195(3)
		0.0	-0.070287(56)	-0.1238(1)
Symanzik	0.7503(2)	0.005	-0.0461(3)	-0.0726(3)
		0.01	-0.0460(3)	-0.0727(3)
		0.03	-0.0458(3)	-0.0725(4)
		0.05	-0.0456(3)	-0.0727(5)
		0.08	-0.0450(3)	-0.0720(3)
		0.10	-0.0447(3)	-0.0716(3)
		0.20	-0.0422(3)	-0.0694(3)
		0.0	-0.0460(1)	-0.0727(1)

Table 4.1: Landau tadpole corrections at one- and two-loops for Wilson and Symanzik-improved gluons. The two-loop results are the fermionic contributions only, with unimproved staggered light quark results presented in column four and ASQTad quarks in column five. The two-loop result at zero light quark mass result is an extrapolation; one-loop results are fermion mass independent. The uncertainties quoted are statistical errors from numerical integration, except in the massless light quark two-loop result. In this case, the uncertainty is from the fit to the light quark mass.

4.2.2   Comparison to the literature

We can compare the one-loop fermionic results given in Table 4.1 with previously published results for the Landau tadpole. In [12], Nobes *et al.* report a value of

$$u_0^L|_{n_f=0} = 1 - 0.9738(2)\alpha_L - 3.33(1)\alpha_L^2 \qquad (4.3)$$

for the quenched Landau tadpole for Wilson gluons and

$$u_0^L|_{n_f=0} = 1 - 0.7501(1)\alpha_L - 2.06\alpha_L^2 \tag{4.4}$$

for Symanzik-improved gluons. My one-loop results are in perfect agreement with the one-loop values given in [12]. In common with the quenched results, my two-loop coefficients are smaller for the Symanzik-improved action than for Wilson gluons. This is what we would expect: the improved action is designed to be more continuum-like, with smaller lattice artifacts, and hence requires less tadpole improvement.

I combine the fermionic contributions given in Table 4.1 with the two-loop quenched results in Equations (4.3) and (4.4) to present the first perturbative calculation of the unquenched Landau tadpole at two-loops. I find

$$u_0^L = 1 - 0.7503(2)\alpha_L - (2.06(1) - 0.0733(4)n_f)\,\alpha_L^2 \tag{4.5}$$

for Symanzik-improved gluons with ASQTad sea quarks of mass $am_q = 0.01$, which corresponds, for example, to the light quark mass on the MILC "fine" ensembles [84].

4.2.3   Three-loop estimate

I estimate the three-loop contribution to the Landau tadpole by subtracting the full two-loop perturbative results in Equation (4.5) from the nonperturbative Landau tadpoles measured on the MILC collaboration's ASQTad ensembles. Data for ensembles with (2+1) flavours of sea quark are presented in [84] and [85] . For the "fine" ensemble, the Landau tadpole was measured to be $u_0^L = 0.8461(1)$. This ensemble has light quark bare masses $am_{u,d} = 0.0124$, strange quark mass $am_s = 0.031$ and bare coupling $\beta = 7.09$.

I use the relation between the bare lattice coupling and the β values listed in Table 1 of [85],

$$\alpha_L = \frac{5}{2\pi\beta}, \tag{4.6}$$

to compute a value of the coupling constant. In this case I obtain $\alpha_L = 0.1122$.

Using this value of the coupling constant, I obtain

$$u_0^{(6),L}\alpha_L^3 \simeq u_0^L - \left(1 - u_0^{(2),L}\alpha_L + u_0^{(4),L}\alpha_L^2\right) = -0.057(1). \qquad (4.7)$$

My estimate of the three-loop perturbative contribution to the Landau tadpole for Symanzik-improved gluons and ASQTad light quarks is therefore

$$u_0^{(6),L} \simeq -40.4(7). \qquad (4.8)$$

In [86], Hart *et al.* found that measurements of the Landau tadpole from quenched high-β Monte Carlo simulations were well described by the two-loop Landau tadpole calculated in perturbation theory. By fitting the high-β results to a polynomial in the coupling constant, they inferred the size of the three-loop contribution to the Landau tadpole. Direct comparison with my results is not possible because the action used in [86] is anisotropic, but the $\mathcal{O}(\alpha_L^3)$ contributions to the Landau tadpole were found to be $u_0^{(6),L} \sim \mathcal{O}(1)$. This is an order of magnitude smaller than my estimate, but, since $\alpha_L^3 \simeq 0.001$, both results support the claim in [86] that the two-loop perturbative calculation of the Landau tadpole provides a very good estimate of the full nonperturbative Landau tadpole.

4.3   Plaquette tadpoles

The plaquette tadpole, u_0^P, is defined to be the fourth root of the expectation value of the plaquette:

$$u_0^P = \left\langle \frac{1}{N}\mathrm{Tr}P_{\mu\nu} \right\rangle^{1/4}, \qquad (4.9)$$

where the plaquette $P_{\mu\nu}$ is the one-by-one gauge invariant loop defined in Equation (2.8).

My calculation of the plaquette tadpole closely parallelled the method I used for the Landau tadpole factor. At one-loop there is again a single contributing diagram, which I give in Figure 4.1. I calculated the corresponding Feynman integral using the HPSRC routines and evaluated the integral numer-

ically using VEGAS. I show the two fermionic contributions to the two-loop factor in Figure 4.2.

4.3.1   Plaquette tadpole results

I present my results for the one- and two-loop plaquette tadpole parameters in Table 4.2 for both Wilson and Symanzik-improved gluons. I extrapolate the results to zero light quark mass. I obtained results with 10^5 function evaluations and 10 VEGAS iterations on six processors, which took about 40 seconds for the one-loop contributions. For the two-loop contributions I used 10^6 function evaluations and 15 VEGAS iterations on 128 processors, taking approximately 40 minutes. I verified that both one- and two-loop results were gauge-independent for three different choices of gauge parameter. I plot my data and the quadratic fit for the light quark mass extrapolation, shown by the blue line, in Figure 4.4.
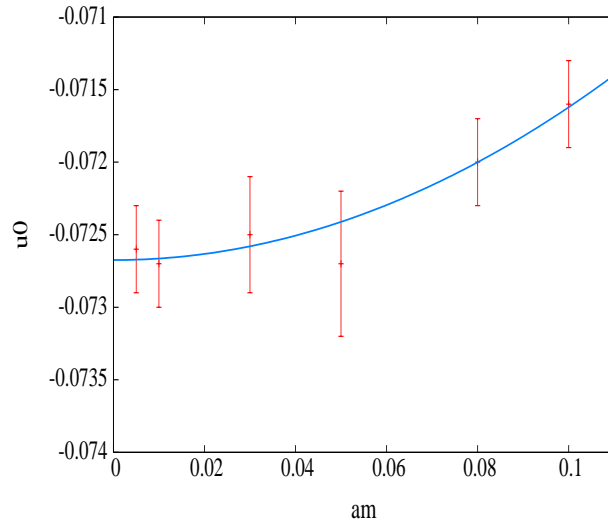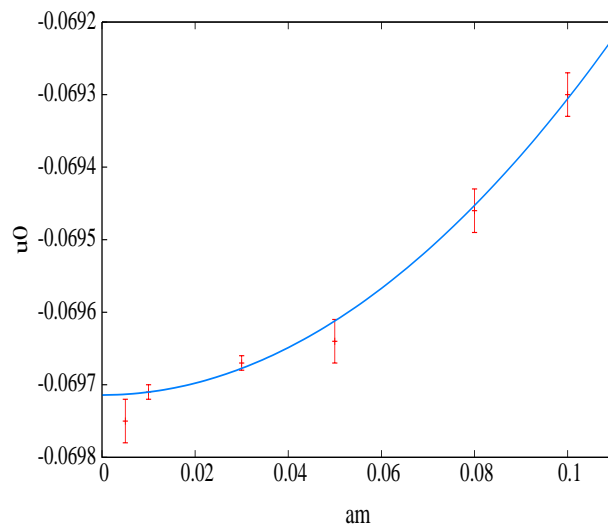

Figure 4.4: The light quark mass-dependence of the two-loop plaquette tadpole. I plot my fit to a function quadratic in the light quark mass in blue. I use Symanzik-improved gluons with ASQTad light quarks. Note the small scale on the y-axis. The smaller errors for the results at $am_q = 0.01$ and $am_q = 0.03$ are due to better statistics.

In Table 4.3 I present results for the quenched plaquette tadpole from

Action	$u_0^{(2),P}$	am_q	$u_0^{(4),P}$	
			Unimproved	ASQTad
		0.005	-0.06451(4)	-0.13583(5)
		0.01	-0.06450(4)	-0.13576(1)
		0.03	-0.06443(4)	-0.13570(1)
Wilson	1.04717(2)	0.05	-0.06427(4)	-0.13563(4)
		0.08	-0.06389(4)	-0.13532(4)
		0.10	-0.06355(4)	-0.13502(4)
		0.0	-0.0645121(21)	-0.135769(69)
		0.005	-0.03674(2)	-0.06976(3)
		0.01	-0.03674(2)	-0.06971(1)
		0.03	-0.03667(2)	-0.06967(1)
Symanzik	0.76708(2)	0.05	-0.03659(3)	-0.06964(3)
		0.08	-0.03637(3)	-0.06946(3)
		0.10	-0.03617(3)	-0.06930(3)
		0.0	-0.0367294(55)	-0.0697147(72)

Table 4.2: Plaquette tadpole corrections at one- and two-loops for Wilson and Symanzik-improved gluons. The two-loop results are the fermionic contributions only, with unimproved staggered light quark results presented in column four and ASQTad quarks in column five. The two-loop result at zero light quark mass result is an extrapolation; one-loop results are fermion mass independent. The uncertainties quoted are statistical errors from numerical integration, except in the massless light quark two-loop result. In this case, the uncertainty is from the fit to the light quark mass. The smaller errors for the ASQTad results at $am_q = 0.01$ and $am_q = 0.03$ are due to better statistics.

Lee's high-β simulations [11]. I extract the two-loop correction by fitting these results to a polynomial in α_L, including terms up to α_L^4, with the one-loop coefficient constrained to the value obtained using perturbation theory. I plot the quenched results in Figure 4.5 and the fit to a function quadratic in the light quark mass. Including higher order terms in the fit did not improve the extrapolation to zero light quark mass. For the two-loop coefficient I

obtain

$$u_0^{(4),P}|_{n_f=0} = 2.12(6). \tag{4.10}$$

The two-loop coefficient is, coincidentally, in agreement with the Landau tadpole coefficient. Whilst we would expect the one-loop terms to be close, because both methods attempt to smooth the gauge field, there is no particular reason to expect the two-loop values to be similar.

I incorporate these results with my fermionic two-loop values to present the first perturbative calculation of the unquenched plaquette tadpole at two-loops. For Symanzik-improved gluons with ASQTad sea quarks with mass $am_q = 0.01$, I find

$$u_0^P = 1 - 0.76708(2)\alpha_L - (2.12(6) - 0.06971(1)n_f)\, \alpha_L^2. \tag{4.11}$$

β	α_L	$u_0^P\|_{n_f=0}$	β	α_L	$u_0^P\|_{n_f=0}$
9	0.08841941	0.90818796	32	0.02486796	0.97970155
10	0.07957757	0.92121955	38	0.02094144	0.98306826
11	0.07234316	0.93072830	46	0.01729945	0.98615808
12	0.06631456	0.93807324	54	0.01473657	0.98827436
15	0.05305165	0.95283073	62	0.01283508	0.98984548
16	0.04973592	0.95627124	70	0.01136821	0.99103890
20	0.03978874	0.96610563	80	0.00994718	0.99217890
24	0.03315728	0.97230232	92	0.00864973	0.99322698
27	0.02947314	0.97561108	120	0.00663146	0.99482774

Table 4.3: Plaquette tadpole contributions extracted from quenched high-β simulations by Lee [11]. The bare coupling constant is given by $\alpha_L = 5/(2\beta)$.

4.3.2 Three-loop estimate

I estimate the three-loop contribution to the plaquette tadpole by subtracting the full two-loop perturbative results in Equation (4.11) from the nonperturbative plaquette tadpoles measured on the MILC collaboration's ASQTad ensembles. Results for ensembles with (2+1) flavours of sea quark are presented
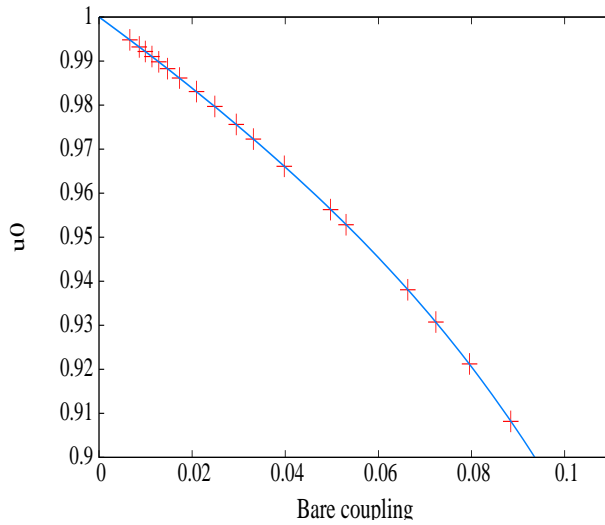
Figure 4.5: Plot of the fit to a function quadratic in the light quark mass for the quenched plaquette tadpole parameter.

in [22]. For the "coarse" ensemble, the plaquette tadpole was measured to be $u_0^P = 0.8677(1)$. This ensemble has light quark bare masses $am_{u,d} = 0.010$, strange quark mass $am_s = 0.050$ and bare coupling $\beta = 6.760$.

I use the relation between the bare lattice coupling and the plaquette tadpole

$$\alpha_L = -1.303615 \log u_0^P, \tag{4.12}$$

to compute a value of the coupling constant from the measured values of u_0^P listed in Table 1 of [22]. This relation arises from the one-loop definition of the coupling constant in terms of the one-by-one Wilson loop, i.e. the plaquette. I obtain $\alpha_L = 0.1850$. Using this value for the strong coupling constant, I obtain

$$u^{(6),P} \alpha_L^3 \simeq u_0^P - \left(1 - u_0^{(2),P} \alpha_L - u_0^{(4),P} \alpha_L^2 \right) = 0.080(1). \tag{4.13}$$

Thus my estimate of the three-loop perturbative contribution to the plaquette tadpole for Symanzik-improved gluons and ASQTad light quarks is

$$u^{(6),P} \simeq 12.6(2). \tag{4.14}$$

66

For the fermionic contribution, I use my value of $u_0^{(4),P}$ at light quark mass $am_q = 0.01$. I estimate the error from the dominant quenched contribution at two-loops, multiplied by α_L^2. This result is the same order of magnitude as my estimate of the three-loop Landau tadpole, Equation (4.8).

Equations (4.5) and (4.11) are the first determination of the unquenched Landau and plaquette tadpoles at two-loops for Symanzik-improved gluons with ASQTad light quarks. These new results allow me to estimate the three-loop contributions to both tadpoles. State-of-the-art lattice simulations by HPQCD now use HISQ light quarks, for which the two-loop tadpoles must be calculated. Although the tadpole calculation is complicated by the reunitarisation of the fattened links in the HISQ action, my code can be relatively easily extended to include HISQ sea quarks. This extension is currently underway.

In the next section, I report on my second perturbative improvement calculation, for the higher order kinetic terms in simple NRQCD.

4.4 NRQCD kinetic operator improvement

The higher order kinetic terms in the NRQCD action correct errors arising from the nonrelativistic expansion of the heavy quark fields. At tree-level, the coefficients of the kinetic terms are equal to unity. Quantum fluctuations renormalise the coefficients and these radiative corrections must be calculated to achieve high precision in lattice NRQCD simulations.

Nonperturbative lattice studies of heavy-heavy mesons using NRQCD have found large energy splittings between states with spatial momenta of equal magnitude but different individual components, for example, states with momenta $\mathbf{p} = (0, 0, 3)$ and $\mathbf{p} = (2, 2, 1)$ [47]. One contribution to these energy splittings is the renormalisation of cubic symmetry breaking terms in the NRQCD action, which first occur at $\mathcal{O}(a^4 p^4)$. Based on the work of [71], [87] and [88], Müller computed the renormalisation parameters of the $\mathcal{O}(a^4 p^4)$ kinetic energy terms for the full NRQCD action in Equation (2.66) using automated lattice perturbation theory [47]. My calculation of the corresponding renormalisation parameters for a simple NRQCD action

served as a cross-check of Müller's numerical code.

In the course of my calculation I discovered that the radiative corrections are infrared divergent unless the action is improved to include higher order kinetic corrections. Whilst the justification for this result is clear in retrospect, we did not anticipate the divergent behaviour initially. Before presenting my results, I derive expressions for the radiative corrections to the kinetic operators of a simple NRQCD discretisation. My derivation largely follows that given in [47] and [87], tailored to my choice of NRQCD action.

4.4.1 Simple NRQCD

I use the simple discretisation of NRQCD given in [49], the "Davies and Thacker" action,

$$S_{\mathrm{DT}} = a^3 \sum_x \psi^\dagger(\mathbf{x}, t) \left(\Delta_4^{(+)} - \sum_{j=1}^3 \frac{\Delta_j^{(+)} \Delta_j^{(-)}}{2aM} \right) \psi(\mathbf{x}, t). \qquad (4.15)$$

In momentum space the tree-level quark propagator for this action is

$$G_0^{-1}(w, \mathbf{p}) = e^{-aw} - 1 + \frac{4}{2aM} \sum_j \sin^2 \left(\frac{ap_j}{2} \right), \qquad (4.16)$$

where $w = -ip_4$ is the energy in Minkowski space. I derive the Feynman rules associated with this action in Appendix B. I expand $G_0^{-1}(w, \mathbf{p})$ for small momenta as

$$G_0^{-1}(w, \mathbf{p}) \approx -aw + \frac{4}{2aM} \sum_j \left(\left(\frac{ap_j}{2} \right)^2 - \frac{1}{3} \left(\frac{ap_j}{2} \right)^4 \right) + \dots \qquad (4.17)$$

The position of the tree-level quark pole, $aw_T(\mathbf{p})$, is the zero of $G_0^{-1}(w, \mathbf{p})$. In this case the pole is given by

$$aw_T(\mathbf{p}) = \frac{a^2 \mathbf{p}^2}{2aM} - \frac{a^4 p^4}{24aM} + \mathcal{O}(a^6 p^6). \qquad (4.18)$$

The one-loop propagator is related to the tree-level propagator via the

selfenergy $\Sigma(w, \mathbf{p})$:

$$G_1^{-1}(w, \mathbf{p}) = G_0^{-1}(w, \mathbf{p}) - \alpha_s \Sigma(w, \mathbf{p}), \qquad (4.19)$$

and so the dispersion relation at one-loop is

$$w(\mathbf{p}) = w_T(\mathbf{p}) - \alpha_s \Sigma(w_T(\mathbf{p}), \mathbf{p}). \qquad (4.20)$$

The NRQCD quark selfenergy is invariant under interchange of any two spatial momentum components $ap_i \leftrightarrow ap_j$, under spatial momentum reflections $ap_j \rightarrow -ap_j$ and transforms into its complex conjugate under $ap_4 \rightarrow -ap_4^\star$ [87]. Hence the small-momentum expansion of the selfenergy is

$$a\Sigma(w, \mathbf{p}) = \Sigma_0(w) + \Sigma_1(w)\frac{a^2\mathbf{p}^2}{2aM} + \Sigma_2(w)\frac{a^4(\mathbf{p}^2)^2}{8a^2M^2} + \Sigma_3(w)a^4p^4 + \ldots \quad (4.21)$$

We can compute the expansion coefficients, $\Sigma_i(w)$, which are functions of the energy, w, by taking appropriate combinations of partial derivatives of the selfenergy:

$$\Sigma_0(w) = a\Sigma(\mathbf{p} = 0), \qquad (4.22)$$

$$\Sigma_1(w) = aM \left.\frac{\partial^2(a\Sigma)}{\partial(ap_z)^2}\right|_{\mathbf{p}=0}, \qquad (4.23)$$

$$\Sigma_2(w) = a^2M^2 \left.\frac{\partial^4(a\Sigma)}{\partial(ap_y)^2\partial(ap_z)^2}\right|_{\mathbf{p}=0}, \qquad (4.24)$$

$$\Sigma_3(w) = \frac{1}{24}\left(\frac{\partial^4(a\Sigma)}{\partial(ap_z)^4} - 3\frac{\partial^4(a\Sigma)}{\partial(ap_y)^2\partial(ap_z)^2}\right)_{\mathbf{p}=0}. \qquad (4.25)$$

I expand the $\Sigma_i(w)$ functions as a Taylor series in w,

$$\Sigma_i = \sum_{j=0}^{\infty} \Sigma_i^{(j)} w^j, \qquad (4.26)$$

and combine this expansion with the expression for the selfenergy in Equation (4.21) and for the dispersion relations in Equations (4.18) and (4.20) to obtain

69

the one-loop dispersion relation:

$$aw(\mathbf{p}) = \frac{a^2\mathbf{p}^2}{2aM}\left(1 - \alpha_s\left(\Sigma_0^{(1)} + \Sigma_1^{(0)}\right)\right) - \frac{a^4p^4}{24aM}\left(1 - \alpha_s\Sigma_0^{(1)}\right)$$
$$- \alpha_s\left(\Sigma_0^{(0)} + \left(2\Sigma_0^{(2)} + 2\Sigma_1^{(1)} + \Sigma_2^{(0)}\right)\frac{a^4(\mathbf{p}^2)^2}{8a^2M^2}\Sigma_3^{(0)}a^4p^4\right). \quad (4.27)$$

I extract the renormalisation parameters by requiring that the one-loop dispersion relation has the renormalised form

$$aw(\mathbf{p}) = \frac{a^2\mathbf{p}^2}{2aM_r} - \frac{a^4p^4}{24aM_r} - \alpha_s\left(E_0 + a\delta w(\mathbf{p})\right). \quad (4.28)$$

We can immediately read off the mass renormalisation from the coefficient of the $\mathcal{O}(a^2\mathbf{p}^2)$ term by comparing Equations (4.27) and (4.28). Thus the mass renormalisation is given by

$$Z_M^{-1} = 1 - \alpha_s\left(\Sigma_0^{(1)} + \Sigma_1^{(0)}\right). \quad (4.29)$$

We obtain the heavy quark energy shift from the one-loop coefficient:

$$E_0 = \Sigma_0^{(0)}. \quad (4.30)$$

I discuss the mass renormalisations in more detail in Chapter 5, where I also derive an expression for the NRQCD wavefunction renormalisation. For now we need only the energy shift and the kinetic correction coefficients. The kinetic corrections are:

$$a\delta w(\mathbf{p}) = W_1\frac{a^4(\mathbf{p}^2)^2}{8a^2M^2} + W_2a^4p^4, \quad (4.31)$$

$$W_1 = 2\left(\Sigma_0^{(2)} + \Sigma_1^{(1)}\right) + \Sigma_2^{(0)}, \quad (4.32)$$

$$W_2 = \Sigma_3^{(0)} - \frac{\Sigma_1^{(0)}}{24aM}. \quad (4.33)$$

For consistency with, and comparison to, the literature (see, for example, [47], [71] and [89]), I also introduce the Ω_i parameterisation functions, which

are related to the $\Sigma_i^{(j)}(w)$ functions by

$$\Omega_0 = \operatorname{Re}\Sigma_0^{(0)} = \Sigma(0), \tag{4.34}$$

$$\Omega_1 = -\operatorname{Re}\Sigma_0^{(1)} = \operatorname{Im}\left.\frac{\partial\Sigma}{\partial p_4}\right|_{p=0}, \tag{4.35}$$

$$\Omega_2 = \operatorname{Re}\Sigma_1^{(0)} = aM\operatorname{Re}\left.\frac{\partial^2\Sigma}{\partial p_z^2}\right|_{p=0}. \tag{4.36}$$

I use the relative simplicity of the Davies and Thacker action to compute the correction coefficients W_i using a mix of analytic and numerical methods. I now outline these calculations.

4.4.2 Calculating the kinetic correction coefficients

In continuum QCD only one Feynman diagram contributes to the selfenergy at one-loop, whereas in lattice NRQCD there are contributions from four diagrams. On top of the lattice artifact tadpole diagrams, the non-relativistic formulation distinguishes space and time and this distinction introduces two different Feynman rules, one for temporal gluons and one for spatial gluons. The Feynman rules associated with the Davies and Thacker action, Equation (4.15), are given in [49] and I have checked these Feynman rules by hand. I have also computed the Feynman rules for an alternative discretisation of simple NRQCD. My derivation of both sets of Feynman rules are presented in Appendix B. I show the four diagrams that must be evaluated in Figure 4.6. Each diagram represents a four-dimensional Euclidean integral that, in principle, can be evaluated numerically. However, the integrands are strongly peaked around poles in the complex k_0 plane. Numerical Monte Carlo integration methods, such as VEGAS, generally do not cope well with strongly peaked integrands. To speed up the calculation, I evaluated the k_0-integral analytically and then computed the less strongly peaked three-dimensional $\mathbf{k}$-integral using VEGAS.

I illustrate the basic steps of the calculation using the example of the temporal gluon "rainbow" diagram, illustrated in the top left corner of Figure
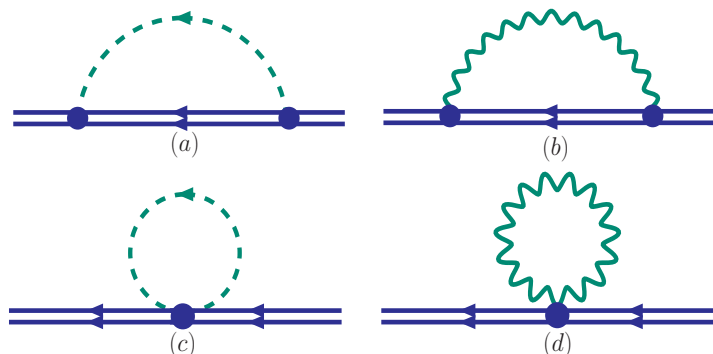
Figure 4.6: The four selfenergy diagrams contributing to the renormalisation of the NRQCD kinetic operators. Double blue lines are heavy quarks, wiggly green lines indicate spatial gluons and green dotted lines are temporal gluons. The commonly used names, "rainbow" for the upper pair of diagrams and "tadpole" for the lower, arise from the shape of the gluon propagators.

4.6, diagram (a). The full expression for this rainbow diagram with arbitrary external quark spatial momenta $\mathbf{p}$ (all vertex momenta defined as incoming) is

$$\Sigma^{\text{rbow}} = a^3 g^2 C_2 \int \frac{\mathrm{d}^4(ak)}{a^3(2\pi)^4} \frac{1}{\widehat{k}^2 + a^2\lambda^2} G_0(we^{-iap_0}, \mathbf{k} - \mathbf{p}), \qquad (4.37)$$

where $C_2 = 4/3$ is the colour factor and I have introduced the conventional lattice shorthand

$$\widehat{k}_\mu = 2\sin\left(\frac{ak_\mu}{2}\right). \qquad (4.38)$$

The heavy quark propagator for the Davies and Thacker action, G_0, is given in Equation (4.16).

I transform the k_0 integral with the standard change of coordinates $ak_0 \rightarrow z = e^{iak_0}$, so that the integral becomes

$$\Sigma^{\text{rbow}} = -g^2 C_2 \frac{i}{2\pi} \int \frac{\mathrm{d}^3(ak)}{(2\pi)^3} \oint \frac{\mathrm{d}z}{z} \frac{1}{(z - z_-)(z - z_+)(z - z_Q)}, \qquad (4.39)$$

and the contour of integration is now the unit circle. The gluon poles lie at

$$z_\pm = \frac{\kappa \pm \sqrt{\kappa^2 - 4}}{2}. \qquad (4.40)$$

where

$$\kappa = \hat{k}^2 + a^2\lambda^2 + 2, \qquad (4.41)$$

and the heavy quark pole occurs at

$$z_Q = 1 - \frac{1}{2aM} \sum_{j=1}^{3} \widehat{(k-p)}_j^{\,2}. \qquad (4.42)$$

I evaluate this integral by closing the contour at infinity: the condition that $zf(z) \to 0$ as $z \to \infty$ ensures that the contour at infinity gives no contribution. In this case we have

$$[(z-z_-)(z-z_+)(z-z_Q)]^{-1} = z^{-3}[(1-z_-z^{-1})(1-z_+z^{-1})(1-z_Qz^{-1})]^{-1}, \ (4.43)$$

which indeed tends to zero in the $z \to \infty$ limit. I close the contour to the right to isolate the pole at $z = z_+$. The result is just

$$\Sigma^{\mathrm{rbow}} = -g^2 C_2 \int \frac{\mathrm{d}^3(ak)}{(2\pi)^3} \frac{1}{(z_+ - z_-)(z_+ - z_Q)}. \qquad (4.44)$$

I extracted the temporal rainbow contribution to W_1 and W_2 by differentiating this expression according to Equations (4.32) or (4.33) respectively. I evaluated the result at $\mathbf{p} = 0$ and computed the remaining three-dimensional integral numerically with VEGAS. I present all results in Section 4.4.3. In particular I demonstrate that the $\mathcal{O}(a^4p^4)$ renormalisation parameters for an NRQCD action correct only to $\mathcal{O}(a^2p^2)$ are infrared divergent.

4.4.3   Numerical results

In Table 4.4 I show results for the energy shift and the renormalisation parameters for the higher order kinetic corrections in simple NRQCD. I give results for the Davies and Thacker action, in Equation (4.15), and a minimally-improved action given by

$$\widetilde{S}_{\mathrm{DT}} = a^3 \sum_{x} \psi^\dagger(\mathbf{x},t) \left(\Delta_4^{(+)} - \frac{\widetilde{\Delta}^{(2)}}{2aM} \right) \psi(\mathbf{x},t). \qquad (4.45)$$

This action is the Davies and Thacker action with the unimproved Laplacian replaced by the improved Laplacian,

$$\widetilde{\Delta}^{(2)} = \Delta^{(2)} - \frac{a^2}{12} \sum_j \left[\Delta_j^{(+)} \Delta_j^{(-)} \right]^2 . \qquad (4.46)$$

I outline the derivation of the renormalisation parameters for the improved action in Appendix D. I used a gluon mass of $a^2\lambda^2 = 10^{-6}$ and fixed the gauge to Feynman gauge. Extrapolation to zero gluon mass is not required [47]. In Table 4.4 I present my results for the heavy quark energy shift, E_0, and the correction coefficients W_1 and W_2 for five different heavy quark masses between $aM_Q = 4.00$ and $aM_Q = 5.40$. I do not present results for masses smaller than $aM = 4.0$ as this would require introducing the stability parameter that I discuss in Section 2.4.1.

For W_2 I give only the finite contribution for the Davies and Thacker action. For the improved action, W_2 is infrared finite. I obtained all results with 10^4 function evaluations and 20 VEGAS iterations, which took approximately 10 minutes on a single processor for E_0 and 40 minutes for W_1 and W_2.

NRQCD action	aM_Q	E_0	W_1	W_2
	5.40	-2.277(2)	0.0546(1)	-0.00122(1)
S_{DT}	5.00	-2.332(2)	0.0551(1)	-0.00118(1)
	4.70	-2.381(2)	0.0555(1)	-0.00116(1)
	4.00	-2.498(2)	0.0562(1)	-0.00110(1)
	5.40	-2.145(2)	0.0398(1)	0.00153(1)
$\widetilde{S}_{\mathrm{DT}}$	5.00	-2.190(2)	0.0391(1)	0.00161(1)
	4.70	-2.230(2)	0.0385(1)	0.00167(1)
	4.00	-2.320(2)	0.0372(1)	0.00182(1)

Table 4.4: Higher-order kinetic improvement factors for two different simple NRQCD actions. I give results for the finite part of the Davies and Thacker action in the second column and the full results for the improved NRQCD action of Equation (4.45) in the third column. Errors for the uncertainties associated with the finite part of W_2 for the Davies and Thacker action are from the fit to the gluon mass.

I extracted the infrared divergent contribution to W_2 using four different heavy quark masses between $aM = 4.00$ and $aM = 5.40$. I obtained

$$W_2^{\text{div}} = 0.00875(10) \frac{1}{aM} \log(a^2\lambda^2), \tag{4.47}$$

in good agreement with expected analytic result

$$\frac{1}{36\pi aM} \log(a^2\lambda^2) \simeq 0.008842 \frac{1}{aM} \log(a^2\lambda^2). \tag{4.48}$$

I explain the origin of this infrared divergence in the next section.

4.4.4 Infrared divergences

The infrared divergent behaviour exhibited in the results of Section 4.4.3 is not unexpected: the renormalisation parameter for the $\mathcal{O}(a^4p^4)$ term in the selfenergy gains a infrared divergent contribution from the wavefunction renormalisation, which is removed by including $\mathcal{O}(a^4p^4)$ improvement in the action. We can understand the occurrence of this divergence in general terms by examining the form of the selfenergy. At tree-level we can express the selfenergy, at small external momenta, as

$$\Sigma_T \sim iap_0 + \frac{a^2p^2}{2aM} + \frac{a^4p^4}{2aM} + \mathcal{O}(a^6p^6). \tag{4.49}$$

The $\mathcal{O}(a^4p^4)$ term arises from the Taylor expansion of the kinetic term $\sin(ap)$. The quark self-interaction induces $\mathcal{O}(a^4p^4)$ contributions to the selfenergy at one-loop and each term is multiplicatively renormalised. Therefore we can write the one-loop selfenergy as

$$\begin{aligned}
\Sigma^{(1)} &\sim Z_\psi \left[ip_0 + Z_M \left(\frac{a^2p^2}{2aM} + \frac{a^4p^4}{2aM} \right) + Z_{\mathbf{p}^4} a^4p^4 \right] + \mathcal{O}(a^6p^6) \\
&= (1 + \alpha_s \delta Z_\psi) \left[ip_0 + (1 + \alpha_s \delta Z_M) \left(\frac{a^2p^2}{2aM} + \frac{a^4p^4}{2aM} \right) + \alpha_s \delta Z_{\mathbf{p}^4} a^4p^4 \right].
\end{aligned} \tag{4.50}$$

We can read off the $\mathcal{O}(a^4 p^4)$ renormalisation coefficient from this expression for $\Sigma^{(1)}$. The one-loop contribution is

$$\alpha_s \left(\delta Z_\psi + \delta Z_{\mathbf{p}^4} \right). \tag{4.51}$$

The wavefunction renormalisation is infrared divergent in Feynman gauge, so this expression is manifestly infrared divergent. In fact, we can obtain the infrared divergence analytically. The long wavelength behaviour of NRQCD must match that of continuum QCD by construction, so the infrared divergence in the wavefunction renormalisation is just that of the continuum wavefunction renormalisation for massive quarks, which I discuss in more detail in Chapter 6. The logarithmic infrared divergence is given by

$$Z_Q^{IR} = -\frac{2\alpha_s}{3\pi} \log \left(\frac{\lambda^2}{M^2} \right). \tag{4.52}$$

To obtain the analytic result for W_2^{div} in Equation (4.48), we must also include the factor of $1/24aM$ from the derivative definition of W_2 in Equation (4.33).

My results for the infrared divergence in Equation (4.47), obtained using the mixed analytic and numerical approach described in this chapter, are in full agreement with my results presented for the NRQCD wavefunction renormalisation in the next chapter. These results were obtained using a fully automated process and their agreement with both each other and the analytic result provides confidence in both methods.

We now consider the selfenergy in the case of the simple action, but with an improved derivative. Here the tree-level selfenergy takes the form

$$\widetilde{\Sigma}_T \sim iap_0 + \frac{a^2 p^2}{2aM} + \mathcal{O}(a^6 p^6). \tag{4.53}$$

Notice that the inclusion of an improved derivative removes the $\mathcal{O}(a^4 p^4)$ contributions from $\widetilde{\Sigma}_T$. Thus $\widetilde{\Sigma}^{(1)}$ is

$$\widetilde{\Sigma}^{(1)} \sim (1 + \alpha_s \delta Z_\psi) \left[ip_0 + (1 + \alpha_s \delta Z_M) \frac{a^2 p^2}{2aM} + \alpha_s \delta Z_{\mathbf{p}^4} a^4 p^4 \right] \tag{4.54}$$

and we can again easily identify the one-loop renormalisation of the $\mathcal{O}(a^4 p^4)$ contribution. In this case the renormalisation of the p^4-term is simply given by

$$\alpha_s \delta Z_{\mathbf{p}^4}. \tag{4.55}$$

We see this parameter is no longer infrared divergent or, at least, not manifestly so.

4.4.5   Comparison to the literature

In Table 4.5 I compare my results to those obtained by Müller using a fully automated procedure. I compare the individual diagram contributions to the energy shift, E_0. I used a heavy quark mass of $aM = 4.0$ and a gluon mass of $a^2 \lambda^2 = 10^{-4}$. All calculations were performed in Feynman gauge. All the results are in good agreement with each other. As a further cross-check, Müller reproduced the results for the correction coefficient in [87]. The mutual agreement between my results and those of [47] and between [47] and [87] support our confidence in the validity of both calculations.

	Rainbow		Tadpole	
	Temporal	Spatial	Temporal	Spatial
E_0	-3.1194(15)	0.2965(1)	1.2984(7)	-0.9735(3)
Ref. [47]	-3.1218(15)	0.2964(2)	1.2986(6)	-0.9740(4)

Table 4.5: A comparison of results for the heavy quark energy shift E_0 for the Davies and Thacker NRQCD action. I give my results in the first row and Müller's results in the second row [47]. All results obtained with $aM = 4.0$ and gluon mass $a^2 \lambda^2 = 10^{-4}$.

4.4.6   Observations

Simulations of heavy-heavy mesons using lattice NRQCD have found large energy splittings between mesons with equal spatial momentum, $\mathbf{p}$, but with different $\sum_{i=1}^{3} p_i^4$, for example states with $\mathbf{p} = (0, 0, 3)$ and $\mathbf{p} = (2, 2, 1)$

[47]. One contribution to these energy splittings is the radiative corrections to the leading cubic symmetry breaking term, which is $c_5 \Delta^{(4)}/(24aM)$. At tree-level $c_5^{(0)} = 1$. The coefficient $c_5^{(1)}$ cancels the radiative corrections at one-loop and is related to W_2 by $c_5^{(1)} = 24aMW_2$. The energy splittings can be removed by tuning c_5 nonperturbatively to a value of $c_5 = 2.6$. Unfortunately this large renormalised value is inconsistent with the relatively small values obtained using automated lattice perturbation theory in [47] and [90], which give a one-loop value of $c_5^{(1)} \simeq 0.4$ for a range of heavy quark masses between $aM = 2.0$ and $aM = 3.4$. My computation of the correction coefficients, and extraction of the correct - but unpredicted - infrared divergence, for the simple Davies and Thacker action confirms that the automated lattice perturbation theory was implemented correctly. Therefore we must conclude that the one-loop radiative corrections to c_5 are not the sole source of the mesonic energy splittings.

There are a number of other sources that could contribute to the discrepancy between the correction coefficient calculated using nonperturbative tuning and using automated lattice perturbation theory. The first possibility is a large two-loop correction to the perturbative result. A correct choice of scale should reduce second order contributions, but may come at the expense of large higher order contributions. Two-loop perturbative results would be required to confirm this hypothesis, but unfortunately the complexity of two-loop lattice perturbation theory is formidable.

A second possibility is that $\mathcal{O}(a^6 p^6)$ corrections strongly influence the correction coefficient c_5. Müller found that including the tree-level $\mathcal{O}(a^6 p^6)$ improvement term $\Delta^{(6)}/(180aM)$ did indeed significantly reduce the renormalisation of c_5, by a factor of 5–10. This is of particular concern in light of the fact that I found the $\mathcal{O}(a^4 p^4)$ renormalisation parameters were not only non-negligible but infrared divergent for an action that wasn't fully improved to $\mathcal{O}(a^4 p^4)$. Obtaining higher order kinetic corrections may prove necessary in the future and in Appendix D I briefly discuss extending this work to $\mathcal{O}(a^6 p^6)$ to investigate the feasibility of further radiative improvement. However, this may not prove necessary. In the nonperturbative simulation, the $\mathcal{O}(a^6 p^6)$ improvement term was included with the tree-level value of the co-

efficient. The fitting process, whereby the $\mathcal{O}(a^6 p^6)$ was fixed to its classical value and the coefficient of the $\mathcal{O}(a^4 p^4)$ term nonperturbatively tuned, may not be optimal and indeed could be another source of the difference between the perturbative and nonperturbative results for $c_5^{(1)}$.

One final source of error may be the relatively large lattice spacing of the lattice used in the nonperturbative simulations. NRQCD is not the only constituent of the lattice simulation and other contributions to the energy splittings might be reduced on finer lattices.

Further work is clearly needed to clarify this discrepancy. Nonperturbative simulations on finer lattices are being explored and these may shed light on the issue. Extending the perturbative renormalisation calculation to $\mathcal{O}(\alpha_s a^6 p^6)$ and $\mathcal{O}(\alpha_s^2 a^4 p^4)$ could also illuminate the problem more brightly. However, the computational complexity of this extension is impressive and not to be underestimated. Implementing the sixth-derivatives numerically is highly nontrivial and the two-loop perturbative lattice calculation would require the evaluation of around 30 diagrams. Whilst calculation is possible in principle, it is not yet feasible in practice.

In the final section of this chapter I review the calculation of the radiative correction to the chromo-magnetic operator in highly-improved NRQCD. This calculation was undertaken by Hammant [14], and represents the first outcome of our implementation of background field gauge in the HiPPy and HPsrc routines.

4.5 NRQCD chromo-magnetic operator improvement

The calculation of the radiative corrections to the chromo-magnetic operator in the highly-improved NRQCD action is an important component of the improvement programme for lattice NRQCD simulations. The chromo-magnetic contribution and four-fermion spin-spin interaction both contribute to the hyperfine structure of heavy quarkonium states in NRQCD.

Gray *et al.* determined the $\Upsilon - \eta_b$ hyperfine splitting using NRQCD valence quarks, with Symanzik-improved gluons and ASQTad sea quarks in [85]. This calculation did not include radiative corrections to the chromo-magnetic

operator in the NRQCD action and obtained results that were dependent on the lattice spacing and in disagreement with the world experimental average of 69.3(2.8) MeV [8].

Updated nonperturbative simulation results using a radiatively-corrected NRQCD action have not yet been completed, but early indications suggest that including the chromo-magnetic corrections and four-fermion contact terms in the NRQCD action remove all lattice spacing dependence in the $\Upsilon - \eta_b$ hyperfine splitting and bring the result into line with the experimental average [14].

As I discuss in Section 3.4.2 background field gauge greatly simplifies the matching calculation for the chromo-magnetic operator. In continuum QCD, the renormalised effective action includes the fermion terms

$$\Gamma_{\text{QCD}}[\Psi_R, \overline{\Psi}_R, A] = \overline{\Psi}_R \slashed{D} \Psi_R + b_\sigma \overline{\Psi}_R \frac{\sigma^{\mu\nu} F_{\mu\nu}}{2m_R} \Psi + \dots, \qquad (4.56)$$

where $\sigma^{\mu\nu}$ is the anticommutator $[\gamma^\mu, \gamma^\nu]/2$, $F_{\mu\nu}$ is the field strength tensor and m_R is the renormalised mass. The coefficient b_σ is given by

$$b_\sigma = \delta Z_\sigma Z_2 Z_M, \qquad (4.57)$$

where δZ_σ is the renormalisation of the second term on the right-hand side of Equation (4.56). We can expand b_σ as a power series in the strong coupling constant. The leading correction to this coefficient occurs at $\mathcal{O}(\alpha_S)$ and comes from δZ_σ.

To match this term to the relevant contribution in lattice NRQCD, we first perform an FWT transformation to obtain

$$(1 + b_\sigma) \psi_R^\dagger \frac{\sigma \cdot \mathbf{B}}{2m_R} \psi_R, \qquad (4.58)$$

where ψ_R is a two-component Pauli spinor. There are two diagrams that contribute to this term in continuum QCD (see [14]) and the result is

$$b_\sigma = \left(\frac{3}{2\pi} \log \frac{\mu}{m} + \frac{13}{6\pi} \right) \alpha_S, \qquad (4.59)$$

where μ is an infrared cutoff scale.

In lattice NRQCD, the quantum effective action contains the spin-dependent term

$$\Gamma_{\text{NRQCD}}[\psi_R, \overline{\psi}_R, A] = c_4 Z_\sigma^{\text{NRQCD}} Z_2^{\text{NRQCD}} Z_m^{\text{NRQCD}} \psi_R^\dagger \frac{\sigma \cdot \mathbf{B}}{2m_R} \psi_R. \qquad (4.60)$$

We require the anomalous chromo-magnetic moment to be equal in both QCD and NRQCD, which gives us, by comparing Equations (4.58) and (4.60), the matching condition

$$(1 + b_\sigma) = c_4 Z_\sigma^{\text{NRQCD}} Z_2^{\text{NRQCD}} Z_m^{\text{NRQCD}}. \qquad (4.61)$$

The tree-level and one-loop coefficients are therefore

$$c_4^{(0)} = 1, \qquad (4.62)$$

$$c_4^{(1)} = b_\sigma^{(1)} - \delta Z_\sigma^{\text{NRQCD},(1)} - \delta Z_2^{\text{NRQCD},(1)} - \delta Z_m^{\text{NRQCD},(1)}. \qquad (4.63)$$

There are four extra diagrams that contribute to the lattice NRQCD calculation. Both NRQCD and QCD contributions to $c_4^{(1)}$ are logarithmically divergent and the overall divergent contribution is

$$c_4^{(1),\text{div}} = -\frac{3\alpha}{2\pi} \log(aM). \qquad (4.64)$$

Including tadpole corrections, the final expression for the coefficient $c_4^{(1)}$ is

$$c_4^{(1)} = \frac{13}{6\pi} - \delta \widetilde{Z}_\sigma^{\text{NRQCD},(1)} - \delta \widetilde{Z}_2^{\text{NRQCD},(1)} - \delta \widetilde{Z}_m^{\text{NRQCD},(1)}$$
$$- \delta Z_M^{u_0,(1)} - \delta Z_\sigma^{u_0,(1)} + c_4^{(1),\text{div}}, \qquad (4.65)$$

where the tildes indicate that the infrared divergence has been subtracted off. I denote the tadpole correction factors with the superscript u_0. The tadpole correction factors are

$$\delta Z_M^{u_0,(1)} = -\left(\frac{2}{3} + \frac{3}{a^2 M^2}\right) u_0^{(2)} \qquad (4.66)$$

and

$$\delta Z_\sigma^{u_0,(1)} = \left(\frac{13}{3} + \frac{13}{4aM} - \frac{3}{8n(a^2M^2} - \frac{3}{4a^3M^3} \right) u_0^{(2)}. \qquad (4.67)$$

In [14] we use Landau tadpoles, with the value of $u_0^{(2)}$ given in Table 4.1 for Symanzik-improved gluons.

The results for each contribution to $c_4^{(1)}$ in Equation (4.65) are collected in Table 1 of [14], with data for three different heavy quark masses. We also provide an estimate of the effect of the radiative correction to the chromo-magnetic operator and four fermion interactions on the $\Upsilon - \eta_b$ hyperfine splitting. Although these estimates are no replacement for full nonperturbative simulations, the results are encouraging and indicate that using a fully-improved action will bring lattice NRQCD results for the hyperfine splitting into line with the current experimental world average.

Chapter 5

Perturbative renormalisation

The precise theoretical and experimental determination of quark masses is an important component of high-precision tests of the Standard Model. One current focus for tests of the Standard Model is the unitarity of the CKM matrix, which describes flavour-changing quark transitions. Quark masses serve as an input into the tests of CKM matrix unitarity; for example, the mass of the b quark is used in the extraction of the CKM matrix element $|V_{ub}|$ from inclusive semileptonic decays of B mesons [91].

Recent high-precision calculations of the b quark mass using realistic lattice QCD simulations [25] and perturbative QCD combined with experimental results [92] are in good agreement, obtaining values of $m_b(m_b,\ n_f = 5) = 4.165(23)$ GeV and $m_b(m_b) = 4.163(16)$ GeV respectively.

The lattice result was obtained using relativistic HISQ valence quarks with ASQTad sea quarks. However, most current lattice studies of b quarks use an effective field theory, such as NRQCD. Simulating both valence and sea quarks with relativistic actions allows a much greater precision, but is only now becoming possible with the advent of finer lattices and highly improved actions. Lattices are not yet fine enough to directly simulate at the physical b quark mass: even on the very finest lattices with HISQ heavy quarks an extrapolation to the heavy quark mass is required [25]. Precise results from effective theories for heavy quarks therefore still serve an important role in precision tests of the Standard Model.

In this chapter I discuss the derivation and calculation of the heavy quark renormalisation parameters in NRQCD. I calculate the wavefunction renormalisation, energy shift and mass renormalisation at one-loop for several different NRQCD actions. These results are a useful cross-check of my code. I then calculate the energy shift for highly-improved NRQCD at two-loops. I use the two-loop results to extract a precise prediction of the mass of the b quark from lattice NRQCD simulations. This result improves on a previ-

ous determination of $m_b(m_b) = 4.4(3)$ GeV from unquenched lattice QCD simulations using NRQCD valence b quarks [85]. The dominant error in that calculation arose from the use of one-loop perturbation theory in the matching between lattice quantities and the continuum result. I calculate the fermionic contribution to the two-loop energy shift and mass renormalisation and discuss the quenched contributions calculated by Lee using weak coupling (high-β) simulations [11]. This mixed strategy, incorporating high-β quenched simulations and automated lattice perturbation theory, is the first ever two-loop calculation in NRQCD.

5.1 NRQCD renormalisation parameters

I first derive an expression for the NRQCD wavefunction renormalisation. I derive the mass renormalisation and energy shift in Section 4.4.1 and so do not repeat the analysis here. An equivalent derivation of the wavefunction renormalisation for mNRQCD is given in [47] and [88]. In this section I set the lattice spacing to unity, that is $a = 1$.

5.1.1 Wavefunction renormalisation

I calculate the wavefunction renormalisation by comparing the tree-level and one-loop quark propagators. At tree-level the heavy quark propagator is given by Equation 4.16, which I write, for small momenta, as

$$G_0^{-1}(w, \mathbf{p}) = w_T - w, \tag{5.1}$$

where $w = -ip_4$ is the energy in Minkowski space. The tree-level onshell value of w is w_T. Following the derivation outlined in Chapter 4, I include one-loop quantum corrections to the tree-level propagator via the heavy quark selfenergy, $\alpha_s \Sigma(w, \mathbf{p})$. I show the one-loop contributions in Figure 4.6.

I write the one-loop propagator as

$$G_1^{-1}(w, \mathbf{p}) = G_0^{-1}(w, \mathbf{p}) - \alpha_s \Sigma(w, \mathbf{p}), \tag{5.2}$$

and define the wavefunction renormalisation, Z_ψ, such that the renormalised quark propagator has the same form as the tree-level propagator, multiplied by the wavefunction renormalisation. The new onshell value of w is w_1, the root of $G(w, \mathbf{p}) = 0$. Thus $G(w, \mathbf{p})$ at one-loop is

$$G_1^{-1}(w, \mathbf{p}) = Z_\psi^{-1}(w_1 - w), \tag{5.3}$$

where the onshell value w_1 is obtained by setting $G(w_1, \mathbf{p}) = 0$.

I expand the selfenergy around the new onshell value w_1,

$$\Sigma(w, \mathbf{p}) = \Sigma(w_1, \mathbf{p}) + (w_1 - w) \frac{\partial \Sigma}{\partial w} \bigg|_{w=w_1} + \cdots, \tag{5.4}$$

and substitute this expression into $G(w, \mathbf{p})$ to give

$$G_1^{-1}(w, \mathbf{p}) = (w_1 - w) \left(1 - \alpha_s \left[\Sigma(w_1, \mathbf{p}) + \frac{\partial \Sigma}{\partial w} \bigg|_{w=w_1} \right] \right) + \cdots. \tag{5.5}$$

We compare Equations (5.3) and (5.5) to read-off the wavefunction renormalisation and use the relation $\Sigma(w_1, \mathbf{p}) = \Sigma(w_T) + \mathcal{O}(\alpha_s)$ to obtain

$$Z_\psi = 1 + \alpha_s \left[\Sigma(w_T, \mathbf{p}) + \frac{\partial \Sigma}{\partial w} \bigg|_{w=w_T} \right] = 1 + \alpha_s \left(\Omega_0 + \Omega_1 \right). \tag{5.6}$$

The wavefunction renormalisation is infrared divergent in Feynman gauge, so I extract the gluon mass dependence of the wavefunction renormalisation using an infrared subtraction function, Z_ψ^{sub}:

$$Z_\psi^{\mathrm{sub}} = \frac{4}{3} \int \frac{\mathrm{d}^4 k}{(2\pi)^4} \frac{M^2}{(\widehat{k}^2 + iMk_0)^2(\widehat{k}^2 + \lambda^2)}. \tag{5.7}$$

Here M is the heavy quark mass and λ^2 the infrared cutoff scale.

I fit Z_ψ^{sub} to a logarithmic function of the gluon mass squared to obtain

$$Z_\psi^{\mathrm{sub}} = -0.05259(10) + 0.10614(19) \log \lambda^2, \tag{5.8}$$

using VEGAS with 5×10^7 function evaluations and 20 iterations for 12 different
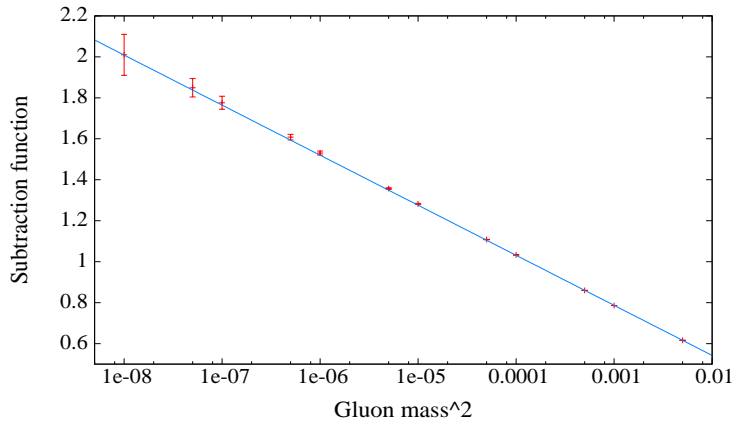
Figure 5.1: Logarithmic fit of the gluon mass dependence for the wavefunction renormalisation subtraction function. I plot the fit in blue and the data from VEGAS as red crosses.

values of the gluon mass between $\lambda^2 = 10^{-3}$ and $\lambda^2 = 10^{-8}$. I plot the results in Figure 5.1, with the fit shown by the blue line. We expect the long-distance behaviour of the NRQCD wavefunction renormalisation to match that of the massive wavefunction renormalisation in continuum QCD. The logarithmic divergence of the subtraction function is in good agreement with the expected behaviour, which is given by

$$Z_\psi^{\mathrm{IR}} = -\frac{2}{3\pi} \log \lambda^2 \simeq -0.212207 \log \lambda. \tag{5.9}$$

5.1.2 Zero point energy shift and mass renormalisation

I derive expressions for the heavy quark energy shift and the mass renormalisation in Section 4.4.1, by examining the dispersion relation for the heavy quark. I do not repeat the analysis here, but rather collect the resulting expressions for convenience. The mass renormalisation is

$$Z_M^{-1} = 1 - \alpha_s \left(\Sigma_0^{(1)} + \Sigma_1^{(0)} \right) = 1 - \alpha_s \left(\Omega_2 - \Omega_1 \right), \tag{5.10}$$

and the heavy quark energy shift is

$$E_0 = \alpha_s \Sigma_0^{(0)} = \alpha_s \Omega_0. \tag{5.11}$$

I compute the heavy quark energy shift, wavefunction renormalisation and mass renormalisation using a fully automated procedure. I wrote new `HPSRC` routines to evaluate the one-loop heavy quark selfenergy. The routines specify the external quark momentum and action type and select which diagrams and parameters to evaluate using a `namelist`, which is read at runtime. I implemented the `TaylUR` derived-type for the vertices and propagators in order to extract the necessary derivatives of the diagrams. I generated all the necessary vertex function files using `HiPPy`, which I discuss in greater detail in Section 3.3.1.

5.1.3   One-loop results

I present numerical results for the one-loop energy shift and mass renormalisation for the "onlyH0" action in Table 5.1. This action corresponds to the NRQCD action of Equation (2.66) without improvement, that is, with $\delta H = 0$. I derive the Feynman rules for this action in Appendix B. I use unimproved Wilson gluons and evaluate the results with 10^6 `VEGAS` iterations and 10 function evaluations, which took approximately 55 minutes on 12 processors.

aM_Q	E_0	Z_M
5.00	-2.6233(35)	0.6439(16)
4.70	-2.6619(39)	0.6484(18)
4.00	-2.7535(39)	0.6594(18)
2.80	-3.0316(37)	0.8996(19)
2.50	-3.1414(38)	0.9291(19)
2.35	-3.2112(39)	0.9433(19)
1.95	-3.4376(46)	0.9933(20)
1.88	-3.4867(41)	1.0010(20)
1.80	-3.5444(39)	1.0146(20)
1.50	-3.8305(41)	1.0619(20)

Table 5.1: Heavy quark energy shift and mass renormalisation for the "on-lyH0" action. Results for masses $aM \geq 4.0$ use stability parameter $n = 1$, whilst all other results use $n = 2$.

I give results for highly-improved NRQCD with Symanzik-improved gluons in Table 5.2. I use 12 VEGAS iterations and 5×10^4 function evaluations (15×10^4 for Z_M), which required about 20 minutes on 12 processors.

I use a gluon mass of $a^2 \lambda^2 = 10^{-6}$ as an infrared regulator for the infrared finite mass renormalisation and energy shift. Extrapolation to zero gluon mass is not required, as my results exhibit no dependence on the gluon mass for $a^2 \lambda^2 \lesssim 10^{-4}$. I show only the infrared finite contributions to the wavefunction renormalisation in Table 5.1.

5.1.4 Tadpole improvement

The one-loop analytic results for the tadpole corrections to the heavy quark energy shift, $E_0^{u_0}$, are given in [47] and [89]:

$$E_0^{u0,(1)} = -\left[1 + \frac{6 + c_5}{2aM} - \frac{3}{2}\left(\frac{c_1}{a^3M^3} + \frac{c_6}{2na^2M^2}\right)\right]u_0^{(2)},$$

$$Z_M^{u0,(1)} = -\left[1 - \frac{3}{2naM} - \frac{c_5}{3} + 3\left(\frac{c_1}{a^2M^2} + \frac{c_6}{2naM}\right)\right]u_0^{(2)}. \qquad (5.12)$$

aM_Q	n	E_0	Z_M	Z_ψ^{finite}
5.40	1	-2.128(3)	0.551(3)	-0.015(2)
5.00	1	-2.167(3)	0.585(3)	-0.019(2)
4.00	1	-2.224(3)	0.719(3)	-0.145(2)
4.00	2	-2.222(3)	0.730(3)	-0.144(2)
2.80	2	-2.366(3)	1.030(3)	-0.333(3)
2.50	2	-2.424(3)	1.150(3)	-0.400(3)
2.50	4	-2.421(3)	1.163(3)	-0.394(4)
1.95	2	-2.562(3)	1.522(4)	-0.605(4)
1.95	4	-2.550(3)	1.524(4)	-0.599(4)
1.88	2	-2.580(3)	1.584(4)	-0.636(4)
1.88	4	-2.574(3)	1.592(4)	-0.629(4)
1.60	4	-2.670(3)	1.920(4)	-0.800(4)

Table 5.2: NRQCD renormalisation parameters: E_0, Z_M and the infrared finite contribution to the wavefunction renormalisation, Z_ψ. I show results for highly-improved NRQCD action with Symanzik-improved gluons.

The tadpole improvement factor vanishes for the wavefunction renormalisation.

I show tadpole improved results for highly-improved NRQCD in Table 5.3.

aM_Q	n	E_0	Z_M
5.40	1	-0.918(3)	-0.026(3)
5.00	1	-0.904(3)	-0.032(3)
4.00	1	-0.870(3)	0.078(3)
4.00	2	-0.850(3)	0.089(3)
2.80	2	-0.765(3)	0.243(3)
2.50	2	-0.741(3)	0.290(3)
2.50	4	-0.715(3)	0.303(3)
1.95	2	-0.691(3)	0.430(4)
1.95	4	-0.642(3)	0.432(4)
1.88	2	-0.682(3)	0.447(4)
1.88	4	-0.637(3)	0.455(4)
1.60	4	-0.608(3)	0.541(4)

Table 5.3: Tadpole corrected NRQCD renormalisation parameters, E_0, Z_M. The tadpole correction vanishes for the wavefunction renormalisation. I show results for highly-improved NRQCD action with Symanzik-improved gluons and include tadpole improvement corrections.

5.1.5   Comparison to the literature

In Table 5.4 I show results for the heavy quark energy shift, mass renormalisation and infrared finite contribution to the wavefunction renormalisation, taken from [47]. The data in Table 5.4 use the "onlyH0" and highly-improved NRQCD actions. We can see that my results, in Tables 5.1 and 5.2 are in excellent agreement with the results of [47].

Action	E_0	Z_M	Z_ψ^{finite}
"onlyH0"	-2.9851(24)	-0.1232(34)	1.1348(38)
highly-improved	-2.36685(40)	-0.3364(74)	1.0183(14)

Table 5.4: NRQCD renormalisation parameters from [47] for comparison. I show only the infrared finite contribution to the wavefunction renormalisation, Z_ψ^{finite}. All results use $aM = 2.8$ and $n = 2$.

Mass	n	E_0	Z_M	Z_ψ^{finite}
5.40	1	0.917(1)	-0.026(4)	-0.016(3)
4.00	2	0.850(1)	0.082(4)	-0.142(3)
2.80	2	0.767(1)	0.235(4)	-0.338(3)
2.10	4	0.666(1)	0.387(4)	-0.539(3)
1.95	2	0.689(1)	0.421(4)	-0.611(3)
1.95	4	0.646(1)	0.428(4)	-0.603(3)
1.60	4	0.609(1)	0.543(4)	-0.797(3)
1.20	6	0.609(1)	0.732(4)	-1.184(3)
1.00	6	0.758(1)	0.859(4)	-1.545(3)

Table 5.5: NRQCD renormalisation parameters from [89] for comparison. I show only the infrared finite contribution to the wavefunction renormalisation, Z_ψ^{finite}. All results use the fully improved NRQCD action with Symanzik-improved gluons and include tadpole corrections to E_0 and Z_M.

In Table 5.5 I show results for the heavy quark energy shift, mass renormalisation and infrared finite contribution to the wavefunction renormalisation from [89]. These results use highly-improved NRQCD with Symanzik-improved gluons and include tadpole corrections. We can see that my results, in Tables 5.1 and 5.2, are also in excellent agreement with the results of [89].

I use the wavefunction renormalisation results as part of my matching calculation of the heavy-light current in Chapter 6.

5.2   Renormalisation parameters at two-loops

The one-loop results presented above are a preliminary cross-check of the routines I wrote to obtain the main result of this chapter: the heavy quark energy shift at two-loops. Combined with my verification of the Ward identity for the fermionic contributions to the gluon selfenergy, which I discuss in Appendix C, these two tests provide a stringent check of my two-loop routines. This computation is, to the best of my knowledge, the first two-loop calculation undertaken in NRQCD.
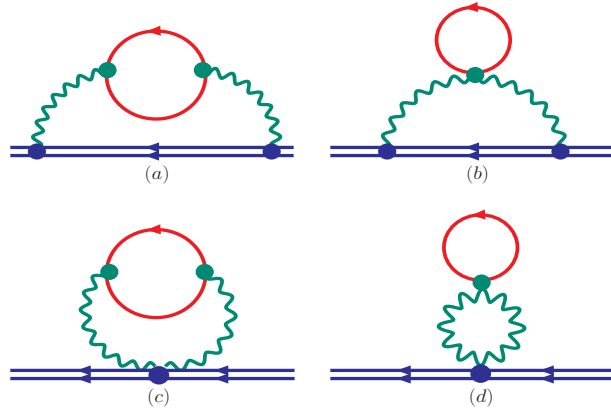
Figure 5.2: Fermionic contributions to E_0 and Z_M, calculated using automated lattice perturbation theory. Blue lines are heavy quarks, green are gluons and red are sea quarks. I give numerical results for each of these diagrams in Tables 5.6 to 5.8. I denote each contribution using column headings in those tables as follows: diagram (a) is the Rainbow-Bubble column; diagram (b) the Rainbow-Tadpole; diagram (c) the Tadpole-Bubble; and diagram (d) the Tadpole-Tadpole.

5.2.1 The fermionic contributions

I show the two-loop fermionic contributions to the heavy quark selfenergy in Figure 5.2. Applying the same method as the two-loop tadpole improvement factor calculation in Chapter 4, I extended the one-loop routines to two-loops using the `HPsrc` module `gluon_sigma`. I describe this module in more detail in Section 4.1 and review the gluon selfenergy more fully in Appendix C.

I calculated the heavy quark energy shift, E_0, at three different heavy quark masses, $aM = 2.50$, $aM = 1.88$ and $aM = 1.72$. The heaviest mass corresponds to the "coarse" lattices used by the HPQCD collaboration [93] and the lighter two masses correspond to the "fine" lattices used by the HPQCD collaboration in [85] and [93] respectively.

5.2.2 Energy shift results

I used three different sets of actions to calculate the energy shift, with either five or nine different light quark masses, between $am_q = 0.01$ and $am_q = 0.30$,

for each set of actions. I extrapolated the results to zero light quark mass using a function quadratic in the light quark mass. I plot the light quark mass dependence and the extrapolation to zero mass for each set of actions listed below in Figure 5.3. I plot results for a single heavy quark mass $aM = 2.50$ to serve as an illustration of the extrapolations. I use the ABCBA NRQCD operator ordering for the results with ASQTad and HISQ light quarks. The uncertainties are smaller than the size of the data points in Figure 5.3. I also show the light quark mass fits for corresponding to each set of actions.

I used a gluon mass as the infrared regulator, which, in general, should be avoided for two-loop calculations. However, in this case a gluon mass regulator is appropriate because there are no ghost contributions. The sets of actions I used are as follows:

- Davies and Thacker NRQCD action, Equation (4.15), with unimproved Wilson gluons and unimproved staggered light quarks, Table 5.6. I used 10^7 function evaluations for the tadpole results in columns three and four, which took approximately 1.5 hours on 128 processors, and 10^8 function evaluations for the rainbow results in columns five and six, which took about eight hours on 128 processors. I describe my notation, that is, my use of the terms "rainbow", "tadpole" and "bubble", in the caption to Table 5.6.

- Highly-improved NRQCD, Equation (2.66), with Symanzik-improved gluons and ASQTad light quarks. I used 10^7 function evaluations for the tadpole diagram results, in columns two and three of Table 5.7 and three and four of Table 5.9. I used 25×10^8 function evaluations for the rainbow diagrams in columns four and five of Table 5.7 and fix and six of Table 5.9. The tadpole diagram contributions took about six hours on 32 processors and the rainbow contributions approximately 23 hours on 64 processors. I give results for both the kernel ordering shown in Equation (2.66), which I denote ABCBA, where $A = (1 - \delta H/2)$, $B = (1 - H_0/2n)^n$ and $C = U^\dagger$, in Table 5.7 and an alternative ordering BACAB in Table 5.9. The ordering BACAB corresponds to the action used by the HPQCD collaboration in their lattice NRQCD simulations

[93].

- Highly-improved NRQCD with Symanzik-improved gluons and HISQ light quarks, Table 5.8. I used 10^8 function evaluations for the tadpole diagram results, in columns two and three, and $25{\times}10^8$ function evaluations for the rainbow diagrams in columns four and five. The tadpole diagram contributions took around three hours on 128 processors and the rainbow contributions about 18 hours on 256 processors. The action kernel ordering was ABCBA.

aM	am_q	Tadpole		Rainbow		Total
		Tadpole	Bubble	Tadpole	Bubble	
	0.30	0.4985(3)	-0.40691(8)	11.934(3)	-11.860(3)	0.166(4)
	0.20	0.5127(3)	-0.41332(8)	12.280(3)	-12.194(3)	0.185(4)
	0.15	0.5182(3)	-0.4156(3)	12.408(3)	-12.315(3)	0.196(4)
2.50	0.10	0.5221(3)	-0.4167(3)	12.505(3)	-12.406(3)	0.204(4)
	0.05	0.5244(3)	-0.4176(3)	12.560(3)	-12.455(3)	0.212(4)
	0.01	0.5251(3)	-0.41728(8)	12.579(3)	-12.468(4)	0.219(4)
	0.0	0.5250(2)	-0.4176(2)	12.575(3)	-12.470(2)	0.2217(8)
	0.30	0.5845(3)	-0.4766(3)	11.866(2)	-11.799(2)	0.176(3)
	0.20	0.6012(3)	-0.4841(3)	12.210(2)	-12.131(3)	0.196(3)
	0.15	0.6077(3)	-0.4863(3)	12.337(2)	-12.251(3)	0.207(3)
1.88	0.10	0.6123(3)	-0.4878(3)	12.430(2)	-12.373(3)	0.212(3)
	0.05	0.6149(3)	-0.4886(3)	12.488(2)	-12.389(3)	0.225(4)
	0.01	0.6158(3)	-0.4886(3)	12.506(2)	-12.402(3)	0.231(4)
	0.0	0.6157(2)	-0.4891(2)	12.502(3)	-12.418(1)	0.233(1)

Table 5.6: Light quark rainbow and tadpole diagram results for the heavy quark selfenergy at heavy quark mass $aM = 1.88$ and $aM = 2.50$ for six light quark masses. Uncertainties for the individual diagrams in columns three to six are statistical errors from numerical integration, whilst uncertainties for the totals given in column seven are the errors from each contribution added in quadrature. The results with $am_q = 0.0$ are extrapolations to zero light quark mass. All results use the "onlyH0" NRQCD action with unimproved staggered light quarks. I give the diagrams in Figure 5.2. The main headings "Tadpole" and "Rainbow" refer to the one-loop structure of the Feynman diagrams, whilst the secondary headings "Tadpole" and "Bubble" indicate the structure of the fermionic insertions in the dressed gluon propagator. Thus the four contributions in Figure 5.2 correspond to the column headings as follows: diagram (a) is the Rainbow-Bubble column; diagram (b) the Rainbow-Tadpole; diagram (c) the Tadpole-Bubble; and diagram (d) the Tadpole-Tadpole.

am_q	Tadpole		Rainbow		Total
	Tadpole	Bubble	Tadpole	Bubble	
0.30	0.5528(3)	-0.3900(1)	11.498(2)	-11.426(2)	0.235(3)
0.25	0.5593(3)	-0.3930(2)	11.630(2)	-11.553(2)	0.243(3)
0.20	0.5649(3)	-0.3953(2)	11.741(2)	-11.658(2)	0.253(3)
0.15	0.5693(3)	-0.3970(2)	11.828(2)	-11.740(2)	0.260(3)
0.10	0.5726(3)	-0.3980(3)	11.891(1)	-11.797(2)	0.269(3)
0.08	0.5734(3)	-0.3982(3)	11.911(2)	-11.814(3)	0.272(3)
0.05	0.5744(3)	-0.3984(2)	11.931(2)	-11.830(3)	0.277(3)
0.03	0.5748(3)	-0.3984(2)	11.939(2)	-11.836(3)	0.279(3)
0.01	0.5750(3)	-0.3984(2)	11.943(2)	-11.838(3)	0.282(3)
0.0	0.5750(5)	-0.3988(2)	11.9416(8)	-11.8422(8)	0.285(1)

Table 5.7: Light quark rainbow and tadpole diagram results for the heavy quark selfenergy at heavy quark mass $aM = 2.50$ for nine light quark masses. All results use the full NRQCD action, but with operator ordering ABCBA, with ASQTad light quarks. See the caption beneath Table 5.6 for full explanation of the data.

am_q	Tadpole		Rainbow		Total
	Tadpole	Bubble	Tadpole	Bubble	
0.30	0.3674(3)	-0.3766(3)	11.377(3)	-11.434(1)	-0.066(3)
0.25	0.3715(3)	-0.3798(3)	11.505(3)	-11.557(1)	-0.060(3)
0.20	0.3750(3)	-0.3823(3)	11.609(3)	-11.658(1)	-0.056(3)
0.15	0.3777(3)	-0.3841(3)	11.692(3)	-11.736(1)	-0.050(3)
0.10	0.3795(3)	-0.3850(3)	11.751(3)	-11.790(1)	-0.046(3)
0.08	0.3802(3)	-0.3855(3)	11.769(3)	-11.809(1)	-0.045(3)
0.05	0.3809(3)	-0.3857(3)	11.783(3)	-11.822(1)	-0.044(3)
0.03	0.3811(3)	-0.3857(3)	11.794(3)	-11.826(1)	-0.037(3)
0.01	0.3812(3)	-0.3857(3)	11.799(3)	-11.828(1)	-0.034(3)
0.0	0.38119(4)	-0.3860(1)	11.7961(9)	-11.8346(9)	-0.035(1)

Table 5.8: Light quark rainbow and tadpole diagram results for the heavy quark selfenergy at heavy quark mass $aM = 2.50$ for nine light quark masses. All results use the full NRQCD action with HISQ light quarks. See the caption beneath Table 5.6 for full explanation of the data.

aM	am_q	Tadpole		Rainbow		Total
		Tadpole	Bubble	Tadpole	Bubble	
2.50	0.30	0.5600(3)	-0.3905(2)	11.493(2)	-11.425(2)	0.237(3)
	0.25	0.5626(3)	-0.3935(2)	11.625(2)	-11.552(2)	0.242(3)
	0.20	0.5681(3)	-0.3958(2)	11.735(2)	-11.657(2)	0.250(3)
	0.15	0.5726(3)	-0.3974(2)	11.823(2)	-11.738(2)	0.260(3)
	0.10	0.5758(3)	-0.3984(2)	11.886(2)	-11.797(3)	0.266(4)
	0.08	0.5767(3)	-0.3986(2)	11.905(2)	-11.813(3)	0.270(4)
	0.05	0.5777(3)	-0.3988(2)	11.925(2)	-11.830(3)	0.274(4)
	0.03	0.5782(3)	-0.3988(2)	11.934(2)	-11.835(2)	0.278(3)
	0.01	0.5784(3)	-0.3988(2)	11.938(2)	-11.837(2)	0.281(3)
	0.0	0.5779(6)	-0.3991(1)	11.9363(8)	-11.8411(8)	0.2823(6)
1.88	0.30	0.6477(4)	-0.4549(3)	11.413(2)	-11.356(2)	0.250(3)
	0.25	0.6554(4)	-0.4584(3)	11.543(2)	-11.483(2)	0.257(3)
	0.20	0.6618(4)	-0.4610(3)	11.625(2)	-11.558(2)	0.268(3)
	0.15	0.6670(4)	-0.4629(3)	11.740(2)	-11.669(2)	0.275(3)
	0.10	0.6708(4)	-0.4640(3)	11.803(2)	-11.727(3)	0.283(4)
	0.08	0.6718(4)	-0.4643(3)	11.822(2)	-11.743(3)	0.287(4)
	0.05	0.6730(4)	-0.4645(3)	11.842(2)	-11.760(3)	0.291(4)
	0.03	0.6735(4)	-0.4645(3)	11.850(2)	-11.765(3)	0.294(4)
	0.01	0.6738(4)	-0.4645(3)	11.854(2)	-11.767(3)	0.296(4)
	0.0	0.6737(1)	-0.4649(2)	11.852(4)	-11.767(6)	0.2991(7)
1.72	0.30	0.6814(4)	-0.4787(3)	11.382(2)	-11.331(2)	0.254(3)
	0.25	0.6895(4)	-0.4823(3)	11.512(2)	-11.457(2)	0.262(3)
	0.20	0.6963(4)	-0.4852(3)	11.622(2)	-11.562(2)	0.271(3)
	0.15	0.7017(4)	-0.4871(3)	11.709(2)	-11.644(3)	0.280(4)
	0.10	0.7038(4)	-0.4883(3)	11.772(2)	-11.701(3)	0.288(4)
	0.08	0.7056(4)	-0.4886(3)	11.790(2)	-11.717(3)	0.290(4)
	0.05	0.7080(4)	-0.4888(3)	11.810(2)	-11.733(3)	0.296(4)
	0.03	0.7088(4)	-0.4888(3)	11.818(2)	-11.739(3)	0.299(4)
	0.01	0.7086(4)	-0.4888(3)	11.822(2)	-11.740(3)	0.302(4)
	0.0	0.7082(3)	-0.4892(2)	11.821(1)	-11.745(1)	0.3041(3)

Table 5.9: Light quark rainbow and tadpole diagram results for the heavy quark selfenergy at heavy quark mass $aM = 1.88$ and $aM = 2.50$ for nine light quark masses. All results use the full NRQCD action, with operator ordering BACAB, with ASQTad light quarks. See the caption beneath Table 5.6 for full explanation of the data.
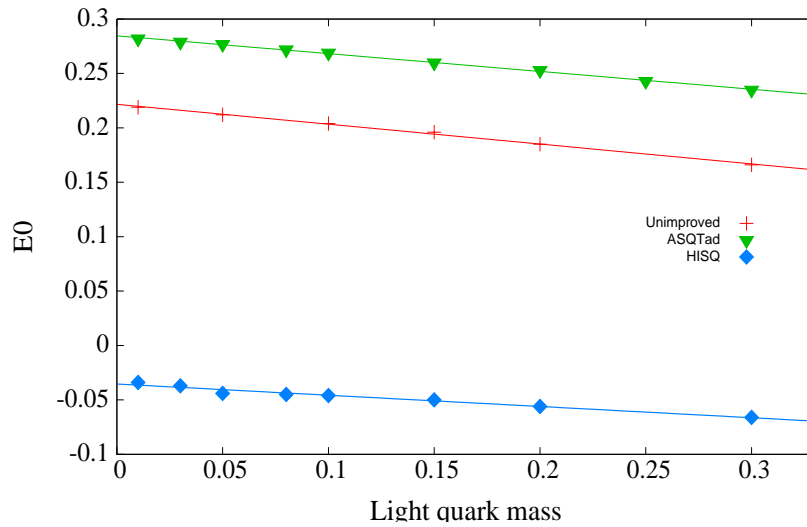
Figure 5.3: Plot of results for the light quark contributions to the heavy quark energy shift. The solid lines are the light quark mass fits corresponding to each set of results. I plot results for each set of actions, using the NRQCD operator ordering for the ASQTad and HISQ light quark data. I use heavy quark mass $aM = 2.5$ and gluon mass $a^2\lambda^2 = 10^{-6}$. Errorbars are smaller than the size of the data points. See the text in Section 5.2.2 for a full explanation of the sets of actions used in the plot.

5.2.3 Quenched high-β simulations

Calculating higher order loop corrections grows ever more difficult with each order, owing to the increasing number of diagrams and complicated vertex structure. In [94], Dimm *et al.* suggested an alternative method for extracting radiative corrections that avoids the difficulties associated with higher order perturbation theory. By measuring the heavy quark two-point function in the weak coupling regime and fitting the renormalisation parameters to a polynomial in α_s, the radiative contributions at each order can be obtained. This technique has been successfully implemented for a range of calculations [47], and in particular [86] and [90] demonstrate that the results obtained from the automated perturbative procedure match those from high-β simulations.

To evaluate the quenched contributions shown in Figure 5.4 Lee performed quenched simulations on $L^3 \times T$ lattices with temporal extent $T = 3L$ and spatial extents running from $L = 3$ to $L = 10$ [11]. He implemented
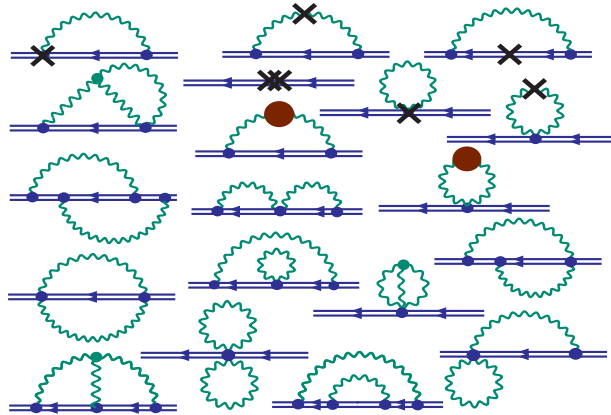
Figure 5.4: Quenched contributions to the heavy quark energy shift, extracted from high-β simulation. Blue lines are heavy quarks, green are gluons and crosses are counterterms. Large brown blobs represent the five gluon selfenergy diagrams. Feynman diagrams based on [95].

twisted boundary conditions to reduce finite size effects and tunnelling between QCD vacua. He used Coulomb gauge with a range of coupling values, from $\beta = 10$ up to $\beta = 120$. The number of independent configurations for each (β, L) was about 300. The energy shift and mass renormalisation were extracted using an exponential fit to the two point function parameterised by

$$G(p) = Z_\psi \exp\left(-\left[E_0 + \frac{a^2 \mathbf{p}^2}{Z_{\text{latt}} aM} + \ldots\right] t\right), \tag{5.13}$$

where the ellipsis indicates higher order terms included in the fits. The one-loop coefficient was extracted by fitting to a free parameter to compare with the perturbative result obtained on finite lattices by exact mode summation [96]. Table 5.10 demonstrates that the simulation fits reliably reproduces the exact one-loop perturbative results. To obtain the two-loop parameter, the one-loop coefficient was then constrained to its exact value from lattice perturbation theory.

Lee ran quenched simulations with and without tadpole improvement. Tadpole improvement significantly reduced the magnitude of the coefficients, from ~ 2.3 to ~ 0.7 at one-loop for E_0. Results from the quenched simulations were extrapolated to $L = \infty$ using a simultaneous multi-polynomial fit to the

L	E_0^{sim}	$E_0^{\text{pert. th.}}$
4	0.5295(16)	0.5312
6	0.5988(16)	0.6020
8	0.6369(12)	0.6362
10	0.6560(11)	0.6565
∞	0.7380(63)	0.7348(3)

Table 5.10: Sample quenched one-loop results from Lee, in column one, compared with the exact perturbative results computed by Ron Horgan in column two [5, 11, 96]. These results use a heavy quark mass of $aM = 2.8$ with stability parameter $n = 2$. There is no error on the perturbation theory calculation as it was obtained by mode summation. The error on the perturbation theory extrapolation to $L = \infty$ is estimated from the fit.

coupling constant, α_V, and the inverse lattice spatial extent, L^{-1}.

He used a fully-improved NRQCD action with radiatively improved coefficients in the action [11]. I present the one-loop values of the operator coefficients, c_i, in the fully-improved NRQCD action in Table 5.11. I define the coefficients in Section 2.4.1. I do not include c_2 or c_3 in Table 5.11, because current simulations do not include one-loop corrections for these coefficients.

aM	c_1 and c_6	c_4	c_5
2.50	$1 + 0.95\,\alpha_V\,(2.0/a)$	$1 + 0.78\,\alpha_V\,(\pi/a)$	$1 + 0.41\,\alpha_V\,(2/a)$
1.72	$1 + 0.766\,\alpha_V\,(1.8/a)$	$1 + 0.691\,\alpha_V\,(\pi/a)$	$1 + 0.392\,\alpha_V\,(1.4/a)$

Table 5.11: One-loop corrected coefficients in the fully-improved NRQCD action used for high-β simulations by Lee [11]. I define the coefficients in Section 2.4.1. I include both the explicit one-loop corrections and the BLM scale of the coupling constant in the V-scheme, α_V.

The coefficients in Table 5.11 correspond to the values chosen for the NRQCD lattice simulations undertaken by Dowdall and the HPQCD Collaboration [93]. The values for $c_1^{(1)}$, $c_5^{(1)}$ and $c_6^{(1)}$ were estimated from [47] and the value of $c_4^{(1)}$ from [14]. There is no contradiction in choosing two different

scales for the coupling constants in the perturbative corrections to the action. Each coefficient removes leading order errors induced by quantum fluctuations and so we choose a scale that best characterises those fluctuations. The scale of $q^\star \sim 2.0$ for the kinetic improvement operators was chosen based on [87], whilst the higher scale of $q^\star = \pi$ for the chromo-magnetic correction reflects the short-distance nature of that operator.

For the fully-improved NRQCD action, the selfenergy is

$$E_0 = E_0^{(1)}\alpha_V(3.33/a) + E_0^{(2),q}\alpha_V^2(3.33/a) + E_0^{(3),q}\alpha_V^2(3.33/a), \qquad (5.14)$$

where I give the tadpole-improved quenched coefficients, indicated by a superscript q, in Table 5.12. I give all results at a characteristic scale given by $q^\star = 3.33$, determined using the BLM procedure in [97].

aM	$E_0^{(1),q}$	$E_0^{(2),q}$	$E_0^{(3),q}$
2.50	0.6864(5)	1.35(10)	2.2(8)
1.72	0.5873(6)	1.56(11)	2.2(8)

Table 5.12: Quenched results from high-β simulations [11, 96]. The one-loop results are the exact perturbative results. Two- and three-loop results are extracted from a simultaneous polynomial fit to the strong coupling constant and lattice size. Uncertainties are from the fit. I evaluate all results at a characteristic scale of $q^\star = 3.33$.

5.2.4   Tadpole improvement

The one-loop analytic results for the tadpole corrections to the heavy quark energy shift, $E_0^{u_0}$, are given in Section 5.1.4. The effects of these one-loop contributions are included in the tadpole subtracted results from the high-β simulation, as are the quenched two-loop tadpole contributions. However, the two-loop fermionic contributions are not included in the high-β results, so I

add these in explicitly. The tadpole correction is

$$E_0^{u0,(2),f} = - \left[1 + \frac{7}{2aM} - \frac{3}{2} \left(\frac{1}{a^3 M^3} + \frac{1}{2na^2 M^2} \right) \right] u_0^{(4),P}, \qquad (5.15)$$

where I take the value of the fermionic contribution to the plaquette tadpole at two-loops, $u_0^{(4),P}$, from the extrapolation to zero light quark mass for the Symanzik-improved gluons with ASQTad light quarks in Table 4.2. The quenched contribution to the energy shift without tadpole improvement, E_0^q, is

$$E_0^q = 2.264(7) \qquad (5.16)$$

for the heavy quark mass $aM = 2.50$ and

$$E_0^q = 2.648(10) \qquad (5.17)$$

for the heavy quark mass $aM = 1.72$.

5.3   The b quark mass

Quark confinement ensures that quark masses are not physically measurable quantities, so the notion of quark mass is a theoretical construction. A wide range of quark mass definitions exist, often tailored to exploit the physics of a particular process. One common choice of quark mass is the pole mass, defined as the pole in the renormalised heavy quark propagator. However, the pole mass is a purely perturbative concept and suffers from infrared ambiguities known as renormalons [55, 56]. I discuss the role of renormalons in NRQCD in more detail in Section 3.2. To avoid these ambiguities, experimental results are usually quoted in the modified Minimal Subtraction ($\overline{MS}$) scheme, which is renormalon ambiguity free. Lattice calculations use the renormalon-free bare lattice mass. These different quark mass definitions must be matched to enable meaningful comparison. I match bare lattice quantities to the $\overline{MS}$ mass using the pole mass as an intermediate step. Any renormalon ambiguities cancel in the full matching procedure between the lattice quantities and the $\overline{MS}$ mass as I explicitly demonstrate in Section

5.3.2.

I extract the $\overline{MS}$ mass from lattice simulation data in a two-stage process. I first relate lattice quantities to the pole mass and then match the pole mass to the $\overline{MS}$ mass evaluated at a scale equal to the b quark mass.

5.3.1   Extracting the pole mass

I determine the pole mass by relating the heavy quark pole mass, M_{pole}, to the experimental Υ mass, $M_{\Upsilon}^{\mathrm{expt}} = 9.46030(26)$ GeV [8], using the heavy quark energy shift, E_0:

$$2M_{\mathrm{pole}} = M_{\Upsilon}^{\mathrm{expt}} - (E_{\mathrm{sim}}(0) - 2E_0). \tag{5.18}$$

Here $E_{\mathrm{sim}}(0)$ is the energy of the Υ meson at zero momentum, extracted from lattice NRQCD simulations. The quantity $(E_{\mathrm{sim}}(0) - 2E_0)$ corresponds to the "binding energy" of the meson in NRQCD.

I use values of $E_{\mathrm{sim}}(0)$ obtained from lattice NRQCD simulations run by the HPQCD collaboration on two different MILC ensembles. The first ensemble, with a tuned heavy quark mass of $aM = 2.50$, is a "coarse" MILC ensemble, with lattice spacing $a = 0.605(5)$ GeV^{-1}. The second ensemble, with a tuned heavy quark mass of $aM = 1.72$, is a "fine" MILC ensemble, with lattice spacing $a = 0.4292(32)$ GeV^{-1}. These heavy quark masses correspond to the kinetic mass, defined through the nonrelativistic kinetic energy, for the spin-average of the Υ and η_b mesons.

In these simulations, the lattice spacing was tuned using the HPQCD value for r_1, given by $r_1 = 0.3133(23)$ [93, 98]. Both ensembles use Symanzik-improved gluons with $2 + 1$ flavours of ASQTad sea quarks. Electromagnetic effects were ignored. For further details of the configurations see [22, 98].

In principle we could extract the quark mass by directly matching the pole mass to the bare lattice mass in physical units, $M_0(a)$, via the heavy quark mass renormalisation, Z_M,

$$M_{\mathrm{pole}} = Z_M(\mu a, M_0(a))M_0(a). \tag{5.19}$$

However, it proved difficult to reliably extract the quenched two-loop mass renormalisation from high-β simulations and so I do not extract the b quark mass in this way.

5.3.2 Matching the pole mass to the $\overline{MS}$ mass

The mass renormalisation relating the pole mass to the $\overline{MS}$ mass, $M_{\overline{MS}}$, evaluated at some scale μ, is given by

$$M_{\overline{MS}}(\mu) = Z_{\text{cont}}^{-1}(\mu, M_{\text{pole}}) M_{\text{pole}}, \tag{5.20}$$

and has been calculated to three-loops in [99]. The result is

$$Z_{\text{cont}}^{-1}(M_{\text{pole}}, M_{\text{pole}}) = 1 - \frac{4}{3\pi} \alpha_{\overline{MS}} + \frac{1}{\pi^2} \left(1.0414 n_f - 14.3323 \right) \alpha_{\overline{MS}}^2 \tag{5.21}$$
$$+ \frac{1}{\pi^3} \left(-0.65269 n_f^2 + 26.9239 n_f - 198.7068 \right) \alpha_{\overline{MS}}^3,$$

where the coupling constant is evaluated at a scale equal to the pole mass.

Although the pole mass is plagued by renormalon ambiguities, these ambiguities cancel when lattice quantities are related to the $\overline{MS}$ mass. We can see that the renormalon ambiguities cancel when determining the pole mass from the energy shift, by equating Equations 5.18 and 5.19 and rearranging them to obtain

$$2(Z_M M_0(a) - E_0) = M_\Upsilon^{\text{expt}} - E_{\text{sim}}(0). \tag{5.22}$$

The two quantities on the right hand side of the equation are renormalon ambiguity free: M_Υ^{expt} is a physical quantity and $E_{\text{sim}}(0)$ is determined non-perturbatively from lattice simulations. Any renormalon ambiguities in the two power series, Z_M and E_0, on the left-hand side of the equation must therefore cancel.

This renormalon cancellation is also evident in the direct matching of the bare lattice mass to the $\overline{MS}$ mass,

$$M_{\overline{MS}}(\mu) = Z_M(\mu a, M_0(a)) Z_{\text{cont}}^{-1}(\mu, M_{\text{pole}}) M_0(a), \tag{5.23}$$

as both $M_{\overline{MS}}$ and M_0 are renormalon-free.

I combine Equations (5.18), (5.20) and (5.21) to obtain the final expression for the full matching between lattice quantities and the $\overline{MS}$ mass as

$$M_{\overline{MS}}(\mu) = \frac{1}{2}Z_{\text{cont}}^{-1}(\mu, M_{\text{pole}})\left[M_{\Upsilon}^{\text{expt}} - (E_{\text{sim}}(0) - 2E_0)\right]. \tag{5.24}$$

5.3.3 Results

I now have all the pieces in place to extract the b quark mass and here I collect them together to obtain my final result. First off, the perturbative results for the heavy quark energy shift, which is given by

$$E_0 = E_0^{(1)}\alpha_V(3.33/a) + \left(E_0^{(2),q} + n_f E_0^{(2),f}\right)\alpha_V^2(3.33/a) + E_0^{(3),q}\alpha_V^3(3.33/a), \tag{5.25}$$

where the coefficients $E_0^{(i),j}$ are given in Table 5.12 for the quenched results and in Table 5.9 for the fermionic contributions.

To extract the b quark mass, I first express the coupling constant in the V-scheme in terms of the coupling constant in the $\overline{MS}$ scheme, evaluated at the same scale $q^{\star}$, using the three-loop relation in [32, 33, 34]. I used the world-average value of $\alpha_{\overline{MS}}(M_Z^2) = 0.1184(7)$ GeV, with $M_Z = 91.1876(21)$ GeV, both taken from the Particle Data Group [8], to set the absolute scale for the coupling constant. I then run the coupling constant to the scale of the heavy quark mass, which is yet to be determined. Finally I use `Mathematica` to self-consistently solve the equation

$$M_{\overline{MS}}(M_{\overline{MS}}) = \frac{1}{2}Z_{\text{cont}}^{-1}(M_{\overline{MS}}, M_{\text{pole}})\left[M_{\Upsilon}^{\text{expt}} - (E_{\text{sim}}(0) - 2a^{-1}E_0)\right], \tag{5.26}$$

where I express the energy shift, E_0, in terms of the coupling constant in the $\overline{MS}$ scheme, evaluated at $M_{\overline{MS}}$.

I summarise all the data necessary to extract the b quark mass in the $\overline{MS}$ scheme in Tables 5.13 and 5.14. In Table 5.13 I combine the quenched energy shift results in Table 5.12 with the fermionic contributions in Table 5.9. I include the fermionic contribution to the tadpole improvement at two-loops in column five. This contribution is given in Equation (5.15). In Table 5.14 I

aM	$E_0^{(1)}$	$E_0^{(2)}$	$E_0^{(3),q}$	$E_0^{u0,(2),f}$
2.50	0.6864(5)	$1.35(10) + 0.2823(6)n_f$	2.2(8)	$-0.158532(16)$
1.72	0.5873(6)	$1.56(11) + 0.3041(3)n_f$	2.2(8)	$-0.166056(17)$

Table 5.13: Perturbative data required to extract $\overline{MS}$ mass. The quenched results, indicated by superscript q, are from high-β simulations [11, 96]. I calculate fermionic contributions using automated lattice perturbation theory. The one-loop data are the exact perturbative results extrapolated to infinite lattice size. The two-loop results include both quenched and fermionic contributions. The three-loop values include only quenched results. I evaluate all results at a characteristic scale of $q^\star = 3.33$.

present the nonperturbative simulation results for $E_{\rm sim}$ and the corresponding inverse lattice spacing, both expressed in GeV.

aM	$E_{\rm sim}$	a^{-1}
2.50	0.7397(66)	1.652(14)
1.72	0.96417(13)	2.330(17)

Table 5.14: Simulation data required to extract $\overline{MS}$ mass. All values extracted from nonperturbative simulations by the HPQCD collaboration on MILC ensembles [93].

I obtain

$$M_{\overline{MS}}\left(M_{\overline{MS}}\right) = 4.185(26) \text{ GeV}, \qquad (5.27)$$

for a heavy quark mass of $aM = 2.50$, and

$$M_{\overline{MS}}\left(M_{\overline{MS}}\right) = 4.154(27) \text{ GeV}, \qquad (5.28)$$

for a heavy quark mass of $aM = 1.72$. I quote only the uncertainty associated with statistical and perturbative errors in these results. I discuss these uncertainties in the next section and, in particular, describe two approaches to estimating the systematic uncertainties due to lattice artifacts.

5.3.4 The error budget

Broadly, there are three main sources of uncertainty in my result for the b quark mass: systematic errors, statistical errors and perturbative errors. I expect the $\mathcal{O}(\alpha_s^3)$ perturbative contributions to dominate the error in my result. In this section I discuss each of these sources of error in turn. I tabulate my estimated error budget in Table 5.15. I estimate all sources of uncertainty by carrying out the analysis discussed in the previous section with a range initial parameters specified by the uncertainties in those parameters. I take the resulting range of b quark masses as the estimate of the uncertainty due to the individual parameter concerned. Thus, for example, I calculate the b quark mass with the inverse lattice spacing equal to its quoted value, $a^{-1} = 1.652$ GeV. This is my final result for the mass of the b quark. I then recalculate the mass with the inverse lattice spacing equal to its maximum value $a^{-1} = 1.666$ GeV. The difference between the new result that I obtain for the b quark mass and my original value for the b quark mass provides an estimate of the uncertainty due to the error in the lattice spacing.

Statistical errors Statistical errors arise in the nonperturbative and experimental input values, E_{sim} and $M_{\Upsilon}^{\text{expt}}$, and in the contributions at each order in the expansion of the heavy quark energy shift, E_0. I do not provide a further breakdown of the errors in $M_{\Upsilon}^{\text{expt}}$, because the associated uncertainties are negligible. I do not have a breakdown of the errors associated with E_{sim} and so include the total uncertainty in this quantity as simply "statistical" error. The corresponding relative error is $\sim$3 MeV, which is less than 0.1% of my final result for the b quark mass. The uncertainty in the lattice spacing for the nonperturbative simulations leads to an error in the b quark mass of less than 0.1%. In Table 5.15 I denote uncertainty due to the error in the value of the lattice spacing as Δa^{-1}. This should not be confused with the systematic error due to lattice artifacts.

Statistical errors arise from the numerical evaluation of each contributions to the heavy quark energy shift. The uncertainty in the one-loop coefficient is from the extrapolation to infinite volume and the associated error in the

b quark mass is $\sim$1 MeV or 0.1% of the final result. The uncertainties in the two-loop and three-loop quenched coefficients of E_0 arise from the simultaneous fit to the lattice size and the strong coupling constant. The statistical error in the two-loop fermionic coefficient is due to the numerical evaluation of the Feynman diagrams and the extrapolation to zero light quark mass.

Systematic errors   Systematic uncertainties arise from the nonzero lattice spacing. With data only available for two lattice spacings, there are two methods to estimate the lattice artifact errors.

The two results in Equations (5.27) and (5.28) agree within the quoted uncertainties. At this level of precision, then, I assume that lattice artifact errors are negligible. In this case, I simply average over the two results, and use their standard deviation as my estimate of the systematic errors. I obtain

$$M_{\overline{MS}}\left(M_{\overline{MS}}\right) = 4.170(27)(22) \text{ GeV}, \tag{5.29}$$

where the first uncertainty is statistical/perturbative and the second is systematic. I assume that the statistical/perturbative errors are correlated between the results in Equations (5.27) and (5.28) and therefore do not combine the two errors in quadrature, but quote a single value.

The NRQCD quantum effective action is an expansion in the lattice spacing, the strong coupling constant and the inverse heavy quark mass. As an alternative method for estimating systematic uncertainties, I assume only that the NRQCD action is improved to sufficient order in the lattice spacing and coupling constant that the leading order correction is a polynomial in the inverse heavy quark mass. The leading order in this expansion is $1/(a^2 M^2)$. I then estimate the lattice artifact errors by fitting the results in Equations (5.27) and (5.28) to a function of the form

$$F(M) = M_0 + \frac{A}{a^2 M^2}. \tag{5.30}$$

I then take my final result to be equal to the value of M_0 from my fit. I obtain

$$M_{\overline{MS}}\left(M_{\overline{MS}}\right) = 4.213(27) \text{ GeV}. \tag{5.31}$$

In this case I do not quote a systematic uncertainty from the fitting procedure because I fit to two parameters with two data points.

A more systematic discussion of the leading contributions missing from the expansion of the quantum effective action is also required. I have not demonstrated rigorously that the leading order term in the expansion is quadratic in the inverse heavy quark mass and a more refined analysis would be preferable and may include non-leading terms. This, of course, requires results from different ensembles, that is, at different heavy quark masses. This work is underway.

Perturbative errors   I include all known three-loop contributions in my calculation of the b quark mass. These contributions come from:

- the quenched heavy quark energy shift;

- matching α_V to $\alpha_{\overline{MS}}$;

- matching the pole mass to the $\overline{MS}$ mass;

- perturbative running of the $\overline{MS}$ mass to the desired scale.

The three-loop fermionic contribution to the energy shift is unknown, so I estimate the error due to this contribution as $\mathcal{O}(1 \times \alpha_{\overline{MS}}^3)$. The corresponding error in the b quark mass is ~ 19 MeV, that is, a relative uncertainty of approximately 0.5%.

The unknown fermionic contributions are the only unknown source of uncertainty at three-loops in my result. In principle these effects can be calculated using automated lattice perturbation theory. However, there are a large number of diagrams to evaluate, many of which are likely to have complicated pole structures and possible divergences (the energy shift is infrared finite, but individual diagrams may have divergences that ultimately cancel). The complexity of such a calculation would be considerable.

5.3.5   Comparison to the literature

My results for the b quark mass improves on the previous, preliminary, result that we presented in [5] in a number of ways. In that work, we obtained a

Class of error	Error	Estimated uncertainty $(aM = 2.50)$		Estimated uncertainty $(aM = 1.72)$	
		MeV	%	MeV	%
Statistical	M_Υ^{expt}	0.1	$\ll 0.1$	0.1	$\ll 0.1$
	E_{sim}	3.0	< 0.1	0.1	$\ll 0.1$
	Δa^{-1}	1.2	< 0.1	1.5	< 0.1
Perturbative	$E_0^{(1)}$	0.2	$\ll 0.1$	0.3	$\ll 0.1$
	$E_0^{(2),q}$	8.3	~ 0.2	11.5	~ 0.3
	$E_0^{(2),f}$	0.3	$\ll 0.1$	0.2	$\ll 0.1$
	$E_0^{(3),q}$	15.4	~ 0.4	15.0	~ 0.4
	$E_0^{(3),f}$	$\sim$19.3	~ 0.5	$\sim$18.8	~ 0.5
Systematic	a	31	~ 0.7	31	~ 0.8

Table 5.15: The b quark mass error budget: estimated uncertainties in my calculation of the b quark mass from lattice NRQCD and lattice perturbation theory. The entries for the "systematic" error are independent of the heavy quark mass. I describe each source of uncertainty in more detail in Section 5.3.4.

value of

$$M_{\overline{MS}}\left(M_{\overline{MS}}\right) = 4.25(12) \text{ GeV} \qquad (5.32)$$

for the b quark mass.

Firstly, the new results remove a number of discrepancies between the nonperturbative data and the perturbation theory results. I used a value for E_{sim} based on simulations using an NRQCD action with a stability parameter of $n = 4$. The perturbation theory results, on the other hand, used an NRQCD action with a stability parameter $n = 2$. I had previously calculated the fermionic contributions with HISQ light quarks, which significantly reduced the fermionic contribution. Furthermore, the lattice NRQCD simulation used Landau tadpoles [85, 98] whilst the quenched high-β simulations

used plaquette tadpoles [11]. With the new results, plaquette tadpoles were used in both simulations and I include the fermionic contributions to the two-loop tadpole correction for the heavy quark energy shift, which had not previously been computed. Although the error arising from these discrepancies is likely to be negligible, and certainly much less than the dominant $\mathcal{O}(\alpha_s^3)$ error, removing as many sources of error as possible is obviously desirable.

The NRQCD simulations from which the value of E_{sim} was extracted have also been improved. Previous results used an NRQCD action without radiative improvements to the coefficient of the chromo-magnetic operator, c_4, which is included in the new result. The lattice spacing determination has also been improved [85, 98]. The new results use higher statistics and determine the value of r_1/a from a combination of methods to reduce systematic uncertainties [93].

In my new results I use simulation data from two different ensembles, allowing me to estimate the systematic uncertainty arising from lattice artifact errors under two different sets of assumptions. Both results are in agreement within errors. This analysis was not possible with the preliminary result presented in [5].

Finally, I have analysed the uncertainties in my new result more rigorously and provided an error budget for individual contributions. I had not previously analysed the individual sources of error in detail.

My results are a significant improvement on the previous determination of the b quark mass from lattice NRQCD simulations by the HPQCD collaboration [85], as can be seen in Figure 5.5. The dominant source of error in that calculation was the contribution from the two-loop heavy quark energy shift and the total error quoted for the result was approximately seven percent. All two-loop contributions have been included in the values given in Equations (5.27) and (5.28) and the errors are reduced to less than one percent, in line with other recent determinations.

In Figure 5.5, I also present a number of recent determinations of the b quark mass. Two of these are from perturbative QCD sum rules, given in [100, 101] and [92]. These results are in excellent agreement with quoted

uncertainties of very similar magnitude, although the errors are about 30% larger than the errors in my result. Of course, these values are not extracted from nonperturbative simulations, but do use input from experimental data.

I show results from three different lattice simulations in Figure 5.5. All results are in agreement within the quoted uncertainties. The most precise determination is by the HPQCD collaboration, using HISQ quarks for the b quark and extrapolating up to the physical b quark mass [25]. This simulation used MILC configurations with $(2 + 1)$ flavours of ASQTad sea quarks.

I also present the result from the ETM collaboration using twisted mass Wilson quarks at four different lattice spacings and two species of sea quarks [102]. The final result is from the ALPHA collaboration [103]. They quote a preliminary result with a larger uncertainty than the other results in Figure 5.5. The ALPHA collaboration use HQET with $\mathcal{O}(1/M)$ corrections and two species of sea quarks, but do not give an indication of the errors from lattice artifacts.

The vertical line in Figure 5.5 is a weighted average of results from other work. This line serves to guide the eye only and does not include the results of this work from [5] or from this dissertation. I do not account for any correlations between results in this average. We can see that my new results are in good agreement with this average.

5.4   Conclusions and outlook

I have calculated the two-loop heavy quark energy shift in highly-improved NRQCD using a mixed approach combining quenched high-β simulations with lattice perturbation theory. This calculation was the first determination of any heavy quark parameter at two-loops in NRQCD and demonstrated the effectiveness of such an approach. My predictions of the b quark mass improves on the previous determination from lattice NRQCD simulations by the HPQCD collaboration. I significantly reduce the uncertainties in the final result by removing the dominant source of uncertainty in the previous calculation: the two-loop heavy quark energy shift. My results include an estimate of the systematic uncertainties arising from lattice artifact errors.
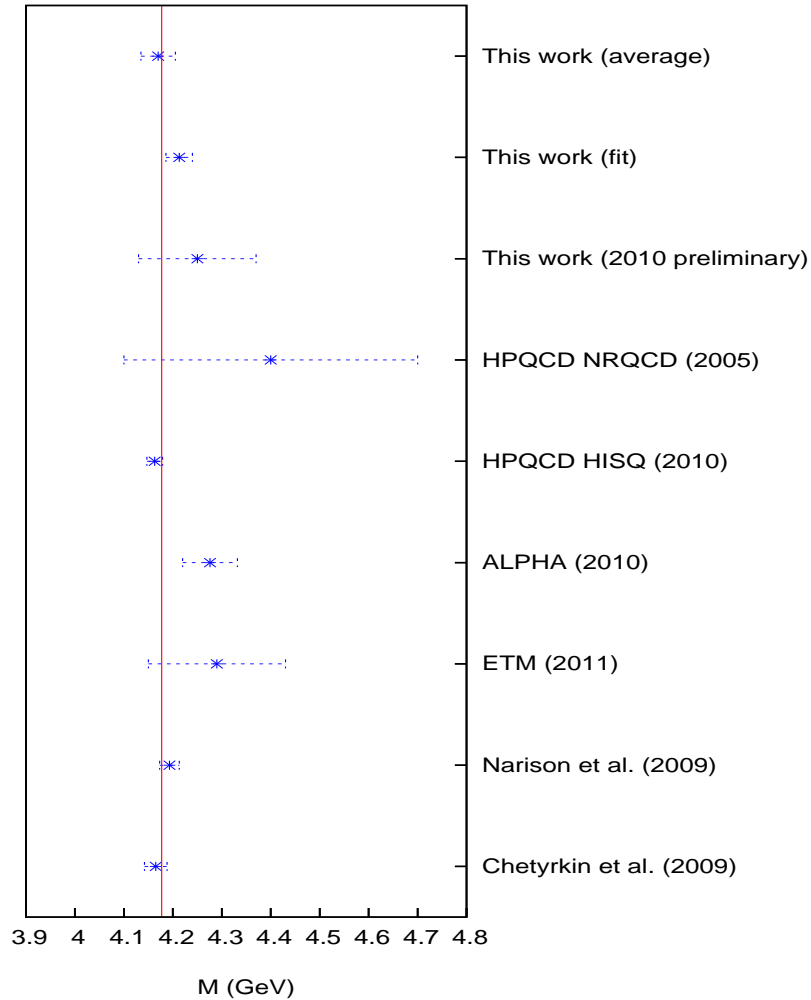
Figure 5.5: Recent results for the b quark mass. From top to bottom: this work, using an averaging procedure (see Section 5.3.4); this work, using a fitting procedure (see Section 5.3.4); the preliminary determination from this work [5]; HPQCD collaboration with NRQCD valence quarks [85]; HPQCD collaboration using HISQ valences quarks [25]; ALPHA collaboration using HQET [103]; ETM collaboration [102]; and QCD sum rules from Narison *et al.* [100, 101] and from Chetyrkin *et al.* [92]. The vertical line is to guide the eye and is my determination of the weighted average of the results, not including data from our preliminary determination in [5] or from this dissertation.

113

By including all two-loop perturbative effects I have brought the uncertainty in the final result into line with a number of other recent determinations of the b quark mass.

A complete analysis of the systematic uncertainty would require further simulation data from ensembles at different lattice spacings. This work is currently underway. The analysis of the high-β simulations will also be improved by using a larger number of ensembles and this development will improve further the precision of the three-loop contribution to the quenched heavy quark energy shift and thereby reduce the uncertainty in the b quark mass. Ultimately the three-loop fermionic contributions to the heavy quark energy shift would be required for a complete three-loop calculation, but this would require extensive developments of my code.

Chapter 6

Heavy-light currents

Electroweak processes are an important tool in understanding the Standard Model, serving as an input into tests of CKM matrix unitarity and CP violation, and as a probe for new physics. Hadronic matrix elements, which characterise the strong interaction dynamics of these processes, are a crucial ingredient in the calculation of the electroweak parameters.

Lattice QCD simulations enable nonperturbative determinations of hadronic matrix elements from first principles. These simulations require us to construct the electroweak lattice currents in terms of the appropriate lattice operators. We then match the lattice currents to their continuum counterparts order-by-order in the strong coupling constant to extract the correct continuum behaviour at the desired precision.

In this chapter I perturbatively match the temporal components of the heavy-light axial and vector currents in lattice NRQCD with massless HISQ light quarks to the corresponding currents in continuum QCD. I perform this matching at zero external quark momentum and include only leading order terms in the inverse heavy quark mass expansion. This calculation updates the matching calculation of [89], which used highly-improved NRQCD with massless ASQTad quarks for the lattice currents. My results are directly relevant for the nonperturbative determination of the f_B, f_{B_s} and f_{D_s} decay constants by the HPQCD collaboration using MILC lattices with HISQ sea quarks.

Before describing the matching calculation in detail, I first briefly review some of the background and motivation for this calculation.

6.1   Heavy-light decays and the CKM matrix

The three-generation Cabibbo-Kobayashi-Maskawa (CKM) matrix parameterises the weak interaction quark eigenstates in terms of the mixing of the

mass eigenstates [104, 105]. The CKM matrix,

$$V_{\text{CKM}} = \begin{pmatrix} V_{ud} & V_{us} & V_{ub} \\ V_{cd} & V_{cs} & V_{cb} \\ V_{td} & V_{ts} & V_{tb} \end{pmatrix}, \tag{6.1}$$

is unitary in the Standard Model and deviations from unitarity may indicate new physics. Tests of the unitarity of the CKM matrix are therefore of paramount importance in understanding the Standard Model. We can parameterise the CKM matrix using three real angles and one CP-violating phase. If this phase is non-zero, then weak interactions violate simultaneous charge (C) and parity (P) invariance. The standard choice of parameterisation for the CKM matrix is the Wolfenstein parameterisation [106], which uses $\lambda = |V_{us}| \approx 0.22$ as a small expansion parameter:

$$V_{\text{CKM}} = \begin{pmatrix} 1 - \frac{\lambda^2}{2} & \lambda & A\lambda^3(\rho - i\eta) \\ -\lambda & 1 - \frac{\lambda^2}{2} & A\lambda^2 \\ A\lambda^3(1 - \rho - i\eta) & -A\lambda^2 & 1 \end{pmatrix}. \tag{6.2}$$

Unitarity imposes constraints on the parameters of the CKM matrix that we can interpret geometrically as triangles in the complex plane. Only one of these triangles is not near-degenerate and the corresponding normalised constraint is

$$\frac{V_{ud}V_{ub}^*}{V_{cd}V_{cb}^*} + \frac{V_{td}V_{tb}^*}{V_{cd}V_{cb}^*} + 1 = 0. \tag{6.3}$$

I show this CKM triangle in Figure 6.1. The angle β is known to 1° precision from $B \to J/\psi K$ decays and precise determinations of $|V_{ub}|$ and $|V_{cb}|$ are therefore an integral component in over-constraining the CKM unitarity triangle [8]. The ultimate goal is to measure the three angles and the lengths of each of the sides and thus determine the apex of the CKM triangle (ρ, η) in as many ways as possible. Over-constraining the CKM triangle provides a stringent test of the three-generation Standard Model.

The CKM matrix elements $|V_{ub}|$ and $|V_{cb}|$ are experimentally determined from a number of different electroweak processes, including inclusive and ex-
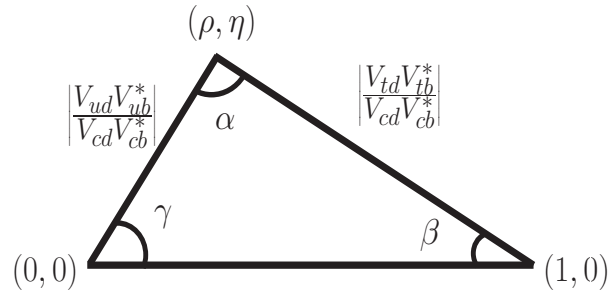
Figure 6.1: The CKM unitarity triangle in the complex plane.

clusive B decays and B meson mixing [8]. The CKM matrix elements must be extracted from strongly bound states and lattice QCD is required to calculate the hadronic matrix elements that characterise the strong interaction dynamics of the decays. There is currently a 2σ tension between the inclusive and exclusive determinations of $|V_{cb}|$ and the dominant uncertainties in these measurements are theoretical, so an improved understanding of the theoretical inputs is increasingly important. This requires high-precision lattice simulations.

The matrix element $|V_{ub}|$ is extracted experimentally from the exclusive semileptonic decay $\overline{B} \to \pi \ell \overline{\nu}_\ell$, which has differential decay rate

$$\frac{\mathrm{d}\Gamma}{\mathrm{d}q^2} = \frac{G_F^2}{24\pi^3}|V_{ub}|^2|p_\pi|^3|f_+(q^2)|^2 \tag{6.4}$$

in the limit that the light quark is massless. Here p_B is the momentum of the B meson and p_π the momentum of the pion in the B meson rest frame. The momentum transfer is $q = p_B - p_\pi$. The form factors f_+ and f_0 parameterise heavy-light matrix elements of the vector current, V^μ,

$$\langle \pi(p_\pi)|V^\mu|B(p_B)\rangle = f_+(q^2)\left[p_B^\mu + p_\pi^\mu - \frac{m_B^2 - m_\pi^2}{q^2}q^\mu\right]$$
$$+ f_0(q^2)\frac{m_B^2 - m_\pi^2}{q^2}q^\mu. \tag{6.5}$$

The axial vector current does not contribute to pseudoscalar-to-pseudoscalar decays [1].

117

The HPQCD collaboration has calculated these form factors using lattice QCD [1]. These simulations were run with $(2 + 1)$ flavours of ASQTad sea quarks and highly-improved NRQCD valence b quarks. Using experimental input from the BaBar, Belle and CLEO experiments, the authors obtained $|V_{ub}| = (3.55 \pm (0.25)_{\text{exp}} \pm (0.50)_{\text{theory}}) \times 10^{-3}$. The uncertainties are experimental and theoretical respectively and are dominated by the theoretical input.

Leptonic decays of heavy mesons also provide experimental methods for constraining the CKM matrix. For example, the ratio $|V_{td}/V_{ts}|$ involves the the decay constants f_B and f_{B_s}. These decays proceed via a virtual charged W boson and the decay width of such a process is given by

$$\Gamma(X \to \ell\nu) = \frac{G_F^2}{8\pi} f_X^2 m_\ell^2 m_X \left(1 - \frac{m_\ell^2}{m_X^2}\right)^2 |V_{q_1 q_2}|^2, \tag{6.6}$$

where X is a heavy hadron, such as a B, B_s or D_s meson and $|V_{q_1 q_2}|$ is the relevant CKM matrix element. In fact, leptonic decay modes occur for $\pi^\pm$ and $K^\pm$ mesons as well, but I restrict my discussion here to heavy quark mesons. We define the decay constant, f_X, through the hadronic matrix element

$$\langle 0|A_\mu|X(p)\rangle = p_\mu f_X. \tag{6.7}$$

The HPQCD collaboration has computed the decay constants f_{B_s} and f_{D_s} using NRQCD heavy quarks and $(2 + 1)$ flavours of ASQTad sea quarks [50, 107, 108, 109]. There is currently tension between the value of $|V_{cb}|$ determined from experimental measurements of $B^\pm \to \tau^\pm \nu$, presently in good agreement with the Standard Model, and from determinations using global fits to the CKM parameters [110].

Recent measurements of the branching ratios of the semileptonic decay $B \to D^{(*)}\tau\nu$, from which $|V_{ub}|$ can be determined, report a preliminary result nearly 2σ above the Standard Model prediction [9]. This decay proceeds via a $W^\pm$ boson, so if this discrepancy were to be confirmed, the excess would hint at the presence of a Beyond the Standard Model charged Higgs boson. These results, however, are very much preliminary findings.

Results from LHCb and the proposed SuperB factory will improve the experimental resolution of B decays by an order of magnitude and corresponding improvements in the theoretical inputs are required. The HPQCD collaboration are therefore calculating the decay constants f_{B_s} and f_{D_s} using NRQCD with HISQ sea quarks, which should improve the precision of the final results [111].

The calculations of the form factors, f_+ and f_0, and the decay constants, f_B and f_{B_s}, using HISQ light quarks both require new matching calculations to relate heavy-light currents on the lattice and in the continuum. In this chapter I discuss this calculation and present results for massless HISQ light quarks using currents at leading order in the inverse heavy quark mass.

6.2   The continuum current

The continuum axial-vector current is given by

$$A_\mu(x) = \overline{q}(x)\widehat{\gamma}_5\widehat{\gamma}_\mu h(x), \tag{6.8}$$

where $q(x)$ is the light quark field and $h(x)$ the heavy quark field. I denote the Euclidean Dirac matrices by $\widehat{\gamma}_\mu$. They are related to the Minkowski Dirac matrices, γ_μ, by

$$\widehat{\gamma}_0 = \widehat{\gamma}^0 = \gamma_0 = \gamma^0, \qquad \widehat{\gamma}_j = \widehat{\gamma}^j = i\gamma_j = -i\gamma^j, \tag{6.9}$$

and satisfy

$$\{\widehat{\gamma}_\mu, \widehat{\gamma}_\nu\} = 2\delta_{\mu\nu}. \tag{6.10}$$

The continuum vector current is

$$V_\mu(x) = \overline{q}(x)\widehat{\gamma}_\mu h(x). \tag{6.11}$$

Morningstar and Shigemitsu calculate the heavy-light continuum QCD current analytically, for the temporal component of the axial vector current in Reference [112] and for both vector and axial vector currents in [113]. They

use massless light quarks, onshell mass and wavefunction renormalisation in Feynman gauge and expand the current in powers of the inverse heavy quark mass. For an incoming heavy quark of momentum, p, and an outgoing light quark of momentum p', the one-loop current is

$$\langle q(p')|J_\mu|h(p)\rangle_{\text{QCD}} = \overline{u}_q(p')W_\mu^J(p',p)u_h(p), \tag{6.12}$$

where J_μ indicates either the axial-vector or vector current and

$$W_\mu^J(p',p) = a_1\Gamma_\mu^J - a_2\frac{ip_\mu}{M}\Gamma_0^J\gamma_0 - a_3\frac{p\cdot p'}{M^2}\Gamma_\mu^J - a_4\frac{ip'_\mu}{M}\Gamma_0^J\gamma_0$$
$$+ a_5\frac{p\cdot p'}{M^2}\frac{ip_\mu}{M}\Gamma_0^J\gamma_0 + \mathcal{O}(1/M^2). \tag{6.13}$$

Here the operator Γ^J stands for either the vector current operator $\Gamma_\mu^V = \widehat{\gamma}_\mu$ or the axial vector current $\Gamma_\mu^A = \widehat{\gamma}_5\widehat{\gamma}_\mu$. The spinors, u_h and u_q, are the standard Dirac heavy quark and light quark spinors respectively. The expansion coefficients are given by

$$a_1 = 1 - \frac{\alpha_s}{\pi}\left(\ln\frac{\lambda}{M} + \frac{11}{12}\right),$$
$$a_2 = \frac{2\alpha_s}{3\pi},$$
$$a_3 = \frac{\alpha_s}{\pi}\left(\frac{1}{6} - \frac{8\pi}{9}\frac{M}{\lambda} - 2\ln\frac{\lambda}{M}\right)$$
$$a_4 = \frac{\alpha_s}{3\pi}\left(\frac{1}{2} + 2\ln\frac{\lambda}{M}\right),$$
$$a_5 = \frac{\alpha_s}{3\pi}\left(5 + 4\ln\frac{\lambda}{M}\right). \tag{6.14}$$

Here λ is the gluon mass. Ultraviolet divergences are regulated using dimensional regularisation.

In the Appendix to Reference [47], Müller quotes a slightly different infrared finite contribution to the coefficient a_3:

$$a_3^{\text{EM}} = -\frac{\alpha_s}{\pi}\left(-\frac{29}{18} - \frac{8\pi}{9}\frac{M}{\lambda} - 2\ln\frac{\lambda}{M}\right). \tag{6.15}$$
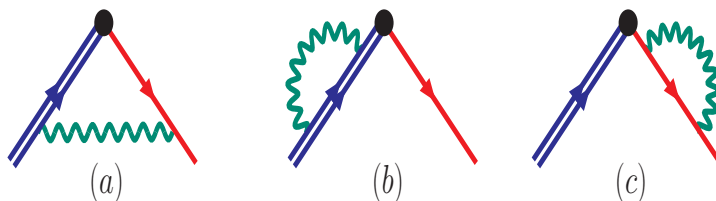
Figure 6.2: Contributions to the continuum QCD axial vector and vector heavy-light currents. The diagram on the left, diagram (a), represents the vertex correction and the other diagrams, from left to right, are (b) the heavy quark and (c) the light quark wavefunction renormalisation contributions respectively. Double blue lines represent heavy quarks, single red lines indicate light quarks, wiggly green lines are gluons and the black dots represent the current insertion.

This discrepancy does not affect the results that I present in this dissertation, but will need to be clarified in future work that requires a_3.

Three diagrams contribute to the continuum QCD currents at one-loop, which I illustrate in Figure 6.2. The diagram on the left represents the one-loop vertex correction and the other two contributions are the one-loop wavefunction renormalisation diagrams. Before reviewing the lattice current calculation, I study the light quark renormalisation parameters. I require the wavefunction renormalisation for massless relativistic quarks for the matching calculation laid out in this dissertation. Ultimately the mass renormalisation for HISQ quarks will also be required for the extension of this work to massive light quarks. As the derivation of the renormalisation parameters for relativistic quarks is different to that for NRQCD, which I present in Chapter 5, I collect the necessary ingredients for both massive and massless relativistic quarks here. I start by deriving an expression for the wavefunction renormalisation.

6.3 Relativistic quark renormalisation parameters

I extract the relativistic quark wavefunction renormalisation by taking appropriate derivatives of the one-loop quark selfenergy. For massive relativistic

quarks in Euclidean space, the tree-level propagator is

$$G_0^{-1}(p) = i\not{p} + m_0,$$

(6.16)

where m_0 is the bare quark mass. I write the one-loop propagator in terms of the one-loop selfenergy, Σ, as

$$G_1^{-1}(p) = i\not{p} + m_0 - \alpha_s \Sigma.$$

(6.17)

I now write the selfenergy as

$$\Sigma = i\not{p}\Sigma_1 + m_0 \Sigma_0,$$

(6.18)

so that the propagator becomes

$$G_1^{-1}(p) = (1 - \alpha_s \Sigma_1) i\not{p} + (1 - \alpha_s \Sigma_0) m_0.$$

(6.19)

I multiply the numerator and denominator in the propagator by

$$(1 - \alpha_s \Sigma_0) m_0 - (1 - \alpha_s \Sigma_1) i\not{p}$$

(6.20)

and then divide by $(1 + \alpha_s \Sigma_1)$ to obtain

$$G(p) = \frac{-i\not{p} + (1 - \alpha_s(\Sigma_0 + \Sigma_1)) m_0}{(1 - \alpha_s \Sigma_1) p^2 + (1 - \alpha_s(2\Sigma_0 - \Sigma_1)) m_0^2}.$$

(6.21)

The mass renormalisation is given by

$$m = \left(\frac{1 - \alpha_s \Sigma_0}{1 - \alpha_s \Sigma_1}\right) m_0 \Bigg|_{p_0 = im_0} = (1 - \alpha_s(\Sigma_0 - \Sigma_1)) m_0 = Z_m m_0,$$

(6.22)

that is,

$$Z_m = 1 - \alpha_s(\Sigma_0 - \Sigma_1).$$

(6.23)

We define the wavefunction renormalisation through the residue of the pole at $p_0 = im_0$. Denoting the denominator of $G(p)$ by $\Gamma(p)$, the wavefunction

renormalisation is given by

$$Z_\psi^{-1} = \frac{\mathrm{d}\Gamma}{\mathrm{d}p^2}\bigg|_{p_0=im_0} = \left[1 + \alpha_s\Sigma_1 - 2m_0^2\alpha_s\frac{\mathrm{d}}{\mathrm{d}p^2}\left(\Sigma_0 - \Sigma_1\right)\right]_{p_0=im_0}. \tag{6.24}$$

I now apply the chain rule to take derivatives with respect to p_0, and write the wavefunction renormalisation as

$$Z_\psi^{-1} = 1 + \alpha_s\left[\Sigma_1 + im_0^2\frac{\mathrm{d}}{\mathrm{d}p_0}\left(\Sigma_1 - \Sigma_0\right)\right]_{p_0=im_0}. \tag{6.25}$$

For massless relativistic quarks, the corresponding expression is just

$$Z_\psi^{-1} = 1 + \alpha_s\Sigma_1|_{p_0=0}. \tag{6.26}$$

I calculate the massless relativistic wavefunction renormalisation numerically, using both unimproved staggered quarks and ASQTad quarks. For massive HISQ quarks, the derivation and calculation is more involved. I briefly discuss the derivation of the HISQ renormalisation parameters before outlining the calculation of the lattice current operators. My presentation for the HISQ parameters is based on [114] and I provide a more detailed derivation in Appendix E

6.4   HISQ renormalisation parameters

I write the inverse relativistic quark propagator as

$$G(p)^{-1} = G_0^{-1}(p) - \Sigma(p) \tag{6.27}$$

where

$$G_0^{-1}(p) = \sum_\mu i\sin\left(p_\mu\right)K_\mu(p)\gamma_\mu + m_0, \tag{6.28}$$

and

$$K_\mu(p) = 1 + \frac{1+\epsilon}{6}\sin^2\left(p_\mu\right). \tag{6.29}$$

Here I parameterise the selfenergy as

$$\Sigma(p) = \sum_\mu i \sin\left(p_\mu\right) B_\mu(p)\gamma_\mu + C(p), \tag{6.30}$$

to be consistent with the notation of [114]. We can see, by comparing this parameterisation with Equation (6.18), that B_μ corresponds to Σ_1 in Equation (6.18) and $C(p)$ to Σ_0.

To calculate the pole mass, I set $\mathbf{p} = 0$ and $p_0 = iE$, where E is the rest energy. Then the pole condition,

$$\sum_\mu \sin^2\left(p_\mu\right)\left(K_\mu - B_\mu\right)^2 + (m_0 - C)^2 = 0 \tag{6.31}$$

becomes

$$-\sinh^2 E \left(1 - \frac{1+\epsilon}{6}\sinh^2 E - B_0\right)^2 + (m_0 - C)^2 = 0. \tag{6.32}$$

Taking the positive energy solution, and expanding the rest energy E and the parameter ϵ in the strong coupling constant, the tree-level mass, m_{tree}, at fixed bare mass m_0, is given by

$$\sinh m_{\text{tree}} \left(1 - \frac{1+\epsilon_{\text{tree}}}{6}\sinh^2 m_{\text{tree}}\right) = m_0. \tag{6.33}$$

The parameter ϵ_{tree} is fixed by requiring the mass to be equal to the kinetic mass, defined as

$$m_{\text{kin}}^{-1} = \left.\frac{\partial^2 E}{\partial p_z^2}\right|_{p_z=0}, \tag{6.34}$$

for an onshell particle with momentum $p_\mu = (iE, 0, 0, p_z)$. The resulting solution is [114]

$$\epsilon_{\text{tree}} = \left(4 - \sqrt{4 + \frac{12m_{\text{tree}}}{\cosh m_{\text{tree}}\sinh m_{\text{tree}}}}\right) / \sinh^2 m_{\text{tree}} - 1. \tag{6.35}$$

We obtain the solution for m_{tree} by plugging in this expression for ϵ_{tree} into Equation (6.33) and solving iteratively.

124

The one-loop mass is given by

$$\alpha_s \frac{1}{Z_2^{(0)}} m_1 - \alpha_s \epsilon_1 \frac{\sinh^3 m_{\text{tree}}}{6} - B_0 \sinh m_{\text{tree}} = -C, \tag{6.36}$$

where $Z_2^{(0)}$ is the tree-level wavefunction renormalisation:

$$\frac{1}{Z_2^{(0)}} = \left(1 - \frac{1 + \epsilon_{\text{tree}}}{2} \sinh^2 m_{\text{tree}} \right) \cosh m_{\text{tree}}. \tag{6.37}$$

At non-zero spatial momentum, we define the kinetic mass, m_{kin}, by Equation (6.34). The tree-level pole condition is

$$-\left(\sinh E - \frac{1 + \epsilon_{\text{tree}}}{6} \sinh^3 E \right)^2 + \left(\sin p_z + \frac{1 + \epsilon_{\text{tree}}}{6} \sin^3 p_z \right)^2 + m_0^2 = 0. \tag{6.38}$$

and the tree-level kinetic mass is

$$m_{\text{kin}} = \left(\sinh m_{\text{tree}} - \frac{1 + \epsilon_{\text{tree}}}{6} \sinh^3 m_{\text{tree}} \right)$$
$$\times \left(1 - \frac{1 + \epsilon_{\text{tree}}}{2} \sinh^2 m_{\text{tree}} \right) \cosh m_{\text{tree}}. \tag{6.39}$$

Setting $m_{\text{kin}} = m_{\text{tree}}$ gives us the expression for ϵ_{tree} in Equation (6.35).

We define the wavefunction renormalisation through the residue of the quark propagator at the single particle pole:

$$\int_{-\pi}^{\pi} \frac{\mathrm{d}p_0}{2\pi} e^{ip_0 t} G(p_0, \mathbf{0}) = Z_2 e^{-mt} \frac{1 + \gamma_0}{2} + \ldots, \tag{6.40}$$

where the ellipses stand for poles corresponding to more complicated bound state and multi-particle states. The final expression for the wavefunction renormalisation is

$$Z_2^{-1} = \left(1 - \frac{1 + \epsilon}{2} \sinh^2 m \right) \cosh m + i \frac{\mathrm{d}}{\mathrm{d}p_0} \left(iB \sin p_0 + C \right). \tag{6.41}$$

At tree-level, this expression reduces to the tree-level wavefunction renormalisation, $Z_2^{(0)}$, given in Equation (6.37). The one-loop wavefunction renor-

malisation, $Z_2^{(1)}$, is

$$\frac{1}{Z_2^{(1)}} = \frac{1}{Z_2^{(0)}} \left\{ 1 - \alpha_s \epsilon_1 \frac{Z_2^{(0)}}{2} \cosh m_{\text{tree}} \sinh^2 m_{\text{tree}} + i \frac{\mathrm{d}}{\mathrm{d}p_0} \left(iB \sin p_0 + C \right) Z_2^{(0)} \right.$$
$$\left. + \alpha_s m_1 \sinh m_{\text{tree}} \left[1 - \frac{1 + \epsilon_{\text{tree}}}{2} \left(2 \cosh^2 m_{\text{tree}} + \sinh^2 m_{\text{tree}} \right) \right] Z_2^{(0)} \right\}. \tag{6.42}$$

For massless HISQ with zero spatial momentum, we immediately see that the one-loop wavefunction renormalisation becomes

$$Z_\psi = 1 + \alpha_s B_0, \tag{6.43}$$

since $m_{\text{tree}} = m_0 = 0$, $\epsilon_{\text{tree}} = 0$ and $Z_2^{(0)} = 1$. As we would expect, this is just Equation (6.26) rewritten in the notation of [114], that is, with $B_0 = \Sigma_1$.

6.5 The lattice current

I now derive the lattice operators corresponding to the continuum operators in Equation (6.13), largely following the derivation in [112]. I illustrate the extra lattice contributions in Figure 6.3. As I discuss in Section 2.4, the lattice NRQCD heavy quark field is defined in terms of a two-component Pauli spinor, which I here denote $\Psi(x)$. We obtain this spinor from the Dirac heavy quark field, $h(x)$, using the FWT transformation, which decouples the quark and antiquark fields.

We transform the external spinor $u_h(p)$ into a nonrelativistic Pauli spinor, $u_Q(p)$,

$$u_h(p) = \left(1 - \frac{1}{2M} \widehat{\gamma} \cdot \mathbf{p} \right) u_Q(p) + \mathcal{O}(1/M^2). \tag{6.44}$$

Then we can decompose the continuum current in Equation (6.12) as

$$\langle q(p')|J_\mu|h(p)\rangle_{\text{NRQCD}} = \overline{u}_q(p')\Omega_\mu^J(p', p)u_Q(p), \tag{6.45}$$
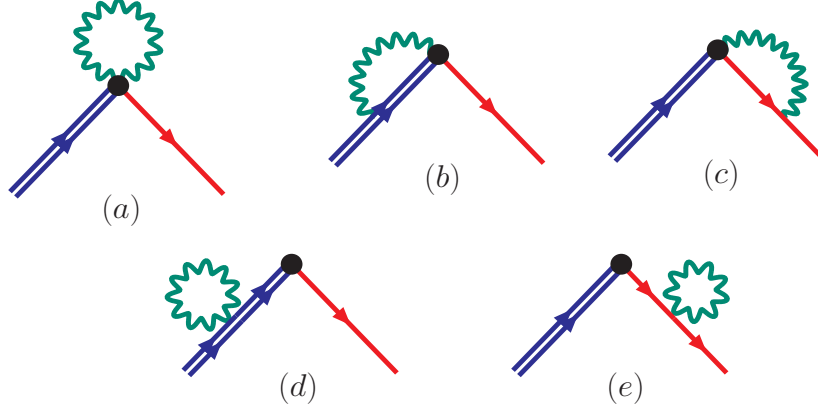
Figure 6.3: Additional lattice NRQCD contributions to the axial vector and vector heavy-light currents. The three upper diagrams, (a), (b) and (c), represent the vertex corrections at next-to-leading order in the inverse heavy quark mass. The lower diagrams, from left to right, are the tadpole diagrams for (d) the heavy quark and (e) the light quark wavefunction renormalisation contributions respectively. Double blue lines represent heavy quarks, single red lines indicate light quarks, wiggly green lines are gluons and the black dots represent the current insertion.

where in this case, the temporal component of Ω_μ^J is given by

$$\Omega_0^J(p',p) = \eta_0^t \Gamma_0^J - i\eta_1^t \Gamma_0^J \frac{\widehat{\gamma}\cdot\mathbf{p}}{2M} + i\eta_2^t \frac{\widehat{\gamma}\cdot\mathbf{p}'}{2M}\gamma_0\Gamma_0^J + \mathcal{O}(\alpha_s^2, 1/M^2), \qquad (6.46)$$

and the spatial components are

$$\Omega_k^J(p',p) = \eta_0^s \Gamma_k^J - i\eta_1^s \Gamma_k^J \frac{\widehat{\gamma}\cdot\mathbf{p}}{2M} + i\eta_2^s \frac{\widehat{\gamma}\cdot\mathbf{p}'}{2M}\gamma_0\Gamma_k^J - i\eta_3^s \frac{p_k}{2M}\Gamma_0^J$$
$$- \eta_4^s \frac{ip_k'}{2M}\Gamma_0^J + \mathcal{O}(\alpha_s^2, 1/M^2). \qquad (6.47)$$

Here the temporal coefficients are

$$\begin{aligned}
\eta_0^t &= a_1 + a_2 = 1 + \alpha_s B_0^t, \\
\eta_1^t &= a_1 - a_2 = 1 + \alpha_s B_1^t, \\
\eta_2^t &= 2(a_3 + a_4 + a_5) = \alpha_s B_2^t,
\end{aligned} \qquad (6.48)$$

with

$$B_0^t = -\frac{1}{\pi}\left(\ln\frac{\lambda}{M} + \frac{1}{4}\right),$$

$$B_1^t = -\frac{1}{\pi}\left(\ln\frac{\lambda}{M} + \frac{19}{12}\right),$$

$$B_2^t = \frac{1}{3\pi}\left(12 + \frac{16\pi}{3}\frac{M}{\lambda}\right). \tag{6.49}$$

The spatial coefficients are given by

$$\eta_0^s = a_1 = 1 + \alpha_s B_0^s,$$

$$\eta_1^s = \eta_0,$$

$$\eta_2^s = 2a_3 = \alpha_s B_2^s,$$

$$\eta_3^s = 2a_2 = \alpha_s B_3^s,$$

$$\eta_4^s = 2a_4 = \alpha_s B_4^s, \tag{6.50}$$

where

$$B_0^s = \frac{1}{\pi}\left(\ln\frac{\lambda}{M} - \frac{11}{12}\right),$$

$$B_2^s = \frac{1}{\pi}\left(1 - \frac{16\pi}{3}\frac{M}{\lambda} - 12\ln\frac{\lambda}{M}\right),$$

$$B_3^s = \frac{4}{3\pi}$$

$$B_4^s = \frac{1}{3\pi}\left(1 + 4\ln\frac{\lambda}{M}\right). \tag{6.51}$$

The lattice NRQCD currents corresponding to the nonrelativistic contin-

uum operators in Equations (6.46) and (6.47) are

$$
\begin{aligned}
J^{(0)}_{\mu,\mathrm{lat}}(x) &= \overline{q}(x)\Gamma^J_\mu Q(x), \\
J^{(1)}_{\mu,\mathrm{lat}}(x) &= -\frac{1}{2aM}\overline{q}(x)\Gamma^J_\mu \widetilde{\gamma}\cdot \nabla Q(x), \\
J^{(2)}_{\mu,\mathrm{lat}}(x) &= -\frac{1}{2aM}\overline{q}(x)\widetilde{\gamma}\cdot \overleftarrow{\nabla}\gamma_0\Gamma^J_\mu Q(x), \\
J^{(3)}_{k,\mathrm{lat}}(x) &= -\frac{1}{2aM}\overline{q}(x)\Gamma^J_0 \nabla_k Q(x), \\
J^{(4)}_{k,\mathrm{lat}}(x) &= -\frac{1}{2aM}\overline{q}(x)\overleftarrow{\nabla}_k \Gamma^J_0 Q(x).
\end{aligned}
\tag{6.52}
$$

Here $q(x)$ is the light quark field in the lattice theory, M is the bare heavy quark mass and $Q(x)$ is given in terms of the NRQCD heavy quark field, $\Psi(x)$, by

$$
Q(x) = \begin{pmatrix} \Psi(x) \\ 0 \end{pmatrix}.
\tag{6.53}
$$

In this dissertation I am concerned only with the leading order contribution to the heavy-light current in the inverse heavy quark mass expansion. This term is the $J^{(0)}_{\mu,\mathrm{lat}}$ current. However, as I discuss in the next section, renormalisation of the lattice operators causing mixing-down from the current $J^{(1)}_{\mu,\mathrm{lat}}$. Therefore, at zero external momentum, there are two vertex correction diagrams that I must calculate for the leading order current. The first diagram is diagram (a) in Figure 6.2 with the $J^{(0)}_{\mu,\mathrm{lat}}$ current insertion. The second is the same diagram, (a) in Figure 6.2, but including the $J^{(1)}_{\mu,\mathrm{lat}}$ current insertion. In the language of [89], these contributions are ζ_{00} and ζ_{10}. I now discuss these contributions more fully.

6.5.1 The lattice operator mixing matrix

The lattice operators in Equation (6.52) mix under renormalisation and the elements of the mixing matrix can be calculated using lattice perturbation theory. I write the mixing matrix, Z^J_{ij}, as

$$
\langle q(p')|J^{(i)}_{\mu,\mathrm{lat}}|h(p)\rangle_{\mathrm{lat}} = \sum_j Z^J_{ij}\overline{u}_q(p')\Omega^{(j),J}_\mu(p',p)u_Q(p).
\tag{6.54}
$$

I further decompose the mixing matrix at one-loop as

$$Z_{ij} = \delta_{ij} + \alpha_s \left(\frac{1}{2} \left(Z_q + Z_Q \right) \delta_{ij} + \delta_{i1}\delta_{j1} + \zeta_{ij} \right). \tag{6.55}$$

In this expression, Z_q is the light quark wavefunction renormalisation, Z_Q the heavy quark wavefunction renormalisation, Z_M the heavy quark mass renormalisation and ζ_{ij} the vertex corrections. We can separate out the infrared divergences and express the renormalisation constants in terms of the known logarithmic divergences, Z_i^{div}, the infrared finite piece, $\widetilde{Z}_i$, and, where appropriate, tadpole improvement corrections, $Z_i^{u_0}$. here the tildes indicate infrared finite contributions. Thus we write

$$
\begin{aligned}
Z_q &= \widetilde{Z}_q + Z_q^{\text{div}} + Z_q^{u_0} \\
Z_Q &= \widetilde{Z}_Q + Z_Q^{\text{div}} \\
Z_M &= \widetilde{Z}_M + Z_M^{u_0} \\
\zeta_{ij} &= \widetilde{\zeta}_{ij} + \zeta_{ij}^{\text{div}} + \zeta_{ij}^{u_0}.
\end{aligned}
\tag{6.56}
$$

The divergent contributions to the wavefunction renormalisation are

$$Z_q^{\text{div}} = \frac{\alpha_s}{3\pi} \ln a^2\lambda^2, \tag{6.57}$$

and

$$Z_Q^{\text{div}} = \frac{2\alpha_s}{3\pi} \left(\ln aM - \ln \frac{a^2\lambda^2}{a^2M^2} \right). \tag{6.58}$$

The mass renormalisation arises because I have expressed the continuum pole mass M in terms of the bare lattice mass, M_0:

$$M = (1 + Z_M)M_0 + \mathcal{O}(\alpha_s^2). \tag{6.59}$$

The pole mass must appear in the continuum currents, but the lattice currents are defined in terms of the bare lattice mass. I present results for the heavy quark mass renormalisation in NRQCD in Section 5.1.4 and do not repeat that part of my analysis here.

We are interested in constructing the continuum operators from their

lattice counterparts, so we invert this relation and remove the dependence on the external states, giving

$$\Omega_\mu^{(j),J}(p',p) = \sum_j \left(Z_{ji}^J\right)^{-1} J_{\mu,\text{lat}}^{(i)}. \tag{6.60}$$

In the rest of this chapter I focus on the temporal component of the axial-vector current. For this case, the mixing relation becomes

$$\begin{aligned}
A_0 = (1 + \alpha_s\widetilde{\rho}_0)J_{0,\text{lat}}^{(0)} &+ (1 + \alpha_s\rho_1)J_{0,\text{lat}}^{(1),\text{sub}} \\
&+ \alpha_s\rho_2 J_{0,\text{lat}}^{(2),\text{sub}} + \mathcal{O}(\alpha_s^2, 1/M^2, a^2\alpha_s).
\end{aligned} \tag{6.61}$$

Here I have introduced the improved, more physical currents, $J_{0,\text{lat}}^{(i),\text{sub}}$, which are defined by

$$J_{0,\text{lat}}^{(i),\text{sub}} = J_{0,\text{lat}}^{(i)} - \alpha_s\zeta_{10}J_{0,\text{lat}}^{(0)}. \tag{6.62}$$

The coefficients, $\widetilde{\rho}_0$, ρ_1 and ρ_2 are given by

$$\begin{aligned}
\widetilde{\rho}_0 &= \widetilde{B}_0 - \frac{1}{2}(\widetilde{Z}_q + \widetilde{Z}_Q) - \widetilde{\zeta}_{00}, \\
\rho_1 &= \widetilde{B}_1 - \frac{1}{2}(\widetilde{Z}_q + \widetilde{Z}_Q) - \widetilde{Z}_M - \widetilde{\zeta}_{01} - \widetilde{\zeta}_{11}, \\
\rho_2 &= \widetilde{B}_2 - \widetilde{\zeta}_{02} - \widetilde{\zeta}_{22},
\end{aligned} \tag{6.63}$$

with

$$\begin{aligned}
\widetilde{B}_0 &= \frac{1}{\pi}\left(\ln(aM_0) - \frac{1}{4}\right), \\
\widetilde{B}_1 &= \frac{1}{\pi}\left(\ln(aM_0) - \frac{19}{12}\right), \\
\widetilde{B}_2 &= \frac{4}{\pi}.
\end{aligned} \tag{6.64}$$

These improved matrix elements have the $\mathcal{O}(\alpha_s/(aM_0))$ power law contributions subtracted out [107]. We can understand the origin of these power-law divergences as follows. The nonleading currents, $J_{\text{lat}}^{(i\neq 0)}$, mix with the other NRQCD currents, renormalising the leading order current $J_{\text{lat}}^{(0)}$. We

can determine the form of the constant of proportionality using dimensional arguments: we must have

$$J_{\text{lat}}^{(1)} = \frac{C_{10}}{aM} J_{\text{lat}}^{(0)} + \mathcal{O}\left(\frac{1}{M}\right) + \ldots \tag{6.65}$$

The leading term on the right hand side of Equation (6.65) is the power law contribution to the matrix element. Our matching calculation should remove these artifacts of the effective theory. We match perturbatively, so we can only remove power law contributions at a given order in the coupling constant. If we write Equation (6.61) in terms of the uncorrected currents, we have

$$A_0 = (1 + \alpha_s \rho_0) J_{0,\text{lat}}^{(0)} + (1 + \alpha_s \rho_1) J_{0,\text{lat}}^{(1)} + \alpha_s \rho_2 J_{0,\text{lat}}^{(2)}, \tag{6.66}$$

where

$$\rho_0 = B_0 - \frac{1}{2}(Z_q + Z_Q) - \zeta_{00} - \zeta_{10}. \tag{6.67}$$

Concentrating for the moment on the mixing of $J_{0,\text{lat}}^{(1)}$ with $J_{0,\text{lat}}^{(0)}$, the relevant terms are

$$(1 + \alpha_s \rho_0) J_{0,\text{lat}}^{(0)} + J_{0,\text{lat}}^{(1)}. \tag{6.68}$$

We can rewrite the $J_{0,\text{lat}}^{(1)}$ current using Equation (6.65) to obtain

$$(1 + \alpha_s \widetilde{\rho}_0) J_{0,\text{lat}}^{(0)} + \left[\frac{C_{10}}{aM} - \alpha_s \zeta_{10}\right] J_{0,\text{lat}}^{(0)} + \frac{1}{aM} + \ldots \tag{6.69}$$

The mixing coefficient ζ_{10} represents the projection of $J_{0,\text{lat}}^{(1)}$ onto $J_{0,\text{lat}}^{(0)}$ at one-loop, which is precisely the one-loop contribution to C_{10}/aM in Equation (6.65). We have thus reduced the power law term, $[C_{10}/aM - \alpha_s \zeta_{10}] J_{0,\text{lat}}^{(0)}$, from an $\mathcal{O}(\alpha_s/aM)$ contribution to $\mathcal{O}(\alpha_s^2/aM)$. For we convenience, we therefore work with the subtracted current $J_{0,\text{lat}}^{(1),\text{sub}}$, which is equal to the last two terms in Equation (6.69) up to higher order corrections.

In this work I calculate the leading order contribution in the inverse heavy

quark mass expansion. This is just

$$A_0 = (1 + \alpha_s \rho_0) J_{0,\text{lat}}^{(0)} + \mathcal{O}(\alpha_s^2, 1/aM, a^2\alpha_s). \tag{6.70}$$

I now present all my results necessary to extract the matching coefficient ρ_0. I start with the relativistic wavefunction renormalisation.

6.6 Numerical results

I computed all contributions to the matching calculation using the HiPPy and HPsrc routines. I introduce these routines in Section 3.3.1. I wrote each contribution as a TaylUR valued FORTRAN function in an HPsrc module. This allowed me to easily extract different derivatives of the selfenergy and to specify massless or massive quarks with a single flag.

6.6.1 Relativistic wavefunction renormalisation

Infrared behaviour   I extract the logarithmic infrared behaviour of the massless wavefunction renormalisation by evaluating the wavefunction renormalisation at different gluon masses and fitting to a function logarithmic in the gluon mass.

I present my results for the divergent contribution to the wavefunction renormalisation in Table 6.1. I quote the known analytic result, given in Equation (6.57), in the first column of Table 6.1 as comparison. My results are in excellent agreement with expected analytic behaviour.

I use Symanzik-improved gluons with three different relativistic staggered quark actions, unimproved, ASQTad and HISQ. I show results obtained with 12 different gluon masses, with values between $a^2\lambda^2 = 1 \times 10^{-3}$ and $a^2\lambda^2 = 10^{-8}$. I used exactly massless light quarks for the massless wavefunction renormalisation.

In Figure 6.4 I plot the massless wavefunction renormalisation for unimproved staggered quarks, ASQTad quarks and HISQ quarks. I include the fits to logarithmic functions of the gluon mass for each action. The data in-

Analytic	Unimproved	ASQTad	HISQ
0.106103	0.10611(11)	0.10587(30)	0.106095(8)

Table 6.1: Numerical results for the infrared divergent contributions to the massless light quark wavefunction renormalisations, $Z_q^{(\mathrm{IR})}$, for three different actions. I compare my results to the coefficient of the known analytic divergence in column two, given to six significant places.

dicate that the fit is excellent and that my `HPSRC` routines are correctly able to handle the logarithmic behaviour of the wavefunction renormalisation.

Finite contributions   I use two independent methods to extract the finite contributions to the massless wavefunction renormalisation. For the first method, I calculate the finite contribution by computing the wavefunction renormalisation at different gluon masses and fitting to a function logarithmic in the gluon mass. For the second method, I remove the logarithmic behaviour using an infrared subtraction function, given by

$$Z_q^{\mathrm{sub}} = -\frac{32\pi}{3} \int \frac{\mathrm{d}^4 k}{(2\pi)^4} \frac{\mathbf{k}^2 - k_0^2}{k^2(k^2 + \lambda^2)^2}. \tag{6.71}$$

I evaluate the subtraction function numerically and extract the logarithmic behaviour by fitting to a function of the gluon mass. The subtraction function is very quick to evaluate: I use 10^8 function evaluations and 20 `VEGAS` iterations for each gluon mass, which took only five minutes on six processors. In Table 6.2 I show my results for the finite contribution to the infrared subtraction function for unimproved staggered, ASQTad and HISQ quarks. In Figure 6.5 I plot my results for the wavefunction renormalisation with infrared behaviour subtracted out. This plot clearly shows the infrared divergences are cleanly handled by the subtraction function.

In Table 6.3 I compare my results for the finite part of the rainbow diagram contribution to the massless and massive wavefunction renormalisations using the two different methods described above. I constrained the coefficient of the logarithmic divergence to its known analytic value. The data in Table
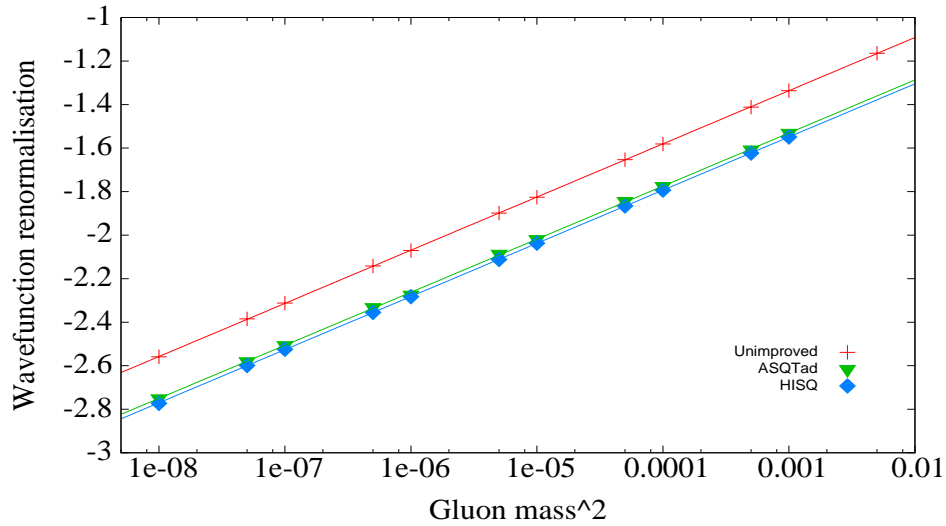
Figure 6.4: Plot of the infrared behaviour of the massless wavefunction renormalisation for three light quark actions. I plot results for unimproved staggered quarks with red crosses, for ASQTad quarks with green triangles and for HISQ quarks with blue diamonds. Errorbars are smaller than the data points. I show the corresponding fits to logarithmic functions in the gluon mass as solid lines. I include only contributions from the infrared divergent rainbow diagram, not the infrared finite contributions from the tadpole diagram.
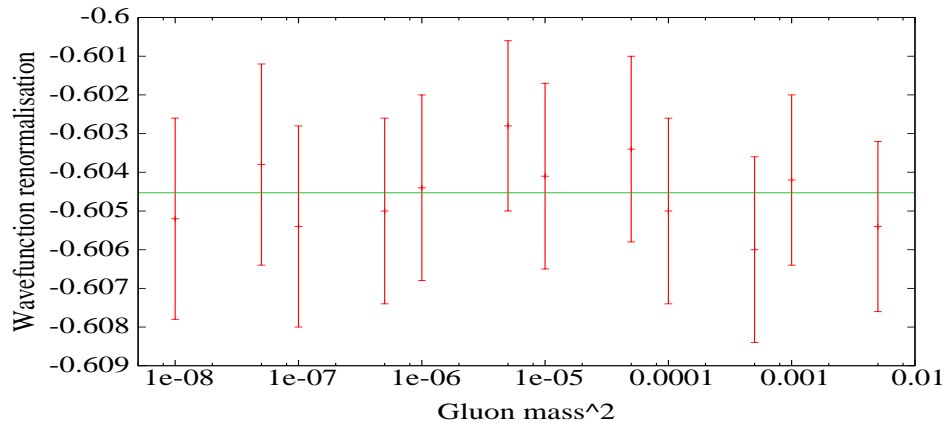
Figure 6.5: Plot of the massless ASQTad wavefunction renormalisation with infrared divergence subtracted. I plot a fit to a constant function. Note the very small scale on the vertical axis.

Z_q^{sub}	$Z_q^{\text{sub,div}}$
-0.191617(5)	0.106099(3)

Table 6.2: Numerical results for the light quark wavefunction renormalisation subtraction function, Z_q. I show both the coefficients of the logarithmic divergence, $Z_q^{\text{sub,div}}$, and the finite contribution, Z_q^{sub}.

6.3 show that, whilst both methods handle the infrared structure well, the subtraction function method is most effective for the unimproved staggered quark action. However, this may simply reflect the need for greater statistics with ASQTad and HISQ quark calculations. Comparison with results in the literature, which I review in the next section, suggests that I can more reliably extract the infrared finite contributions using the constrained fit method.

Coefficient	Unimproved	ASQTad	HISQ
Z_q^{rbow} via subtraction	-0.60394(75)	0.79615(29)	-0.8169(48)
Z_q^{rbow} via fit	-0.60316(20)	-0.79726(61)	-0.81598(24)

Table 6.3: Numerical results for the finite rainbow diagram contributions to the light quark wavefunction renormalisation, Z_q. I show unimproved staggered quarks in column two, ASQTad quarks in column three and HISQ quarks in column four.

I show my results for all infrared finite contributions to the wavefunction renormalisation in Table 6.4. I use three different sets of actions: unimproved staggered quarks with unimproved Wilson gluons; ASQTad light quarks with Symanzik-improved gluons; and HISQ light quarks with Symanzik-improved gluons.

The individual contributions are the infrared finite contribution from the rainbow diagram, Z_q^{rbow}; the tadpole contribution, Z_q^{tad}; and the tadpole correction factor, $Z_q^{u_0}$. I also show the total infrared finite result, $\widetilde{Z}_q$, in Table 6.4.

The tadpole correction for the ASQTad wavefunction renormalisation is

Action	ξ	Z_q^{rbow}	Z_q^{tad}	$Z_q^{u_0}$	$\widetilde{Z}_q$
Unimproved	1	-0.6032(2)	1.296(1)	–	0.693(1)
	0	0.0001(3)	0.973(1)	–	0.973(1)
ASQTad	1	-0.7973(6)	1.600(1)	-1.72593(5)	-0.923(1)
	0	0.0001(5)	1.309(1)	-1.72593(5)	-0.417(1)
HISQ	1	-0.8160(2)	0.424(1)	–	-0.392(1)
	0	0.0001(3)	0.134(1)	–	0.134(1)

Table 6.4: Numerical results for all three finite contributions to the light quark wavefunction renormalisation, $\widetilde{Z}_q$, for three different actions. I use Feynman gauge, with $\xi = 1$, and Landau gauge, with $\xi = 0$.

given in [89] as

$$Z_q^{u_0} = -\left(4 - \frac{1}{4} - \frac{3}{2}\right) u_0^{(2)} = -\frac{9}{4} u_0^{(2)}, \qquad (6.72)$$

where, in this case, I use the value of $u_0^{(2)}$ for Landau tadpoles from Equation (4.5). I do not include tadpole corrections for the unimproved light quark action. The tadpole correction is not required for HISQ quarks, because the high energy modes that contribute to tadpole diagrams are reduced by construction as part of the improvement procedure that reduces taste-changing interactions.

I show results for both Feynman gauge, with gauge parameter $\xi = 1$, and Landau gauge, with $\xi = 0$. For the rainbow diagram in Feynman gauge I use 12 different gluon masses and fit to logarithmic function of the gluon mass. In Landau gauge, the rainbow contribution is infrared finite.

6.6.2 Comparison to the literature

Gulez *et al.* calculate the massless ASQTad wavefunction renormalisation in [89]. We can see, by comparing my ASQTad results for the wavefunction renormalisation in Table 6.4, with their values in Table 6.5, that I am able to reproduce their results correctly. This agreement provides good confidence in

both my `HPSRC` routines and my fits for the logarithmic infrared behaviour. As I discuss in the previous section, this agreement also justifies my choice of

ξ	Z_q^{rbow}	Z_q^{tad}	$Z_q^{u_0}$	$\widetilde{Z}_q$
1	-0.798(3)	1.600	-1.726	-0.924(3)
0	0.000(3)	1.310	-1.726	-0.416(3)

Table 6.5: Numerical results for the finite contributions to the massless ASQ-Tad wavefunction renormalisation, $\widetilde{Z}_q$. I take all results from [89]. The authors of [89] use different notation, with C_q representing the wavefunction renormalisation and C_q^{reg} specifying the infrared finite contribution from the rainbow diagram, that is, Z_q^{rbow} in my notation.

fitting to the gluon mass to handle the infrared structure, because my results obtained using the subtraction function method do not reproduce the data in Table 6.5 so reliably.

In [47], Müller calculates the massless HISQ wavefunction renormalisation. I show his results in Table 6.6. We can see, by comparing my results in

Z_q^{rbow}	Z_q^{tad}	$\widetilde{Z}_q$
-0.8155(12)	0.4250(10)	-0.3905(16)

Table 6.6: Numerical results for the finite contributions to the massless HISQ wavefunction renormalisation from [47].

Table 6.4 with those in Table 6.6, that my results are in excellent agreement with those of [47]. This establishes that my wavefunction renormalisation routines work correctly and handle the infrared structure appropriately.

6.6.3   HISQ renormalisation parameters

I give the HISQ renormalisation parameters for three different masses in Table 6.7 and 6.8. I calculate the massive HISQ renormalisation parameters

using exact modesummation on L^4 lattices, where L is the spatial extent. I implement twisted boundary conditions, with two-dimensional twists, to regulate the infrared behaviour. I discuss twisted boundary conditions in more detail in Section 3.3.2. I extrapolate the results to infinite lattice volume using a polynomial fit to the inverse lattice side length.

In Figure 6.6 I present example results for the infinite volume extrapolation. I show result for both the mass renormalisation and the wavefunction renormalisation in Feynman gauge and use light quark mass $am_q = 0.1$.

am_q	L	Z_m		Z_ψ	
		$\xi = 1$	$\xi = 0$	$\xi = 1$	$\xi = 0$
	4	0.03051297	0.04613782	-3.06231058	-4.50669680
	6	0.02070912	0.03069662	-2.06558281	-2.94254494
	8	0.01604188	0.02342252	-1.58606227	-2.19846734
	12	0.01140586	0.01627413	-1.10484608	-1.45983861
0.01	16	0.00911651	0.01275412	-0.86284384	-1.09014261
	24	0.00567171	0.00929034	-0.61847086	-0.71718699
	28	0.00624375	0.00831570	-0.54751444	-0.60899295
	∞	0.0142(53)	0.010085(95)	-0.1159(19)	0.1791(71)
	4	0.03511824	0.05076104	-0.70002402	-0.89478086
	6	0.02586957	0.03586130	-0.49326654	-0.57131307
	8	0.02161898	0.02900166	-0.39027728	-0.41227203
	12	0.01749555	0.02236487	-0.28070367	-0.24625620
0.05	16	0.01552171	0.01916007	-0.21982997	-0.15613470
	24	0.01365601	0.01607513	-0.14889542	-0.05413055
	28	0.01315297	0.01522533	-0.12501221	-0.02074331
	∞	0.010088(9)	0.002392(62)	0.0175(11)	0.0459(16)

Table 6.7: Renormalisation parameters for massive HISQ quarks. I extrapolate the results to $L = \infty$. Results at finite lattice spacing use modesummation and are therefore exact. Uncertainties for the $L = \infty$ results are from the polynomial fit.

am_q	L	Z_m		Z_ψ	
		$\xi = 1$	$\xi = 0$	$\xi = 1$	$\xi = 0$
	4	0.04021517	0.05588301	-0.38471270	-0.42329209
	6	0.03144242	0.04144233	-0.27003185	-0.24824283
	8	0.02754374	0.03493137	-0.20866792	-0.15688533
	12	0.02382350	0.02869585	-0.13745787	-0.05434727
0.10	16	0.02208393	0.02572454	-0.09374485	0.00631186
	24	0.02046735	0.02288796	-0.03806222	0.08087924
	28	0.02002501	0.02209865	-0.01821517	0.10676488
	∞	0.017421(17)	0.017416(10)	0.1026(68)	0.2642(79)
	4	0.05594294	0.07173053	-0.12182111	-0.05634316
	6	0.04825177	0.05831329	-0.05900989	0.02925742
	8	0.04514575	0.05257860	-0.01968736	0.08121890
	12	0.04203358	0.04693684	0.03140938	0.14692902
0.30	16	0.04030510	0.04396936	0.06536116	0.18964292
	24	0.03810375	0.04054048	0.11094060	0.24600307
	28	0.03727723	0.03936478	0.12778618	0.26658286
	∞	0.0.32560(58)	0.033352(23)	0.2310(11)	0.3926(74)

Table 6.8: Renormalisation parameters for massive HISQ quarks. I extrapolate the results to $L = \infty$. Results at finite lattice spacing use modesummation and are therefore exact. Uncertainties for the $L = \infty$ results are from the polynomial fit.
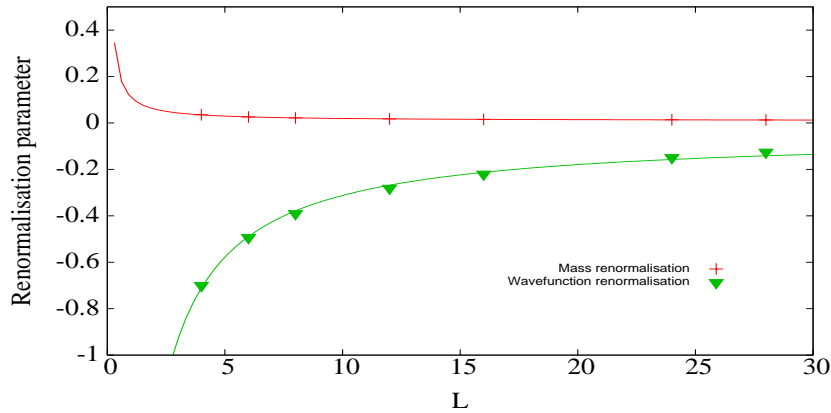
Figure 6.6: Plot of the infinite volume extrapolation of HISQ renormalisation parameters in Feynman gauge. I plot results for the mass renormalisation, in red, and the wavefunction renormalisation in green. I use a light quark mass of $am_q = 0.1$.

6.6.4 Lattice operator matching

I now present my results for the lattice vertex corrections. I used three different sets of actions to calculate the vertex corrections, with seven different combinations of heavy quark mass and stability parameter for each set of actions. I used a gluon mass as the infrared regulator. The vertex correction ζ_{00} is infrared divergent in Feynman gauge, so I extracted the finite contribution using a subtraction function and a gluon mass of $a^2\lambda^2 = 10^{-6}$. I use the subtraction function method to speed up the code because the computation of the vertex correction is relatively computationally expensive.

The subtraction function depends on the heavy quark mass, but as an example I plot a fit to the logarithmic infrared behaviour of the subtraction function with heavy quark mass $aM = 2.8$ in Figure 6.7. This plot demonstrates that the infrared structure is correctly handled by the subtraction function. Using a constrained fit to the logarithmic divergence, which must match the known analytic continuum result, I obtain

$$F_{\zeta_{00}}^{\text{sub,finite}} = -0.221626(75) \qquad (6.73)$$

for the finite contribution to the subtraction function. In Landau gauge ζ_{00}
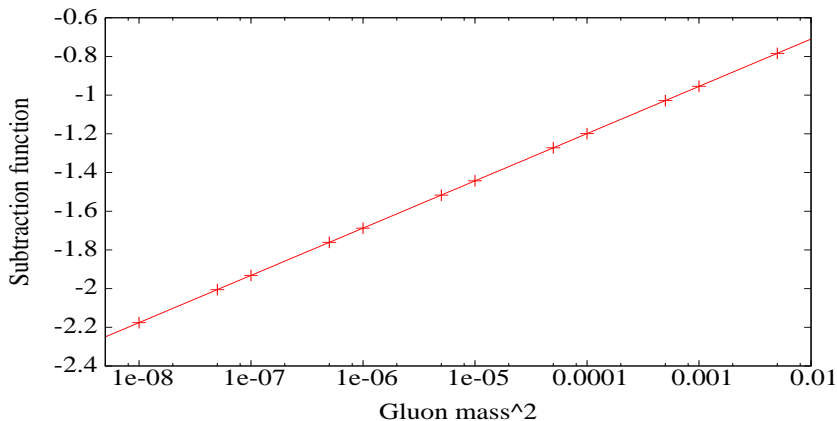
Figure 6.7: Plot of the infrared behaviour of the subtraction function, with a constrained fit to the data. I use a heavy quark mass of $aM = 2.8$. Uncertainties are smaller than the data points.

is infrared finite, whilst the vertex correction ζ_{10} is infrared finite and gauge-independent. The sets of actions I used are as follows:

- The "onlyH0" NRQCD action with unimproved staggered quarks and unimproved Wilson gluons, Table 6.9. I used 10^7 function evaluations and 20 VEGAS iterations, which took about one hour on six processors for each gluon mass.

- Highly-improved NRQCD with ASQTad light quarks and Symanzik-improved gluons, Table 6.10. I used 5×10^5 function evaluations and 20 VEGAS iterations, which took about five minutes on twelve processors for each gluon mass. I give results for the kernel ordering BACAB for the NRQCD action (I review this issue in more detail in Section 5.2.2).

- Highly-improved NRQCD with HISQ light quarks and Symanzik-improved gluons, Table 6.11. I used 10^7 function evaluations and 20 VEGAS iterations, which took about one hour on six processors for each gluon mass. I use the NRQCD kernel ordering BACAB.

I am now able to extract the mixing coefficient $\widetilde{\rho}_0$, which I define in Equation (6.63). I present my final results for massless HISQ light quarks,

142

aM	n	ζ_{00}		ζ_{10}
		$\xi = 1$	$\xi = 0$	
5.40	1	0.622(1)	0.1194(3)	-0.1436(1)
4.00	2	0.592(1)	0.0865(2)	-0.1813(1)
2.80	2	0.544(1)	0.0381(2)	-0.2270(1)
2.10	4	0.524(1)	0.0158(1)	-0.2746(2)
1.95	2	0.508(1)	0.0016(1)	-0.2726(2)
1.95	4	0.517(1)	0.0093(1)	-0.2853(2)
1.60	4	0.503(1)	-0.0048(1)	-0.3133(2)

Table 6.9: Results for the vertex corrections at seven different quark mass and stability parameter combinations. All results use the "onlyH0" NRQCD action with massless unimproved staggered quarks.

aM	n	ζ_{00}		ζ_{10}
		$\xi = 1$	$\xi = 0$	
5.40	1	0.685(1)	0.1784(1)	-0.0952(1)
4.00	2	0.744(1)	0.2371(2)	-0.1235(1)
2.80	2	0.835(1)	0.3279(2)	-0.1658(1)
2.10	4	0.932(2)	0.4242(3)	-0.2100(1)
1.95	2	0.960(2)	0.4528(3)	-0.2227(1)
1.95	4	0.961(2)	0.4513(3)	-0.2189(1)
1.60	4	1.048(2)	0.5391(3)	-0.2599(2)

Table 6.10: Results for the vertex corrections at seven different quark mass and stability parameter combinations. All results use highly-improved NRQCD and massless ASQTad quarks.

with highly-improved NRQCD heavy quarks and Symanzik-improved gluons in Table 6.12.

6.6.5 Comparison to the literature

In Table 6.13 I show the results for the leading order vertex corrections calculated for highly-improved NRQCD with massless ASQTad quarks in

aM	n	ζ_{00}		ζ_{10}
		$\xi = 1$	$\xi = 0$	
5.40	1	0.622(1)	0.1147(1)	-0.0615(1)
4.00	2	0.657(1)	0.1505(1)	-0.0806(1)
2.80	2	0.712(1)	0.2054(2)	-0.1104(1)
2.10	4	0.771(1)	0.2624(2)	-0.1417(1)
1.95	2	0.786(1)	0.2791(2)	-0.1510(1)
1.95	4	0.787(1)	0.2785(2)	-0.1511(1)
1.60	4	0.838(1)	0.3291(3)	-0.1789(1)

Table 6.11: Results for the vertex corrections at seven different quark mass and stability parameter combinations. All results use highly-improved NRQCD and massless HISQ quarks.

aM	n	$\widetilde{\rho}_0$		ζ_{10}	ρ_0	
		$\xi = 1$	$\xi = 0$		$\xi = 1$	$\xi = 0$
5.40	1	0.243(2)	-0.284(2)	-0.0615(1)	0.305(2)	0.858(2)
4.00	2	0.239(2)	-0.291(2)	-0.0806(1)	0.319(2)	-0.210(2)
2.80	2	0.266(2)	-0.262(2)	-0.1104(1)	0.377(2)	-0.152(2)
2.10	4	0.317(2)	-0.210(2)	-0.1417(1)	0.458(2)	-0.068(2)
1.95	2	0.350(2)	-0.175(2)	-0.1510(1)	0.501(2)	-0.024(2)
1.95	4	0.341(2)	-0.186(2)	-0.1511(1)	0.492(2)	-0.034(2)
1.60	4	0.421(2)	-0.105(2)	-0.1789(1)	0.600(2)	0.074(2)

Table 6.12: Results for the mixing coefficient $\widetilde{\rho}_0$ for massless HISQ light quarks with highly-improved NRQCD and Symanzik-improved gluons.

[89]. We can directly compare the values in Table 6.13 with my results in Table 6.10. We see my results are in excellent agreement with those of [89]. This agreement provides strong confidence in the fully automated method that I use to extract my results.

aM	n	ζ_{00}	ζ_{10}
5.40	1	0.687(4)	-0.095
4.00	2	0.746(4)	-0.123
2.80	2	0.836(4)	-0.166
2.10	4	0.932(4)	-0.210
1.95	2	0.958(4)	-0.222
1.95	4	0.961(4)	-0.219
1.60	4	1.048(4)	-0.259
1.20	6	1.207(4)	-0.329
1.00	6	1.341(4)	-0.378

Table 6.13: Results for the vertex corrections from [89] at 10 different quark mass and stability parameter combinations. All values use highly-improved NRQCD with massless ASQTad quarks in Feynman gauge. The authors of [89] do not provide explicit values for ζ_{00}, but these values are easily extracted from their data.

6.7   Conclusions and outlook

In this chapter I have computed the massless relativistic quark wavefunction renormalisation, the massive HISQ renormalisation parameters and the vertex corrections to the leading order heavy-light lattice currents. These results, which I obtained for three different sets of actions, enabled me to extract the leading order matching coefficient between the temporal component of the heavy-light current in continuum QCD and on the lattice. My results for ASQTad light quarks serve as a check of my code and are in perfect agreement with the results given in [89].

My results using HISQ light quarks will serve as an input into the HPQCD collaboration's determination of the f_B and f_{B_s} decay constants. The HPQCD collaboration has previously calculated these decay constants using the MILC ensembles with ASQTad light quarks [50, 107, 108, 109]. However, there is currently tension between the value of $|V_{ub}|$ determined from experimental measurements of $B^{\pm} \to \tau^{\pm}\nu$ and from determinations using global fits to the CKM parameters [110]. Experimental data from the LHCb and the pro-

posed SuperB factory will improve the experimental resolution by an order of magnitude and corresponding improvements in the theoretical inputs are required. The HPQCD collaboration are therefore calculating the decay constants f_{B_s} and f_{D_s} using NRQCD with HISQ light quarks, which should improve the precision of the the decay constants [111].

My work can be progressively extended in a number of steps. As part of the HPQCD collaboration's calculation of the form factors for semileptonic B decays, such as $\overline{B} \to \pi \ell \overline{\nu}_\ell$, the spatial components of the vector current, including non-leading $1/M$ corrections, will need to be determined. For the $B \to \pi$, $B \to K$ and $B_s \to K$ decays, massless HISQ light quarks are sufficient. Massive light quarks will be required for the $B \to D$ and $B_s \to D_s$ decays.

To facilitate this final extension, the massless continuum calculation will also need to be calculated numerically using automated lattice perturbation theory and extrapolated to the continuum limit. The analytic calculation is complicated by the presence of two different scales and this is where the use of a numerical calculation on fine lattices will help. The relativistic calculation can be extended very simply by using massive light quark vertex files, with little additional modification required.

Chapter 7

Conclusions and outlook

Lattice perturbation theory plays an important role in the extraction of precise predictions of physical processes from lattice simulations. Modern actions, such as HISQ and NRQCD, are highly-improved, which greatly reduces the discretisation effects and systematic errors associated with nonperturbative simulations. The price, however, is that calculating perturbative quantities is no longer feasible by hand. In this dissertation I have applied automated lattice perturbation theory to a number of perturbative calculations involving highly-improved actions at both one- and two-loops.

In the first chapter I introduce the basic formalism of lattice QCD and highlight the important role that lattice perturbation theory plays in extracting precise results from lattice simulations. In the second chapter I motivate and justify lattice perturbation theory in more detail and introduce several tools of the trade: automation algorithms, twisted boundary conditions and background field gauge.

In the course of this dissertation I performed a number of calculations using the automated perturbation theory routines `HiPPy` and `HPsrc`. I review and summarise these calculations in the following sections. I also discuss some open issues and indicate directions for future work.

7.1   Tadpole improvement

In Section 4.1 I calculate the tadpole improvement factors for both Landau and plaquette tadpoles. I confirm previous one-loop results and obtain, for the first time, the fermionic contributions to the two-loop tadpole improvement factors. I combine my results with data from high-β simulations carried out by Lee [11] to present the first calculation of the plaquette tadpole at two-loops for Symanzik-improved gluons with ASQTad light quarks. I also connect my results with those of [12] to extract the full two-loop Landau tadpole, again

for Symanzik-improved gluons with ASQTad light quarks. I then use data from simulations by the HPQCD collaboration [93] to estimate the three-loop contribution to both Landau and plaquette tadpoles. I find agreement with the study in [86] that the nonperturbative Landau tadpoles are well-described by the two-loop approximation.

Current simulations by the HPQCD collaboration use HISQ light quarks, for which the two-loop tadpole improvement factors need to be calculate. This calculation is complicated by the reunitarisation operators in the HISQ action, but the modular nature of the `HPSRC` modules that I wrote to compute the tadpole improvement factors ensures that my results can extended to HISQ with relative ease.

7.2   Operator improvement

I calculate the one-loop corrections to the higher order kinetic operators in the NRQCD action in Section 4.4. I use a mix of analytic and numerical integration to extract the one-loop corrections for two simple NRQCD actions. I demonstrate that these corrections are infrared divergent unless the action is improved to the appropriate order. I compare my results to those obtained by Müller using a fully automated procedure in [47] and the agreement of our results provides confidence in both methods.

This work was motivated by the HPQCD collaboration's discovery of large spin splittings between mesonic states with the same total spatial momentum, but different components of the momentum, in nonperturbative NRQCD simulations. These spin splittings were removed by nonperturbatively tuning the coefficient of the $\mathcal{O}(a^4 p^4)$ kinetic operator in the NRQCD action to a value of 2.6 [47]. Unfortunately this nonperturbative result is inconsistent with the one-loop corrections, which were found to be relatively small, approximately 0.4 for a range of heavy quark masses between $aM = 2.0$ and $aM = 3.4$ [47].

There are a number of other sources that could contribute to the discrepancy between these results. The first possibility is a large two-loop correction to the perturbative result. Two-loop perturbative results would be required to confirm this, but the complexity of two-loop lattice perturbation theory

in this case would be formidable.

A second possibility is that $\mathcal{O}(a^6 p^6)$ corrections strongly influence the correction coefficient. Obtaining higher order kinetic corrections may prove necessary in the future and in Appendix D I briefly discuss extending my work to $\mathcal{O}(a^6 p^6)$ to investigate the feasibility of further radiative improvement. However, this may not prove necessary. In the nonperturbative simulations, the $\mathcal{O}(a^6 p^6)$ improvement term was included with the tree-level value of the coefficient. The fitting process, whereby the $\mathcal{O}(a^6 p^6)$ was fixed to its classical value and the coefficient of the $\mathcal{O}(a^4 p^4)$ term nonperturbatively tuned, may not be optimal and indeed could be another source of the difference in perturbative and nonperturbative results. Finally, there may be errors introduced by the relative coarseness of the lattice used in these simulations.

Further work is needed to clarify this discrepancy. Nonperturbative simulations on finer lattices are being explored and these may shed light on the issue. Extending the perturbative renormalisation calculation to $\mathcal{O}(\alpha_s a^6 p^6)$ and $\mathcal{O}(\alpha_s^2 a^4 p^4)$ could also illuminate the problem more brightly. However, the computational complexity of this extension is impressive and not to be underestimated.

I also briefly review the calculation of the one-loop radiative correction to the chromo-magnetic operator in the highly-improved NRQCD action. This calculation was undertaken by Hammant [14] and is the first outcome of our development and implementation of background field gauge in the HPSRC and HIPPY routines.

As part of the development of our implementation of background field gauge I derived background field gauge Feynman rules. I also hardwired the ghost-gluon vertices in an HPSRC routine. A calculation of the known ratio between the QCD scale parameter on the lattice and in the $\overline{MS}$ scheme using the gluon selfenergy in background field gauge will serve as a further check of our background field gauge implementation. This computation will build on my analysis of the Ward identities for the gluon selfenergy.

7.3   The b quark mass

In Chapter 5 I calculate the one-loop renormalisation parameters for a variety of NRQCD actions. The modules I wrote for these calculations were the basis of my computation of the fermionic contributions to the two-loop heavy quark energy shift. To my knowledge this calculation is the first two-loop calculation carried out for lattice NRQCD.

I combine my results with data extracted from high-β simulations data undertaken by Lee [11] to determine the full heavy quark energy shift at two-loops. With this result, I then extract a new prediction of the mass of the b quark from nonperturbative studies by Dowdall and the HPQCD collaboration [93]. My results are in good agreement with recent studies by three other lattice collaborations and improves significantly on the previous determination by the HPQCD collaboration using lattice NRQCD. I reduced the uncertainty in the prediction to approximately one percent by removing the dominant contribution to the uncertainty in the b quark mass, which came from the two-loop energy shift.

The dominant sources of uncertainty in my results are the three-loop heavy quark energy shift and the systematic uncertainties arising from lattice artifacts. Results from Lee provide an estimate of the quenched three-loop contribution [11], but the fermionic contribution is yet to be determined. In principle, this is a possible extension of my work. However, there are a large number of diagrams to compute at three-loops and in practice, it may be more feasible to extract higher order contributions from high-β simulations. New simulations at different heavy quark masses are required for a more complete understanding of the lattice artifact errors.

7.4   Heavy-light currents

Finally, in Chapter 6, I compute the matching coefficients between heavy-light currents in continuum QCD and NRQCD with massless HISQ light quarks. I include only the leading order contributions in the inverse heavy quark mass expansion. As part of this process, I confirm the results of [89],

which used highly-improved NRQCD with massless ASQTad light quarks. The temporal component of the axial-vector and vector currents serve as inputs into the HPQCD collaboration's determination of the f_B and f_{B_s} decay constants.

There are a number of stages to the extension of this work. As part of the HPQCD collaboration's calculation of the semi-leptonic B decays, the spatial components of the vector current, including non-leading $1/M$ corrections, will need to be determined. For the $B \to \pi$, $B \to K$ and $B_s \to K$ decays, massless HISQ light quarks are sufficient. However, for the $B \to D$ and $B_s \to D_s$ decays, non-zero mass light quarks will be required. This final extension will require the continuum massive light quark calculation. Rather than extending the analytic continuum calculation, my HiPPy and HPSRC code can be developed to compute the continuum results numerically, using relativistic quarks on fine lattices with high statistics. This will simplify the extension to massive light quarks, which would otherwise be technically involved if performed analytically.

Appendix A

Conventions

In this appendix I summarise the conventions and notation that I employ in this dissertation.

A.1 Notation

Units I use units in which $\hbar = c = 1$.

Indices Greek indices run from 0 to 3; latin indices run from 1 to 3.

Metric The Minkowski metric is $g_{\mu\nu} = \mathrm{diag}(1, -1, -1, -1)$; the Euclidean metric is $\delta_{\mu\nu} = \mathrm{diag}(1, 1, 1, 1)$.

Wick rotation I relate Euclidean four-vectors, denoted $(\tau, \mathbf{x})$, and derivatives to their Minkowski counterparts, denoted $(t, \mathbf{x}^M)$, as follows:

$$\tau = it, \qquad\qquad x_j = x^j = x_M^j = -x_j^M. \qquad (\text{A.1})$$

I relate derivatives via

$$\partial_0 = \partial^0 = -i\partial_M^0 = -i\partial_0^M, \qquad\qquad \partial_j = \partial^j = -\partial_M^j = \partial_j^M. \qquad (\text{A.2})$$

Gauge fields I define the gauge field as

$$A_0 = A^0 = -iA_M^0 = -iA_0^M, \qquad\qquad A_j = A^j = -A_M^j = A_j^M. \qquad (\text{A.3})$$

Chromo-electric and -magnetic fields I relate the Euclidean chromo-electric and chromo-magnetic fields to the Euclidean field strength tensor

$$E_i = -F_{0i}, \qquad\qquad B_i = -\frac{1}{2}\epsilon_{ijk}F_{jk}. \qquad (\text{A.4})$$

Dirac algebra   Euclidean gamma matrices, $\widehat{\gamma}_\mu$, satisfy

$$\{\widehat{\gamma}_\mu, \widehat{\gamma}_\nu\} = 2\delta_{\mu\nu}. \tag{A.5}$$

I relate the Euclidean gamma matrices to the Minkowski gamma matrices, γ_μ, as follows:

$$\widehat{\gamma}_0 = \widehat{\gamma}^0 = \gamma^0 = \begin{pmatrix} \sigma^0 & 0 \\ 0 & -\sigma^0 \end{pmatrix}, \qquad \widehat{\gamma}_j = -i\gamma^j = \begin{pmatrix} 0 & -i\sigma^j \\ i\sigma^j & 0 \end{pmatrix}, \tag{A.6}$$

$$\widehat{\gamma}_5 = \widehat{\gamma}_0\widehat{\gamma}_1\widehat{\gamma}_2\widehat{\gamma}_3 = \gamma_5 = \begin{pmatrix} 0 & \sigma^0 \\ \sigma^0 & 0 \end{pmatrix}. \tag{A.7}$$

A.2   Lattice derivatives and field strength

I now give explicit expressions for the derivatives that I use in the lattice actions throughout this dissertation. I denote link variables by $U_\mu(x)$.

Elementary forward, backward and symmetric difference operators

$$\Delta_\mu^+\psi(x) = U_\mu(x)\psi(x + \hat{\mu}) - \psi(x), \tag{A.8}$$

$$\Delta_\mu^-\psi(x) = \psi(x) - U_{-\mu}(x)\psi(x - \hat{\mu}), \tag{A.9}$$

$$\Delta_\mu^\pm\psi(x) = \frac{1}{2}\Big[U_\mu(x)\psi(x + \hat{\mu}) - U_{-\mu}(x)\psi(x - \hat{\mu})\Big]. \tag{A.10}$$

Unimproved derivative

$$\Delta^{(2n)} = \sum_{i=1}^{3}(\Delta_i^+\Delta_i^-)^n. \tag{A.11}$$

Improved derivatives

$$\widetilde{\Delta}_\mu^\pm = \Delta_\mu^\pm - \frac{1}{6}\Delta_i^+\Delta_i^\pm\Delta_i^-, \tag{A.12}$$

$$\widetilde{\Delta}^{(2n)} = \frac{1}{12}\sum_{i=1}^{3}\Delta_i^+\Delta_i^-\Delta_i^+\Delta_i^-. \tag{A.13}$$

Improved field strength tensor

$$
\widetilde{F}_{\mu\nu}(x) = \frac{5}{3}F_{\mu\nu}(x) - \frac{1}{6}\Big[U_\mu(x)F_{\mu\nu}(x+\hat{\mu})U_\mu^\dagger(x) + U_{-\mu}(x)F_{\mu\nu}(x-\hat{\mu})U_{-\mu}^\dagger(x)
$$
$$
- U_\nu(x)F_{\nu\mu}(x+\hat{\nu})U_\nu^\dagger(x) - U_{-\nu}(x)F_{\nu\mu}(x-\hat{\nu})U_{-\nu}^\dagger(x)\Big], \qquad \text{(A.14)}
$$

where

$$
F_{\mu\nu}(x) = -\frac{i}{2g}\Big(\Omega_{\mu\nu}(x) - \Omega_{\mu\nu}^\dagger(x)\Big),
$$
$$
\Omega_{\mu\nu}(x) = \frac{1}{4}\sum_{\{(\alpha,\beta)\}} U_\alpha(x)U_\beta(x+\widehat{\alpha})U_{-\alpha}(x+\widehat{\alpha}+\widehat{\beta})U_{-\beta}(x+\widehat{\beta}), \qquad \text{(A.15)}
$$

and

$$
\{(\alpha,\beta)\} = \{(\mu,\nu),(\nu,-\mu),(-\mu,-\nu),(-\nu,\mu)\} \quad \text{for} \quad \mu \neq \nu. \qquad \text{(A.16)}
$$

A.3   Lattice fields in Fourier space

For the purposes of deriving Feynman rules, I give the Fourier series representation of lattice fields.

Gauge fields   Lattice gauge fields are defined on the links between lattice sites:

$$
A_\mu^a(x) = \int_{-\pi/a}^{\pi/a} \frac{\mathrm{d}^4 p}{(2\pi)^4} e^{ip(x+\hat{\mu}/2)}\widetilde{A}_\mu^a(p), \qquad \text{(A.17)}
$$

with inverse

$$
\widetilde{A}_\mu^a(p) = \sum_x e^{-ip(x+\hat{\mu}/2)}A_\mu^a(x). \qquad \text{(A.18)}
$$

Fermion fields   Lattice fermions live on the lattice sites themselves:

$$
\psi(x) = \int_{-\pi/a}^{\pi/a} \frac{\mathrm{d}^4 p}{(2\pi)^4} e^{ipx}\widetilde{\psi}(p), \qquad \text{(A.19)}
$$

where

$$\widetilde{\psi}(p) = \sum_x e^{-ipx}\psi(x). \tag{A.20}$$

Ghost fields   Ghosts have Fourier series representation

$$c^a(x) = \int_{-\pi/a}^{\pi/a} \frac{\mathrm{d}^4 p}{(2\pi)^4} e^{ipx}\widetilde{c}^a(p), \tag{A.21}$$

where

$$\widetilde{c}^a(p) = \sum_x \frac{\mathrm{d}^4 p}{(2\pi)^4} e^{-ipx} c^a(x). \tag{A.22}$$

Appendix B

Lattice Feynman rules

In this appendix I derive Feynman rules for two simple discretisations of NRQCD, for a quenched gauge action in background field gauge and for the current operators used in Chapter 6. I give the Fourier series representations of the lattice fields in Appendix A.

B.1 NRQCD: Davies and Thacker action

One choice of discretisation for an unimproved NRQCD heavy quark action is given in Davies and Thacker [49]:

$$
S_{\mathrm{DT}} = \sum_{x,t} \psi^\dagger(x) \left(\Delta_4 - \sum_{j=1}^{3} \frac{\Delta^{(2)}}{2M} \right) \psi(x).
$$

Here I implicitly trace over $SU(3)$ colour generators. For all order three vertices (and higher), there is an overall minus sign factor that must be included because the Euclidean path integral weight is e^{-S}, rather than the Minkowskian e^{iS}. For these higher order vertices, I consider $S \rightarrow -S$. Throughout this appendix, I set the lattice spacing to unity, $a = 1$. I take colour factors directly from [49].

The Davies and Thacker action has Green function evolution equation

$$
U_4(\mathbf{x},t)G(\mathbf{x},t+1) - \left(1 + \frac{\Delta^{(2)}}{2M} \right) G(\mathbf{x},t) = \delta(t)\delta(\mathbf{x}), \qquad \text{(B.1)}
$$

with solution

$$
G(\mathbf{x},t+1) = U_4^\dagger(\mathbf{x},t) \left(1 + \frac{\Delta^{(2)}}{2M}G(\mathbf{x},t-1) + \delta(t)\delta(\mathbf{x}) \right) \qquad \text{(B.2)}
$$

and initial conditions $G(\mathbf{x},t) = 0$ for $t \leq 0$.

Explicitly writing out the link variables in the covariant difference oper-

ators, the Davies and Thacker action becomes

$$
S_{\mathrm{DT}} = \sum_{x,t} \left\{ \psi(x)^{\dagger} U_4(x) \psi(\mathbf{x}, t+1) - \psi(x)^{\dagger} \psi(x) - \frac{1}{2M} \sum_{j=1}^{3} \left[-2\psi(x)^{\dagger} \psi(x) \right. \right.
$$
$$
\left. \left. + \psi(x)^{\dagger} U_j(x) \psi(\mathbf{x}+j, t) + \psi(x)^{\dagger} U_j^{\dagger}(\mathbf{x}-j) \psi(\mathbf{x}-j, t) \right] \right\}. \tag{B.3}
$$

In this appendix, I employ a variant of the vertex notation of [77] and [78]. A general vertex $V^{(i,j,k,l)}(m, p, q, r, s)_{\mu\nu\rho\tau}^{abcd}$ has i fermion legs, j background field legs, k quantum gluon legs and $2l$ ghost legs (one ghost and one antighost). All momenta are incoming, with $\delta(m+p+q+r+s) = 0$ and I take the colour indices to be associated with the ordering (i, j, k, l). The Lorentz indices are associated with the ordering (j, k, l), that is, the quarks do not carry Lorentz indices. For example, for the vertex $V^{(0,1,1,1)}(p, q, r, s)_{\mu\nu\rho\sigma}^{abcd}$ the associated fields are $B_\mu^a(p)$, $q_\nu^b(q)$, $c_\rho^c(r)$ and $\bar{c}_\sigma^d(s)$.

B.1.1   Two-point vertices

We obtain the inverse quark propagator from the leading order terms in the continuum expansion of the link variables (with no sum over μ),

$$
U_\mu(x) = 1 - igT^a A_\mu^a(x) + \frac{g^2}{2} T^a A_\mu^a T^b A_\mu^b + \mathcal{O}(g^3).
$$

We Fourier expand the heavy quark fields to give

$$
S_{\mathrm{DT}}^{(0)} = \sum_{x,t} \sum_{p,p'} \widetilde{\psi}^{\dagger}(p') \widetilde{\psi}(p) e^{i(p_0 - p_0')t} e^{i(\mathbf{p}-\mathbf{p}') \cdot \mathbf{x}}
$$
$$
\times \left[e^{ip_0} - 1 + \frac{1}{2M} \sum_j (e^{-ip_j} + e^{ip_j} - 2) \right]
$$
$$
= \sum_{p,p'} \widetilde{\psi}^{\dagger}(p') \widetilde{\psi}(p) \delta(p - p') \left[e^{ip_0} - 1 + \frac{4}{2M} \sum_j \sin^2 \left(\frac{p_j}{2} \right) \right].
$$

Hence the corresponding Feynman rule is

$$V^{(2,0,0,0)}(p,-p)^{ab} = \delta^{ab}\left(e^{ip_0} - 1 + \frac{1}{2M}\sum_j \widehat{p}_j^2\right) \qquad (B.4)$$

for the inverse heavy quark propagator. In this expression I have used the common lattice notation

$$\widehat{p}_\mu = 2\sin\left(\frac{p_\mu}{2}\right). \qquad (B.5)$$

B.1.2 Three-point vertices

The nonrelativistic expansion for NRQCD breaks the symmetry between temporal and spatial directions and introduces separate Feynman rules for temporal and spatial gluon vertices. For the temporal gluon three-point vertex, only one term contributes:

$$\psi(x)^\dagger U_4(x)\psi(\mathbf{x}, t+1). \qquad (B.6)$$

We expand the link variable in terms of the gluon fields

$$S_{\mathrm{DT}}^{(1,T)} = -ig\sum_{x,t}\psi(x)^\dagger A_0(x)\psi(\mathbf{x}, t+1), \qquad (B.7)$$

which has Fourier series representation

$$\begin{aligned}
S_{\mathrm{DT}}^{(1)} &= -ig\sum_{x,t}\sum_{p',p,k}\widetilde{\psi}^\dagger(p')\widetilde{A}_0(k)\widetilde{\psi}(p)e^{i(p_0-p_0'+k_0)t}e^{i(\mathbf{p}-\mathbf{p}'+\mathbf{k})\cdot\mathbf{x}}e^{ik_0/2}e^{ip_0} \\
&= -ig\sum_{p',p}\widetilde{\psi}^\dagger(p)\widetilde{\psi}(p)\widetilde{A}_0(k)\delta(p-p'+k)e^{i(p_0'+p_0)/2},
\end{aligned}$$

so the corresponding Feynman rule is

$$V^{(2,0,1,0)}(p,q,r)_0^{abc} = -ig(T^c)^{ab}e^{i(p_0+q_0)/2}. \qquad (B.8)$$

The $\mathcal{O}(g)$ spatial terms in Equation (B.3) are

$$S_{\mathrm{DT}}^{1,S} = -ig \sum_{x,t} \left(\psi(x)^\dagger A_j(x)\psi(\mathbf{x}+j,t) + \psi(x)^\dagger A_j(\mathbf{x}-j)\psi(\mathbf{x}-j,t) \right),$$

which have Fourier space representation

$$S_{\mathrm{DT}}^{0,S} = -\frac{ig}{2M} \sum_j \sum_{p',p} \widetilde{\psi}^\dagger(p')\widetilde{\psi}(p)\widetilde{A}(k)\delta(p-p'+k) \left(e^{i(p+p')_j/2} - e^{-i(p+p')_j/2} \right),$$

(B.9)

and consequently an associated Feynman rule

$$V^{(2,0,1,0)}(p,q,r)_j^{abc} = -\frac{g}{2M}(T^c)^{ab}(\widehat{p+q})_j.$$

(B.10)

The derivations of the four-point vertices follow a similar pattern. I have derived these expression, but only state them here. The four-point vertices are

$$V^{(2,0,2,0)}(p,q,r,s)_{00}^{abcd} = \frac{g^2}{2}(T^cT^d)^{ab}\exp\left(\frac{i(p_0+q_0)}{2} \right)$$

(B.11)

and

$$V^{(2,0,2,0)}(p,q,r,s)_{jk}^{abcd} = -\delta_{jk}\frac{g^2}{2M}(T^cT^d)^{ab}\cos\left(\frac{p_j+q_j}{2} \right) \left[1 - \frac{1}{2M}\sum_j \widehat{p^2} \right].$$

(B.12)

B.2 NRQCD: "onlyH0" action

An alternative discretisation of an unimproved NRQCD heavy quark action is

$$S_H = \sum_{x,t} \psi^\dagger(x) \left[\psi(\mathbf{x},t) - U_4^\dagger(\mathbf{x},t-1)\left(1 + \frac{\Delta^{(2)}}{2M} \right)\psi(\mathbf{x},t-1) \right] \quad (B.13)$$

where I again implicitly trace over $SU(3)$ colour generators. In this case the action has an associated Green function evolution equation given by

$$G(\mathbf{x},t) - U_4^\dagger(\mathbf{x},t-1)\left(1 + \frac{\Delta^{(2)}}{2M}\right)G(\mathbf{x},t-1) = \delta(t)\delta(\mathbf{x}), \qquad \text{(B.14)}$$

with solution

$$G(\mathbf{x},t) = U_4^\dagger(\mathbf{x},t-1)\left(1 + \frac{\Delta^{(2)}}{2M}\right)G(\mathbf{x},t-1) + \delta(t)\delta(\mathbf{x}) \qquad \text{(B.15)}$$

and initial conditions $G(\mathbf{x},t) = 0$ for $t < 0$.

To clarify the following derivations I again write out the link variables explicitly:

$$
\begin{aligned}
S_H = \sum_{x,t}\Big\{ &\psi^\dagger(x)\psi(x) - \psi^\dagger(x)U_4^\dagger(\mathbf{x},t-1)\psi(\mathbf{x},t-1) \\
&-\frac{1}{2M}\sum_j\Big[\psi^\dagger(x)U_4^\dagger(\mathbf{x},t-1)U_j(x)\psi(\mathbf{x}+\hat{j},t-1) + \psi^\dagger(x)U_4^\dagger(\mathbf{x},t-1) \\
&\times U_j(x-\hat{j})^\dagger\psi(\mathbf{x}-\hat{j},t-1) - 2\psi^\dagger(x)U_4^\dagger(\mathbf{x},t-1)\psi(\mathbf{x},t-1)\Big]\Big\}.
\end{aligned}
$$
$$\text{(B.16)}$$

B.2.1 Two-point vertices

For the action of Equation (B.13), we Fourier expand the heavy quark fields and use the leading order terms in the continuum expansion of the link variables to give

$$
\begin{aligned}
S_H^{(0)} &= \sum_{x,t}\sum_{p,p'}\widetilde{\psi}^\dagger(p')\widetilde{\psi}(p)e^{i(p_0-p_0')t}e^{i(\mathbf{p}-\mathbf{p}')\cdot\mathbf{x}} \\
&\quad\times\left[1 - e^{-ip_0} - \frac{e^{-ip_0}}{2M}\sum_j(e^{-ip_j}+e^{ip_j}-2)\right] \\
&= \sum_{p,p'}\widetilde{\psi}^\dagger(p')\widetilde{\psi}(p)\delta(p-p')\left[1 - e^{-ip_0} - \frac{e^{-ip_0}}{2M}\sum_j\widehat{p}_j^2\right].
\end{aligned}
$$

Hence the Feynman rule for the inverse heavy quark propagator is

$$V^{(2,0,0,0)}(p,-p)^{ab} = \delta^{ab}\left[1 - e^{-ip_0}\left(1 + \frac{1}{2M}\sum_j \widehat{p}_j\right)\right]. \qquad (B.17)$$

B.2.2 Higher order vertices

The derivation of the three- and four-point vertices follows exactly the scheme of the derivation for the Davies and Thacker action, so I simply state the results here.

The three-point vertices are

$$V^{(2,0,1,0)}(p,q,r)^{abc}_0 = -ig(T^c)^{ab}e^{-i(p_0+q_0)/2}\left[1 - \frac{1}{2M}\sum_j \widehat{p}_j^2\right] \qquad (B.18)$$

and

$$V^{(2,0,1,0)}(p,q,r)^{abc}_j = -\frac{g}{2M}(T^c)^{ab}e^{-ip_0}(\widehat{p+q})_j. \qquad (B.19)$$

The four-point vertices are

$$V^{(2,0,2,0)}(p,q,r,s)^{abcd}_{00} = -\frac{g^2}{2}(T^cT^d)^{ab}\exp\left(-\frac{i(p_0+q_0)}{2}\right)\left[1 - \frac{1}{2M}\sum_j \widehat{p}_j^2\right] \tag{B.20}$$

and

$$V^{(2,0,2,0)}(p,q,r,s)^{abcd}_{jk} = -\delta_{jk}\frac{g^2}{2M}(T^cT^d)^{ab}\cos\left(\frac{p_j+q_j}{2}\right)\left[1 - \frac{1}{2M}\sum_j \widehat{p}_j^2\right]. \tag{B.21}$$

B.3 Quenched lattice QCD in background field gauge

I discuss background field gauge in more detail in Section 3.4.2. In this section I derive the Feynman rules. The complete quenched lattice QCD action is

$$S^{\mathrm{BF}}[B,q,\bar{c},c] = S^{\mathrm{BF}}_{\mathrm{W}}[U] + S^{\mathrm{BF}}_{\mathrm{GF}}[B,q] + S^{\mathrm{BF}}_{\mathrm{FP}}[B,q,\bar{c},c], \qquad (B.22)$$

where $S_{\mathrm{W}}^{\mathrm{BF}}$ is given in Equation (3.47), $S_{\mathrm{GF}}^{\mathrm{BF}}$ in Equation (3.48) and $S_{\mathrm{FP}}^{\mathrm{BF}}$ in Equation (3.49).

In the continuum limit we can expand the action in terms of the four fields, B, q, $\bar{c}$ and c. The Wilson term becomes

$$
\begin{aligned}
S_{\mathrm{W}} = & \frac{1}{g_0^2} \mathrm{Tr} \sum_x \sum_{\mu,\nu} \mathrm{Re} \Big(\Delta_\mu^+ (B + g_0 q)_\nu - \Delta_\nu^+ (B + g_0 q)_\mu \\
& + [(B + g_0 q)_\mu, (B + g_0 q)_\nu] \Big)^2,
\end{aligned}
\tag{B.23}
$$

whilst the gauge fixing term is

$$
\begin{aligned}
S_{\mathrm{GF}} = -\lambda_0 \mathrm{Tr} \sum_x & \left(q_\mu(x) - e^{-B_\mu(x-a\hat{\mu})} q_\mu(x - a\hat{\mu}) e^{B_\mu(x-a\hat{\mu})} \right) \\
& \times \left(q_\nu(x) - e^{-B_\nu(x-a\hat{\nu})} q_\nu(x - a\hat{\nu}) e^{B_\nu(x-a\hat{\nu})} \right)
\end{aligned}
\tag{B.24}
$$

and the Faddeev-Popov ghost term becomes

$$
\begin{aligned}
S_{\mathrm{FP}} = & -2\mathrm{Tr} \sum_x \left(e^{B_\mu(x)} \bar{c}(x + a\hat{\mu}) e^{-B_\mu(x)} - \bar{c}(x) \right) \Big[g_0 \mathrm{Ad}[q_\mu(x)] c(x) \\
& + \left(e^{B_\mu(x)} c(x + a\hat{\mu}) e^{-B_\mu(x)} - c(x) \right) \Big] \left(1 + \frac{1}{2} g_0 \mathrm{Ad}[q_\mu(x)] - \frac{1}{6} g_0^2 (\mathrm{Ad}[q_\mu(x)])^2 \right).
\end{aligned}
\tag{B.25}
$$

B.3.1   Two-point vertices

There are four relevant two-point vertices: the inverse quantum and ghost field propagators and two vertices with background field external legs. The fifth two-point vertex is the measure term, which will not be discussed here. The measure term is derived in, for example, [115].

The $V^{(0,0,2,0)}(p,-p)^{ab}_{\mu\nu}$ vertex

The contributing second order terms in the Wilson and gauge fixing parts of the action are

$$S^{(0,0,2,0)} = -\frac{\delta^{ab}}{2}\mathrm{Tr}\sum_x 2\left(\Delta^+_\mu q_\nu\Delta^+_\mu q_\nu + (\lambda_0-1)\Delta^+_\nu q_\mu\Delta^+_\mu q_\nu\right). \qquad \text{(B.26)}$$

We expand Equation (B.26) to first order in the coupling constant g_0 and use the Fourier series representation of the fields to give

$$S^{(0,0,2,0)}_{\mathrm{W},1} = -\delta^{ab}\int\frac{\mathrm{d}^4 p}{(2\pi)^4}\frac{\mathrm{d}^4 q}{(2\pi)^4}\delta(p+q)\widetilde{q}^a_\mu(p)\widetilde{q}^b_\nu(q)\left(\delta_{\mu\nu}\widehat{p}^2 + (\lambda_0-1)\widehat{p}_\mu\widehat{p}_\nu\right). \tag{B.27}$$

The corresponding Feynman rule is

$$V^{(0,0,2,0)}(p,-p)^{ab}_{\mu\nu} = \delta^{ab}\left(P_{\mu\nu}(p) + \lambda_0\widehat{p}_\mu\widehat{p}_\nu\right), \qquad \text{(B.28)}$$

where

$$P_{\mu\nu} = \delta_{\mu\nu}\widehat{p}^2 - \widehat{p}_\mu\widehat{p}_\nu. \qquad \text{(B.29)}$$

The derivation of the two–point vertices involving background gluons both follow exactly the calculation for the inverse gluon propagator, without the contribution from the gauge–fixing term. The results are

$$V^{(2,0,0)}(p,-p)^{ab}_{\mu\nu} = g_0^{-2}\delta^{ab}P_{\mu\nu}(p) \qquad \text{(B.30)}$$

and

$$V^{(1,1,0)}(p,-p)^{ab}_{\mu\nu} = g_0^{-1}\delta^{ab}P_{\mu\nu}(p). \qquad \text{(B.31)}$$

B.3.2 Three-point vertices

The $V^{(0,1,2,0)}(p,q,r)^{abc}_{\mu\nu\rho}$ vertex

The contributing term from the gauge fixing action is

$$
S^{(0,1,2,0)}_{\mathrm{GF}} = -2\lambda_0 \mathrm{Tr} \sum_x \left(q_\mu(x) - e^{-B_\mu(x-a\hat\mu)} q_\mu(x-a\hat\mu) e^{B_\mu(x-a\hat\mu)} \right)
$$
$$
\times \left[B_\nu(x-a\hat\nu), q_\nu(x-a\hat\nu) \right]. \tag{B.32}
$$

For the purposes of updating the HiPPy /HPsRc routines to include the background field gauge, we need only consider the gauge fixing terms arising from $S^{(0,1,2,0)}_{\mathrm{GF}}$. The gauge fixing terms are hardwired into the HPsRc code, whereas the other contributions are generated from the python vertex files.

The colour structure of the gauge fixing term is

$$
C^{(0,1,2,0)} = \mathrm{Tr}\left\{ T^b[T^a, T^c] \right\} = \mathrm{Tr}\left\{ f^{acd} T^b T^d \right\} = -\frac{1}{2} f^{abc}. \tag{B.33}
$$

The gauge fixing term is, after permuting the indices,

$$
S^{(0,1,2,0)}_{\mathrm{GF}} = \lambda_0 f^{abc} \int \frac{\mathrm{d}^4 p}{(2\pi)^4} \frac{\mathrm{d}^4 q}{(2\pi)^4} \frac{\mathrm{d}^4 r}{(2\pi)^4} \Big[\delta_{\mu\rho} \left(1 - e^{-iq_\nu} \right) e^{iq_\nu/2} e^{-ir_\rho/2}
$$
$$
- \delta_{\mu\nu} \left(1 - e^{-ir_\rho} \right) e^{-iq_\nu/2} e^{ir_\rho/2} \Big] e^{-ip_\mu/2} \delta(p+q+r) \widetilde{B_\mu}^a(p) \widetilde{q_\nu}^b(q) \widetilde{q_\rho}^c(r)
$$
$$
= i\lambda_0 f^{abc} \int \frac{\mathrm{d}^4 p}{(2\pi)^4} \frac{\mathrm{d}^4 q}{(2\pi)^4} \frac{\mathrm{d}^4 r}{(2\pi)^4} \delta(p+q+r) \widetilde{B_\mu}^a(p) \widetilde{q_\nu}^b(q) \widetilde{q_\rho}^c(r)
$$
$$
\times \left[e^{iq_\mu/2} \widehat{q}_\nu - e^{iq_\nu/2} \widehat{r}_\rho \right] \tag{B.34}
$$

implying an associated Feynman rule

$$
V^{(0,1,2,0)}_{\mathrm{GF}}(p,q,r)^{abc}_{\mu\nu\rho} = i\lambda_0 f^{abc} \left(\delta_{\mu\rho} \widehat{q}_\nu e^{iq_\mu/2} - \delta_{\mu\nu} \widehat{r}_\rho e^{ir_\mu/2} \right). \tag{B.35}
$$

This Feynman rule differs from equation [A.11] in [78] by a minus sign in the exponential factors. The Feynman rules for background field gauge have been independently checked by Tom Hammant. The analytical expressions have been implemented in the HPsRc code, which has been used in several

calculations and provides a further cross-check of these Feynman rules. I therefore believe this discrepancy is an error in [78].

The $V^{(0,1,0,1)}(p,q,r)^{abc}_\mu$ vertex

The background field ghost three–point interaction is induced via two terms in S_{FP}

$$S^{(0,1,0,1)} = -2\sum_x \mathrm{Tr}\left\{[B_\mu(x),\bar{c}(x+a\hat{\mu})]\Delta^+_\mu c(x) + \Delta^+_\mu\bar{c}(x)[B_\mu(x),c(x+a\hat{\mu})]\right\}$$

(B.36)

The colour factor of the first term is $f^{abc}/2$. For the second term the colour factor is $-f^{abc}/2$. So in momentum space $S^{(0,1,0,1)}$ is

$$\begin{aligned}
S^{(0,1,0,1)} &= -f^{abc}\int\frac{\mathrm{d}^4p}{(2\pi)^4}\frac{\mathrm{d}^4q}{(2\pi)^4}\frac{\mathrm{d}^4r}{(2\pi)^4}\left[e^{ir_\mu}\left(e^{iq_\mu}-1\right)-e^{iq_\mu}\left(e^{ir_\mu}-1\right)\right]\\
&\quad\times e^{-i(q+r)_\mu/2}\widetilde{B}^a_\mu(-q-r)\widetilde{c}^b(q)\widetilde{\widetilde{c}}^c(r)\\
&= -f^{abc}\int\frac{\mathrm{d}^4p}{(2\pi)^4}\frac{\mathrm{d}^4q}{(2\pi)^4}\frac{\mathrm{d}^4r}{(2\pi)^4}\delta(p+q+r)\widetilde{B}^a_\mu(p)\widetilde{c}^b(q)\widetilde{\widetilde{c}}^c(r)i\widehat{(q-r)}_\mu.
\end{aligned}$$

(B.37)

Hence the Feynman rule associated with this vertex is

$$V^{(0,1,0,1)}(p,q,r)^{abc}_\mu = -if^{abc}\widehat{(q-r)}_\mu,$$

(B.38)

in agreement with equation [A.12] in [78].

The $V^{(0,0,1,1)}(p,q,r)^{abc}_\mu$ vertex

This three-point vertex arises from two terms in S_{FP} in equation (B.25):

$$S^{(0,0,1,1)} = -2g_0\sum_x \mathrm{Tr}\left\{\frac{1}{2}\Delta^+_\mu\bar{c}(x)\mathrm{Ad}[q_\mu(x)]\Delta^+_\mu c(x) + \Delta^+_\mu\bar{c}(x)\mathrm{Ad}[q_\mu(x)]c(x)\right\}.$$

(B.39)

The colour factor for these terms is

$$\mathrm{Tr}\left\{\bar{c}\,\mathrm{Ad}[q_\mu]c\right\} = \mathrm{Tr}\left\{\bar{c}^a T^a(\mathrm{Ad}[q_\mu]c)^d T^d\right\} = \frac{f^{abc}}{2}q^a_\mu\bar{c}^b c^c,$$

(B.40)

where I have used the property $(\text{Ad}[X] \cdot Y)^a = f^{abc} X^b Y^c$.

Expanding equation (B.39) in momentum space gives

$$
\begin{aligned}
S^{(0,0,1,1)} = &- g_0 f^{abc} \sum_x \int \frac{\mathrm{d}^4 p}{(2\pi)^4} \frac{\mathrm{d}^4 q}{(2\pi)^4} \frac{\mathrm{d}^4 r}{(2\pi)^4} \left(e^{iq_\mu} - 1 \right) e^{iqx} e^{ip(x+\hat{\mu}/2)} \\
&\times \left[\frac{1}{2} \left(e^{ir_\mu} - 1 \right) + 1 \right] e^{irx} \widetilde{q}_\mu^a(p) \widetilde{c}^b(q) \widetilde{\overline{c}}\,(r) \\
= &- g_0 f^{abc} \int \frac{\mathrm{d}^4 p}{(2\pi)^4} \frac{\mathrm{d}^4 q}{(2\pi)^4} \frac{\mathrm{d}^4 r}{(2\pi)^4} \delta(p+q+r) \widetilde{q}_\mu^a(p) \widetilde{c}^c(q) \widetilde{\overline{c}}\,(r) \\
&\times i\hat{q}_\mu \frac{1}{2} \left(e^{ir_\mu/2} + e^{-ir_\mu/2} \right).
\end{aligned}
\tag{B.41}
$$

The Feynman rule is therefore

$$
V^{(0,0,1,1)}(p, q, r)_\mu^{abc} = -ig_0 f^{abc} \hat{q}_\mu \cos\left(\frac{r_\mu}{2} \right).
\tag{B.42}
$$

This Feynman rule disagrees with [A.8] of [78]. Using calculations performed with HPSRC , and comparing the analytic expression with that derived independently by Tom Hammant, I believe there is an error in the expression of [78].

B.3.3 Four-point vertices

The four-point vertices are not listed in [78].

Unpicking the structure of the double commutator terms (those of the form $[X, Y][Z, W]$), the associated colour factor is

$$
C_A^{(4)} = \text{Tr}(T^a T^c - T^c T^a)(T^b T^d - T^d T^b) = -\frac{1}{2} f^{ace} f^{ebd}.
\tag{B.43}
$$

The other contributions to the four-point vertices have the general structure $(\{XY, Z\} - 2XZY)W$ or $W(\{XY, Z\} - 2XZY)$, and have colour factors given by

$$
C_B^{(4)} = \text{Tr}(T^a T^b T^c T^d + T^a T^b T^d T^c - 2T^a T^c T^b T^d),
\tag{B.44}
$$

using the cyclic properties of the trace. However, since we are free to exchange

the colour indices a and b on the background field legs, we have

$$C_A^{(4)} = -C_B^{(4)} \equiv C^{(4)}. \tag{B.45}$$

The $V^{(0,2,0,1)}(p,q,r,s)_{\mu\nu}^{abcd}$ vertex

The interaction of two background fields with a ghost anti–ghost pair is generated by three terms in S_{FP}.

These contributions have Fourier decomposition

$$S^{(0,2,0,1)} = -2C^{(4)} \int \frac{\mathrm{d}^4 p}{(2\pi)^4} \cdots \frac{\mathrm{d}^4 s}{(2\pi)^4} \delta(p + q + r + s) \widetilde{B}_\mu^a(p) \widetilde{B}_\nu^b(q) \widetilde{c}^c(r) \widetilde{\bar{c}}^d(s)$$
$$\times \cos((r+s)_\mu/2). \tag{B.46}$$

Hence the corresponding Feynman rule is

$$V^{(0,2,0,1)}(p,q,r,s)_{\mu\nu}^{abcd} = -2\delta_{\mu\nu} C^{(4)} \cos\left(\frac{(r-s)_\mu}{2}\right). \tag{B.47}$$

The $V^{(0,0,2,1)}(p,q,r,s)_{\mu\nu}^{abcd}$ vertex

The interaction of two quantum fields with a ghost anti–ghost pair is generated by a single term in S_{FP}:

$$S^{(0,0,2,1)} = 2\sum_x \mathrm{Tr}\left\{-\frac{1}{12}g_0^2 \Delta_\mu^+ \bar{c}(x)(\mathrm{Ad}[q_\mu(x)])^2 \Delta_\mu^+ c(x)\right\}. \tag{B.48}$$

The colour factor is given by

$$\mathrm{Tr}\left\{\bar{c}^c T^c \mathrm{Ad}[q_\mu](\mathrm{Ad}[q_\mu]c)^e T^e\right\} = f^{bde} \mathrm{Tr}\left\{T^c T^f (\mathrm{Ad}[q_\mu])^{ef}\right\} q_\mu^b c^c \bar{c}^d$$
$$= \frac{1}{2} f^{bde} f^{eca} q_\mu^a q_\mu^b c^c \bar{c}^d = C^{(4)} q_\mu^a q_\mu^b c^c \bar{c}^d. \tag{B.49}$$

Therefore the momentum expansion of $S^{(0,0,2,1)}$ is

$$S^{(0,0,2,1)} = \frac{C^{(4)}}{6} \int \frac{\mathrm{d}^4 q}{(2\pi)^4} \cdots \frac{\mathrm{d}^4 s}{(2\pi)^4} \delta(p+q+r+s) \widetilde{q}_\mu^a(p) \widetilde{q}_\mu^b(q) \widetilde{c}^c(r) \widetilde{c}\,(s) \widehat{r}_\mu \widehat{s}_\mu.$$

(B.50)

Hence the corresponding Feynman rule for the complete vertex is

$$V^{(0,0,2,1)}(p,q,r,s)_{\mu\nu}^{abcd} = \frac{1}{6} g_0^2 C^{(4)} \delta_{\mu\nu} \widehat{r}_\mu \widehat{s}_\nu.$$

(B.51)

The $V^{(0,2,2,0)}(p,q,r,s)_{\mu\nu\rho\sigma}^{abcd}$ vertex

The interaction of two background and two quantum gluons arises from the fourth order terms in the gauge fixing action.

The first relevant term from the gauge fixing action is

$$S_{\mathrm{GF},A}^{(0,2,2,0)} = -\lambda_0 C^{(4)} \sum_x \delta_{\mu\rho} \delta_{\nu\sigma} B_\mu^a(x-a\hat{\mu}) B_\nu^b(x-a\hat{\nu}) q_\rho^c(x-a\hat{\rho}) q_\sigma^d(x-a\hat{\sigma}),$$

(B.52)

with corresponding Feynman rule

$$V_{\mathrm{GF},A}^{(0,2,2,0)}(p,q,r,s)_{\mu\nu\rho\sigma}^{abcd} = -\lambda_0 C^{(4)} \delta_{\mu\rho} \delta_{\nu\sigma} e^{-i(q+s)_\nu/2} e^{i(q+s)_\mu/2}.$$

(B.53)

The Fourier series representation of the other gauge fixing contributions is

$$\begin{aligned}
S_{\mathrm{GF},B}^{(0,2,2,0)} &= \lambda_0 C^{(4)} \int \frac{\mathrm{d}^4 p}{(2\pi)^4} \cdots \frac{\mathrm{d}^4 s}{(2\pi)^4} \Big(\delta_{\mu\sigma} \delta_{\nu\sigma} \left(1 - e^{-ir_\rho}\right) e^{ir_\rho/2} e^{-is_\sigma/2} \\
&\quad + \delta_{\mu\rho} \delta_{\nu\rho} e^{-ir_\rho/2} \left(1 - e^{-is_\sigma}\right) e^{is_\sigma/2} \Big) e^{-ip_\mu/2} e^{-iq_\nu/2} \\
&\quad \times \delta(p+q+r+s) \widetilde{B}_\mu^a(p) \widetilde{B}_\mu^b(q) \widetilde{q}_\rho^c(r) \widetilde{q}_\sigma^d(s) \\
&= i\lambda_0 C^{(4)} \int \frac{\mathrm{d}^4 p}{(2\pi)^4} \cdots \frac{\mathrm{d}^4 s}{(2\pi)^4} \delta(p+q+r+s) \widetilde{B}_\mu^a(p) \widetilde{B}_\nu^b(q) \widetilde{q}_\rho^c(r) \widetilde{q}_\sigma^d(s) \\
&\quad \times \left(e^{ir_\sigma/2} \widehat{r}_\rho + e^{is_\rho/2} \widehat{s}_\sigma \right),
\end{aligned}$$

(B.54)

with associated Feynman rule

$$V_{\mathrm{GF},B}^{(0,2,2,0)}(p,q,r,s)_{\mu\nu\rho\sigma}^{abcd} = -i\lambda_0 C^{(4)}\left(\delta_{\mu\sigma}\delta_{\nu\sigma}e^{ir_\sigma/2}\widehat{r}_\rho + \delta_{\mu\rho}\delta_{\nu\rho}e^{is_\rho/2}\widehat{s}_\sigma\right) \quad \text{(B.55)}$$

Finally, then, the overall Feynman rule is

$$\begin{aligned}
V_{\mathrm{GF}}^{(0,2,2,0)}(p,q,r,s)_{\mu\nu\rho\sigma}^{abcd} = -\lambda_0 C^{(4)}\bigg[&\delta_{\mu\rho}\delta_{\nu\sigma}e^{-i(q+s)_\nu/2}e^{i(q+s)_\mu/2} \\
&+ i\left(\delta_{\mu\sigma}\delta_{\nu\sigma}e^{ir_\sigma/2}\widehat{r}_\rho + \delta_{\mu\rho}\delta_{\nu\rho}e^{is_\rho/2}\widehat{s}_\sigma\right)\bigg]. \quad \text{(B.56)}
\end{aligned}$$

B.4   Current insertions

In this section I derive the Feynman rules associated with the heavy-light current operators, $J_\mu^{(i)}$ [89, 112, 113]. There are three NRQCD operators, given in Equation (6.52). In the following, all momenta are incoming and the current insertion is $\Gamma_\mu = \widehat{\gamma}_\mu$ for the vector current and $\Gamma_\mu = \widehat{\gamma}_5\widehat{\gamma}_\mu$ for the axial-vector current.

Feynman rules for $J_\mu^{(0)}$

The Feynman rule associated with $J_\mu^{(0)}$ is simply Γ_μ.

Feynman rules for $J_\mu^{(1)}$

The Feynman rules for the $J_\mu^{(1)}$ current are slightly more involved. The tree-level Feynman rule, corresponding to a vertex insertion, is given by the leading order contribution to $\nabla Q(x)$ in the strong coupling expansion of the link variable. The Fourier series representation is

$$\begin{aligned}
J_\mu^{(1),\mathrm{tree}} &= \left(-\frac{1}{2aM}\right)\sum_{p,p'}\widetilde{q}(p')e^{ip'x}\Gamma_\mu\sum_j\widehat{\gamma}_j\nabla_j e^{ipx}\widetilde{Q}(p) \\
&= -\frac{1}{2aM}\sum_{p,p'}\widetilde{q}(p')e^{ip'x}\Gamma_\mu\sum_{j=1}^{3}\widehat{\gamma}_j\left(i\sin p_j\right)e^{ipx}\widetilde{Q}(p). \quad \text{(B.57)}
\end{aligned}$$

Therefore the associated Feynman rule is

$$J_\mu^{(1),\text{tree}} = -\frac{i}{2aM}\Gamma_\mu \sum_{j=1}^{3}\widehat{\gamma}_j \sin p_j. \tag{B.58}$$

The one-loop vertex insertion is given by the $\mathcal{O}(g^2)$ contributions to $\nabla Q(x)$. In this case we have

$$
\begin{aligned}
J_\mu^{(1),g^2} &= \left(-\frac{1}{2aM}\right)\left(-ig^2\right)T^a \sum_{p,p',k}\widetilde{q}(p')\widetilde{A}^a(k)e^{ip'x}\Gamma_\mu \\
&\quad \times \sum_{j=1}^{3}\widehat{\gamma}_j\frac{1}{2}\left(e^{ik(x+\hat{j}/2)}e^{ip(x+\hat{j})} + e^{ik(x-\hat{j}/2)}e^{ip(x-\hat{j})}\right)\widetilde{Q}(p) \\
&= \frac{ig^2}{2aM}T^a \sum_{p,p',k}\widetilde{q}(p')\widetilde{A}^a(k)e^{i(p'+p+k)x}\Gamma_\mu \sum_{j=1}^{3}\widehat{\gamma}_j\cos\left(p+k/2\right)_j\widetilde{Q}(p).
\end{aligned} \tag{B.59}
$$

The plus sign in the parenthesis on the second line (and hence the cosine) arise because the gauge fields are anti-Hermitian and so $-A^\dagger = +A$. The corresponding Feynman rule is

$$J_\mu^{(1),g^2} = \frac{ig^2}{2aM}T^a\Gamma_\mu \sum_{j=1}^{3}\widehat{\gamma}_j\cos\left(p+k/2\right)_j. \tag{B.60}$$

The two-gluon vertex insertion is

$$
\begin{aligned}
J_\mu^{(1),g^4} &= \left(-\frac{1}{2aM}\right)\frac{(-ig^2)^2}{2}\{T^a,T^b\} \sum_{p,p',k,k'}\widetilde{q}(p')\widetilde{A}^a(k)\widetilde{A}^b(k')e^{ip'x}\Gamma_\mu \\
&\quad \times \sum_{j=1}^{3}\widehat{\gamma}_j\frac{1}{2}\left(e^{ik(x+\hat{j}/2)}e^{ik'(x+\hat{j}/2)}e^{ip(x+\hat{j})} - e^{ik(x-\hat{j}/2)}e^{ik'(x-\hat{j}/2)}e^{ip(x-\hat{j})}\right)\widetilde{Q}(p) \\
&= -\frac{g^4}{4aM}\{T^a,T^b\} \sum_{p,p',k,k'}\widetilde{q}(p')\widetilde{A}^a(k)\widetilde{A}^b(k')e^{i(p'+p+k'+k)x}\Gamma_\mu \\
&\quad \times \sum_{j=1}^{3}\widehat{\gamma}_j\sin\left(p+k/2+k'/2\right)_j\widetilde{Q}(p).
\end{aligned} \tag{B.61}
$$

In this case, the minus sign in the second line occurs because $-(A^\dagger)^2 = -A^2$. Finally, then, we have the Feynman rule

$$J_\mu^{(1),g^4} = -\frac{g^4}{4aM}\{T^a, T^b\}\Gamma_\mu \sum_{j=1}^{3} \widehat{\gamma}_j \sin{(p + k/2 + k'/2)}_j \, . \qquad \text{(B.62)}$$

Appendix C

Gluon selfenergy

In continuum QCD four diagrams contribute to the gluon selfenergy at one-loop. These diagrams, which comprise the fermionic bubble diagram, two gluon diagrams (the bubble and the tadpole) and a single ghost contribution, are shown in Figure C.1. The Ward identity, which is ultimately an expression
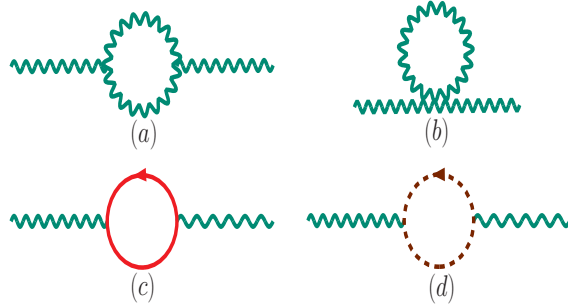

Figure C.1: Contributions to the gluon selfenergy in continuum QCD. From top left, the diagrams are (a) the gluon bubble, (b) the gluon tadpole, (c) the light quark bubble and (d) the ghost bubble. Green wiggly lines indicate gluons, red solid lines represent light quarks and brown dotted lines are ghosts.

of gauge invariance, takes the form

$$q^\mu \Pi_{\mu\nu}(q^2) = 0 \qquad (C.1)$$

and guarantees that the selfenergy, $\Pi_{\mu\nu}(q^2)$, must be transverse in the external momenta q_μ. The selfenergy must therefore have the Lorentz structure

$$\Pi_{\mu\nu}(q^2) = i(q^2 g_{\mu\nu} - q_\mu q_\nu)\Pi(q^2), \qquad (C.2)$$

where $\Pi(q^2)$ is a regular function of q^2 at $q^2 = 0$ (see, for example, [116]) and I have neglected colour indices for clarity. Thus the only divergences present in the selfenergy are ultraviolet logarithmic divergences.

For lattice QCD, the situation is complicated by the presence of three extra diagrams, the fermion and ghost tadpoles and the measure term, which I illustrate in Figure C.2. Without the extra diagrams, the selfenergy is not gauge invariant and therefore the Ward identity does not hold. Computing all seven lattice diagrams to ensure the selfenergy obeys the relevant Ward identity is a nontrivial check of the HPSRC and HIPPY code.
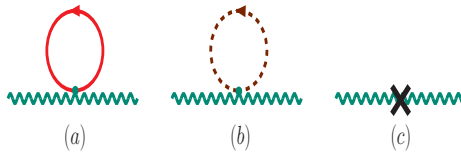

(a) (b) (c)

Figure C.2: Additional lattice QCD contributions to the gluon selfenergy. From left, the diagrams are (a0 the light quark tadpole, (b) the ghost tadpole and (c) the measure term. Green wiggly lines are gluons, red solid lines are light quarks and brown dotted lines are ghosts. The black cross represents the measure insertion.

The two fermionic contributions to the gauge boson selfenergy satisfy the Ward identity independently of the remaining gluon, ghost and counterterm diagrams, which I collectively call the quenched contributions. The fermion diagrams are exactly those that contribute to the heavy quark selfenergy, discussed in Chapter 5, and checking the validity of the Ward identity therefore serves as one cross-check of the code used in the heavy quark selfenergy calculation.

In this appendix I confirm that the fermionic contributions to the gluon selfenergy obey the Ward identity, Equation (C.1). This serves as an important check of the two-loop tadpole improvement factor and heavy quark selfenergy calculations in Chapters 4 and 5.

C.1 Fermionic contributions

I calculated the light quark contributions to the gluon selfenergy using HPSRC code based on a routine, `gluon_sigma`, written by Alistair Hart. This routine takes the momentum, Lorentz and colour indices of the external gluons as

arguments and evaluates one or more of the seven lattice contributions by exact modesummation according to a parameter list that specifies which diagrams to calculate. I adapted the routine to work with the heavy quark selfenergy code, discussed in Chapter 5, and implemented `VEGAS` evaluation of the integrands. I updated the code to use the `TaylUR` derived type to extract derivatives of the gluon selfenergy. I have also extended the routine so that it is compatible with our implementation of background field gauge.

For the gluon selfenergy to satisfy the Ward identity, the light quark bubble diagram – diagram (c) in Figure C.1 – must depend on the external momentum in such a way that the overall contribution vanishes as the momentum tends to zero. I find that this is indeed the case, as I illustrate in Figure C.3 for unimproved staggered light quarks and in Figure C.4 for ASQTad light quarks.

In Tables C.1 and C.2 I show results for unimproved staggered quarks and ASQTad quarks respectively I use three different light quark masses, $m_q = 0.05$ and $m_q = 0.3$. I obtained the results for the bubble diagrams using six cores with 5×10^7 function evaluations and 15 iterations, taking approximately 1.5 hours each for the unimproved staggered quarks. The ASQTad computations took approximately 35 minutes on 32 processors. For the tadpole diagrams I used six cores with 10^5 function evaluations and 15 iterations, taking approximately two minutes for unimproved staggered quarks and seven minutes for ASQTad quarks.

I found that, as expected, the light quark tadpole contribution is independent of the external momenta. Tests of the Ward identity for the quenched contributions are currently underway.
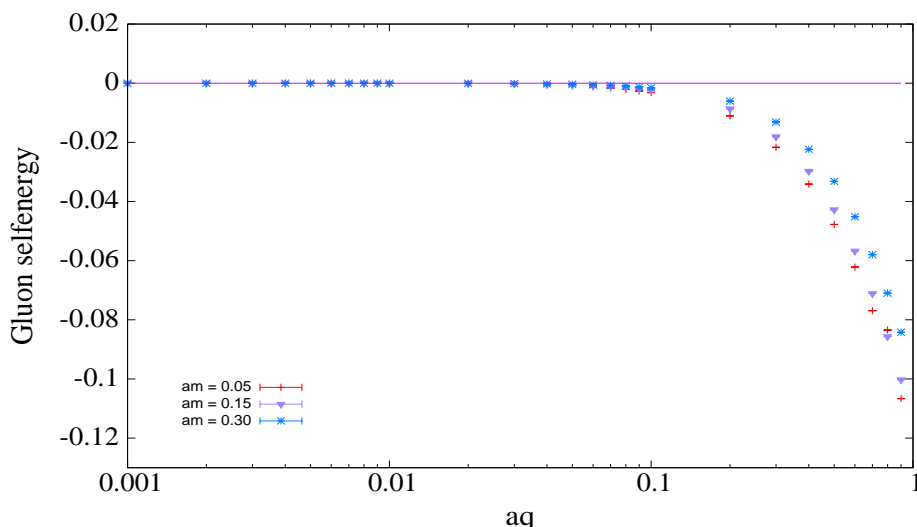
Figure C.3: Light quark bubble and rainbow contributions to the gluon self-energy using unimproved staggered quarks. I plot three light quark masses: $am_q = 0.05$ with red crosses, $am_q = 0.15$ with purple triangles and $am_q = 0.30$ with blue stars. The horizontal line indicates vanishing self-energy. Uncertainties are smaller than the data points shown.

Figure C.4: Light quark bubble and rainbow contributions to the gluon selfenergy using ASQTad light quarks. I plot three light quark masses: $am_q = 0.05$ with red crosses, $am_q = 0.15$ with purple triangles and $am_q = 0.30$ with blue stars. The horizontal line indicates vanishing selfenergy. Uncertainties are smaller than the data points shown.
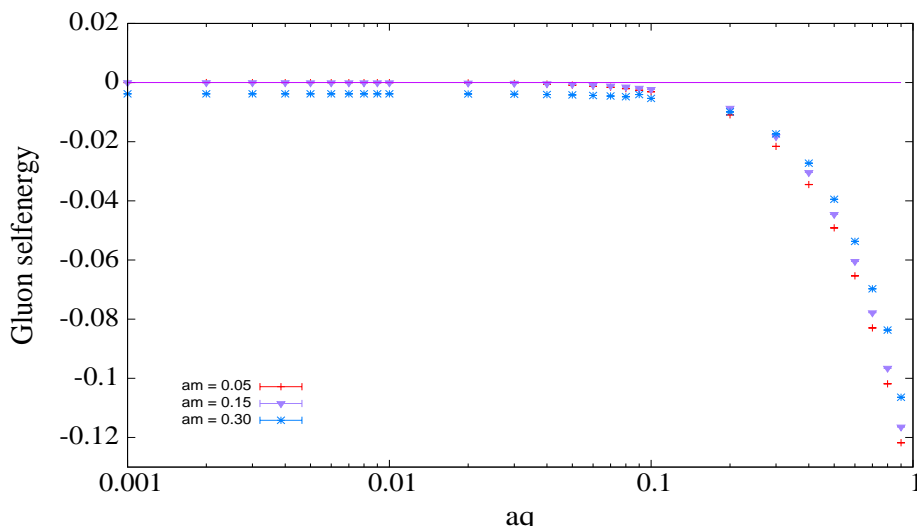
175

	am_q		
aq	0.05	0.15	0.3
0.001	-0.00002(1)	0.000000(7)	0.000014(3)
0.002	-0.00002(1)	0.000000(7)	0.000015(3)
0.003	-0.00002(1)	0.000000(7)	0.000011(3)
0.004	-0.00002(1)	0.000000(7)	0.000011(3)
0.005	-0.00002(1)	-0.000003(7)	0.000010(3)
0.006	-0.00003(1)	-0.000007(7)	0.000007(3)
0.007	-0.00003(1)	-0.000010(7)	0.000005(3)
0.008	-0.00003(1)	-0.000013(7)	0.000005(3)
0.009	-0.00003(1)	-0.000017(7)	0.000001(3)
0.01	-0.00003(1)	-0.000023(7)	0.000001(3)
0.02	-0.00013(1)	-0.000092(7)	-0.000050(3)
0.03	-0.00029(1)	-0.000207(7)	-0.000126(3)
0.04	-0.00054(1)	-0.000369(7)	-0.000233(3)
0.05	-0.00084(1)	-0.000577(7)	-0.000373(3)
0.06	-0.00121(1)	-0.000830(7)	-0.000546(3)
0.07	-0.00163(1)	-0.001130(7)	-0.000744(3)
0.08	-0.00209(4)	-0.001467(7)	-0.000979(3)
0.09	-0.00264(4)	-0.001849(7)	-0.001243(3)
0.1	-0.00318(4)	-0.002277(7)	-0.001533(3)
0.2	-0.01102(4)	-0.008643(7)	-0.006039(3)
0.3	-0.02166(4)	-0.018108(7)	-0.013146(3)
0.4	-0.03410(4)	-0.029730(7)	-0.022360(3)
0.5	-0.04775(4)	-0.042770(7)	-0.033195(3)
0.6	-0.06216(4)	-0.056687(7)	-0.045159(3)
0.7	-0.07691(4)	-0.071087(7)	-0.057954(3)
0.8	-0.08344(4)	-0.085673(7)	-0.070962(3)
0.9	-0.10664(4)	-0.100220(7)	-0.084218(3)

Table C.1: Light quark bubble and tadpole diagram results for the gluon selfenergy at three different light quark mass. The uncertainties quoted are the errors from both bubble and tadpole contributions added in quadrature. All results use unimproved staggered light quarks.

aq	am_q		
	0.05	0.15	0.3
0.001	-0.00001(3)	-0.000015(3)	-0.003794(3)
0.002	-0.00001(3)	-0.000015(3)	-0.003795(3)
0.003	-0.00002(3)	-0.000015(3)	-0.003795(3)
0.004	-0.00002(3)	-0.000015(3)	-0.003795(3)
0.005	-0.00002(3)	-0.000019(3)	-0.003798(3)
0.006	-0.00002(3)	-0.000020(3)	-0.003798(3)
0.007	-0.00002(3)	-0.000024(3)	-0.003803(3)
0.008	-0.00002(3)	-0.000028(3)	-0.003804(3)
0.009	-0.00003(3)	-0.000034(3)	-0.003810(3)
0.01	-0.00004(3)	-0.000037(3)	-0.003811(3)
0.02	-0.00013(3)	-0.000106(3)	-0.003858(3)
0.03	-0.00029(3)	-0.000219(3)	-0.003934(3)
0.04	-0.00054(3)	-0.000379(3)	-0.004044(3)
0.05	-0.00084(3)	-0.000582(3)	-0.004184(3)
0.06	-0.00117(3)	-0.000832(3)	-0.004358(3)
0.07	-0.00159(3)	-0.001129(3)	-0.004558(3)
0.08	-0.00205(3)	-0.001465(3)	-0.004789(3)
0.09	-0.00260(3)	-0.001849(3)	-0.004053(3)
0.1	-0.00310(4)	-0.002269(3)	-0.005351(3)
0.2	-0.01089(3)	-0.008626(3)	-0.009938(3)
0.3	-0.02157(3)	-0.018249(3)	-0.017338(3)
0.4	-0.03447(3)	-0.030370(3)	-0.027269(3)
0.5	-0.04913(3)	-0.044553(3)	-0.039467(3)
0.6	-0.06535(3)	-0.060431(3)	-0.053682(3)
0.7	-0.08294(3)	-0.077813(3)	-0.069716(3)
0.8	-0.10183(3)	-0.096532(3)	-0.083690(3)
0.9	-0.12177(3)	-0.116410(3)	-0.106410(3)

Table C.2: Light quark bubble and tadpole diagram results for the gluon selfenergy at three different light quark mass. The uncertainties quoted are the errors from both bubble and tadpole contributions added in quadrature. All results use ASQTad light quarks.

Appendix D

Kinetic renormalisation parameters

D.1 Kinetic renormalisation parameters

In Chapter 4 I discuss the calculation of the renormalisation coefficients for a simple NRQCD action - the Davies and Thacker action. In this appendix I outline the derivation of the correction coefficients for the minimally-improved NRQCD action given by

$$\widetilde{S}^0_{\mathrm{NRQCD}} = a^3 \sum_x \psi^\dagger(\mathbf{x}, t) \left(\Delta_4^+ - \frac{\widetilde{\Delta}^{(2)}}{2aM} \right) \psi(\mathbf{x}, t) \tag{D.1}$$

where I define $\widetilde{\Delta}^{(2)}$ in Appendix A.

The quark propagator now takes the form

$$\widetilde{G}_0^{-1}(w, \mathbf{p}) = e^{-aw} - 1 + \frac{4}{2aM} \sum_j \left(\sin^2 \left(\frac{ap_j}{2} \right) + \frac{1}{3} \sin^4 \left(\frac{ap_j}{2} \right) \right) \tag{D.2}$$

and the tree-level pole lies at

$$a\widetilde{w}_T(\mathbf{p}) = \frac{a^2 \mathbf{p}^2}{2aM} + \mathcal{O}(a^6 p^6). \tag{D.3}$$

Note that there are no lattice artifacts at $\mathcal{O}(a^4 p^4)$, in contrast with the unimproved Davies and Thacker action.

Obtaining the renormalisation parameters for this action parallels the scheme set out in Chapter 4. However, in this case, the renormalised dispersion relation is

$$\widetilde{w}(\mathbf{p}) = \widetilde{w}_T(\mathbf{p}) - \alpha_s a(E_0 + \delta\widetilde{w}(\mathbf{p})) \tag{D.4}$$

are the correction terms are now

$$a\delta\widetilde{w}(\mathbf{p}) = \widetilde{W}_1 \frac{a^4(\mathbf{p}^2)^2}{8a^2M^2} + \widetilde{W}_2 a^4 p^4, \tag{D.5}$$

$$\widetilde{W}_1 = 2\left(\Sigma_0^{(2)} + \Sigma_1^{(1)}\right) + \Sigma_2^{(0)}, \tag{D.6}$$

$$\widetilde{W}_2 = \Sigma_3^{(0)}. \tag{D.7}$$

The exact expression for $\widetilde{W}_2$ differs from Equation (4.33): the improvement term has removed the $\Sigma_1^{(0)}$ contribution to W_2. Further improvement has no further effect on the mathematical expression for W_2. Equation (D.7) holds for even the highly-improved NRQCD action of Equation (2.66) [47].

D.1.1 Extension to p⁶

Future work may require calculating radiative corrections to $\mathcal{O}(a^6 p^6)$ kinetic operators. Here I give the expressions required for such a calculation. I expand the selfenergy to $\mathcal{O}(a^6 p^6)$ as

$$a\Sigma(w, \underline{p}) = \Sigma_0(w) + \Sigma_1(w)\frac{a^2 \underline{p}^2}{2aM} + \Sigma_2(w)\frac{a^4(\underline{p}^2)^2}{8a^2M^2} + \Sigma_3(w)a^4 p^4$$
$$+ \Sigma_4(w)\frac{a^6(p^2)^3}{48a^3M^3} + \Sigma_5(w)a^6(p^2)p^4 + \Sigma_6(w)a^6 p^6. \tag{D.8}$$

$\Sigma_5(w)$ and $\Sigma_6(w)$ are the coefficients of the new cubic symmetry breaking terms at $\mathcal{O}(a^6 p^6)$ and can be extracted using the following combinations of partial derivatives:

$$\Sigma_4(w) = a^3 M^3 \left.\frac{\partial^6(a\Sigma)}{\partial(ap_x)^2\partial(ap_y)^2\partial(ap_z)^2}\right|_{\mathbf{p}=0}, \tag{D.9}$$

$$\Sigma_5(w) = \frac{1}{48}\left(\frac{\partial^6(a\Sigma)}{\partial(ap_y)^2\partial(ap_z)^4} - 3\frac{\partial^6(a\Sigma)}{\partial(ap_x)^2\partial(ap_y)^2\partial(ap_z)^2}\right)_{\mathbf{p}=0}, \tag{D.10}$$

$$\Sigma_6(w) = \frac{1}{48}\left(\frac{\partial^6(a\Sigma)}{\partial(ap_z)^6} - \frac{\partial^6(a\Sigma)}{\partial(ap_y)^2\partial(ap_z)^4} - 143\frac{\partial^6(a\Sigma)}{\partial(ap_x)^2\partial(ap_y)^2\partial(ap_z)^2}\right)_{\mathbf{p}=0}. \tag{D.11}$$

The minimally-improved action of Equation (D.1) can be further improved to $\mathcal{O}(a^6 p^6)$ by replacing the Laplacian with an operator correct to $\mathcal{O}(a^6 p^6)$:

$$\overline{\Delta}^{(2)} = \Delta^{(2)} - \frac{a^2}{12}\Delta^{(2)} + \frac{a^4}{90}\sum_j \left[\Delta_j^+ \Delta_j^-\right]^3.$$ (D.12)

In this case I find the correction coefficients to be

$$W_3 = \Sigma_4^{(0)} + 3\Sigma_2^{(1)} + 6\left(\Sigma_0^{(3)} + \Sigma_1^{(2)}\right),$$ (D.13)

$$W_4 = \Sigma_5^{(0)} + \frac{\Sigma_3^{(1)}}{2aM},$$ (D.14)

$$W_5 = \Sigma_6^{(0)}.$$ (D.15)

Equation (D.15) holds for highly-improved NRQCD (Equation (2.66)), though the actual numerical value will clearly differ.

I do not give results for the $\mathcal{O}(a^6 p^6)$ kinetic coefficients. The computation is not tractable with the mix of analytic and numerical methods that I employ to calculate the radiative corrections for the Davies and Thacker action. Full automation in the future will be required if $\mathcal{O}(a^6 p^6)$ radiative corrections are desired.

Appendix E

HISQ renormalisation parameters

In this appendix I derive the mass and wavefunction renormalisation parameters for the HISQ action. My derivation largely follows [114].

E.1 Mass renormalisation

I write the inverse propagator as

$$G(p)^{-1} = G_0^{-1}(p) - \Sigma(p) \tag{E.1}$$

where

$$G_0^{-1}(p) = \sum_\mu i \sin(p_\mu) K_\mu(p)\gamma_\mu + m_0, \tag{E.2}$$

$$K_\mu(p) = 1 + \frac{1+\epsilon}{6} \sin^2(p_\mu), \tag{E.3}$$

$$\Sigma(p) = \sum_\mu i \sin(p_\mu) B_\mu(p)\gamma_\mu + C(p). \tag{E.4}$$

To calculate the pole mass, I set p = 0 and $p_0 = iE$, where E is the rest energy. Then the pole condition,

$$\sum_\mu \sin^2(p_\mu) (K_\mu - B_\mu)^2 + (m_0 - C)^2 = 0, \tag{E.5}$$

becomes

$$-\sinh^2 E \left(1 - \frac{1+\epsilon}{6} \sinh^2 E - B_0 \right)^2 + (m_0 - C)^2 = 0. \tag{E.6}$$

Taking the positive energy solution, and expanding the rest energy E and

the parameter ϵ as

$$E = m_{\text{tree}} + \alpha_s m_1 \tag{E.7}$$

$$\epsilon = \epsilon_{\text{tree}} + \alpha_s \epsilon_1, \tag{E.8}$$

the tree-level mass, m_{tree}, at fixed bare mass m_0, is given by

$$\sinh m_{\text{tree}} \left(1 - \frac{1 + \epsilon_{\text{tree}}}{6} \sinh^2 m_{\text{tree}} \right) = m_0. \tag{E.9}$$

The parameter ϵ_{tree} is fixed by requiring the mass to be equal to the kinetic mass, defined as

$$m_{\text{kin}}^{-1} = \left. \frac{\partial^2 E}{\partial p_z^2} \right|_{p_z = 0}, \tag{E.10}$$

for an onshell particle with momentum $p_\mu = (iE, 0, 0, p_z)$. The resulting solution is

$$\epsilon_{\text{tree}} = \left(4 - \sqrt{4 + \frac{12 m_{\text{tree}}}{\cosh m_{\text{tree}} \sinh m_{\text{tree}}}} \right) / \sinh^2 m_{\text{tree}} - 1. \tag{E.11}$$

We obtain the solution for m_{tree} by plugging in this expression for ϵ_{tree} into Equation (E.9) and solving iteratively.

Substituting the expansions in Equations (E.7) and (E.8) and keeping terms up to α_f, the one-loop mass is given by

$$\alpha_s \frac{1}{Z_2^{(0)}} m_1 - \alpha_s \epsilon_1 \frac{\sinh^3 m_{\text{tree}}}{6} - B_0 \sinh m_{\text{tree}} = -C, \tag{E.12}$$

where $Z_2^{(0)}$ is the tree-level wavefunction renormalisation:

$$\frac{1}{Z_2^{(0)}} = \left(1 - \frac{1 + \epsilon_{\text{tree}}}{2} \sinh^2 m_{\text{tree}} \right) \cosh m_{\text{tree}}. \tag{E.13}$$

At non-zero spatial momentum, the kinetic mass, m_{kin}, is defined by Equa-

tion (E.10). The tree-level pole condition is

$$
-\left(\sinh E - \frac{1 + \epsilon_{\text{tree}}}{6} \sinh^3 E \right)^2 + \left(\sin p_z + \frac{1 + \epsilon_{\text{tree}}}{6} \sin^3 p_z \right)^2 + m_0^2 = 0.
\tag{E.14}
$$

We now need to calculate the onshell derivative

$$
\left. \frac{\mathrm{d}^2}{\mathrm{d}p_z^2} \right|_{p_z=0} = \left[\frac{\partial^2}{\partial p_z^2} + 2 \frac{\partial E}{\partial p_z} \frac{\partial^2}{\partial p_z \partial E} + \left(\frac{\partial E}{\partial p_z} \right) \frac{\partial^2}{\partial E^2} \right]_{p_z=0}.
\tag{E.15}
$$

If we define

$$
F(E) = \sinh E - \frac{1 + \epsilon_{\text{tree}}}{6} \sinh^3 E,
\tag{E.16}
$$

$$
H(p_z) = \sin p_z + \frac{1 + \epsilon_{\text{tree}}}{6} \sin^3 p_z,
\tag{E.17}
$$

and note that $H(0) = 0$ and

$$
\left. \frac{\partial E}{\partial p_z} \right|_{p_z=0} = 0, \qquad \left. \frac{\partial H}{\partial p_z} \right|_{p_z=0} = 1,
\tag{E.18}
$$

then we obtain

$$
\left[\left(-F \frac{\partial F}{\partial E} \right) \left(\frac{\partial^2 E}{\partial p_z^2} \right) + \left(\frac{\partial H}{\partial p_z} \right)^2 \right]_{p_z=0} = 0.
\tag{E.19}
$$

Thus the tree-level kinetic mass is

$$
m_{\text{kin}} = \frac{1}{Z_2^{(0)}} m_0 = \left. \frac{\partial F}{\partial E} \right|_{p_z=0},
\tag{E.20}
$$

or, writing F explicitly,

$$
m_{\text{kin}} = \left(\sinh m_{\text{tree}} - \frac{1 + \epsilon_{\text{tree}}}{6} \sinh^3 m_{\text{tree}} \right)
$$
$$
\times \left(1 - \frac{1 + \epsilon_{\text{tree}}}{2} \sinh^2 m_{\text{tree}} \right) \cosh m_{\text{tree}}.
\tag{E.21}
$$

Requiring $m_{\text{kin}} = m_{\text{tree}}$ gives us the expression for ϵ_{tree} in Equation (6.35).

E.2   Wavefunction renormalisation

The wavefunction renormalisation is defined through the residue of the quark propagator at the single particle pole

$$\int_{-\pi}^{\pi} \frac{\mathrm{d}p_0}{2\pi} e^{ip_0 t} G(p_0, \mathbf{0}) = Z_2 e^{-mt} \frac{1 + \gamma_0}{2} + \ldots, \tag{E.22}$$

where the ellipses stand for poles corresponding to more complicated bound state and multi-particle states. I use the variable transformation $z = e^{ip_0}$ and write the propagator as $G(p) = g(z)/f(z)$, so that the integral becomes

$$\oint \frac{\mathrm{d}z}{2\pi i} z^{t-1} \frac{g(z)}{f(z)}. \tag{E.23}$$

The residue of the pole at $p_0 = im$, or $z = z_1$, is

$$e^{-mt} \left(\frac{g(z)}{z f'(z)} \right)_{z=z_1}. \tag{E.24}$$

Using the chain rule, the denominator in this expression is

$$z f' = z \frac{\mathrm{d}f}{\mathrm{d}z} = -i \frac{\mathrm{d}f}{\mathrm{d}p_0} = -\frac{\mathrm{d}f}{\mathrm{d}E}. \tag{E.25}$$

Now, for the HISQ propagator,

$$f(z) = ((B_0 - K_0)\sinh E + m_0 - C)\left((K_0 - B_0)\sinh E + m_0 - C\right), \tag{E.26}$$

so

$$z f'|_{z=z_1} = 2(m_0 - C)\left(\cosh E - \frac{1 + \epsilon}{2} \sinh^2 E \cosh E \right.$$
$$\left. + i \frac{\mathrm{d}}{\mathrm{d}p_0} (iB \sin p_0 + C) \right). \tag{E.27}$$

The residue is therefore

$$
\text{Res} = \frac{e^{-mt}}{2}(1 + \gamma_0)\left[\left(1 - \frac{1 + \epsilon}{2}\sinh^2 m\right)\cosh m + i\frac{\mathrm{d}}{\mathrm{d}p_0}\left(iB\sin p_0 + C\right)\right]^{-1},
$$

(E.28)

and so the wavefunction renormalisation is

$$
Z_2^{-1} = \left(1 - \frac{1 + \epsilon}{2}\sinh^2 m\right)\cosh m + i\frac{\mathrm{d}}{\mathrm{d}p_0}\left(iB\sin p_0 + C\right).
$$

(E.29)

At tree-level, this expression reduces to $Z_2^{(0)}$, given in Equation (6.37). The one-loop wavefunction renormalisation, $Z_2^{(1)}$, is given by

$$
\frac{1}{Z_2^{(1)}} = \frac{1}{Z_2^{(0)}}\left\{1 - \alpha_s\epsilon_1\frac{Z_2^{(0)}}{2}\cosh m_{\text{tree}}\sinh^2 m_{\text{tree}} + i\frac{\mathrm{d}}{\mathrm{d}p_0}\left(iB\sin p_0 + C\right)Z_2^{(0)}\right.
$$
$$
\left. + \alpha_s m_1\sinh m_{\text{tree}}\left[1 - \frac{1 + \epsilon_{\text{tree}}}{2}\left(2\cosh^2 m_{\text{tree}} + \sinh^2 m_{\text{tree}}\right)\right]Z_2^{(0)}\right\}.
$$

(E.30)

For massless HISQ with zero spatial momentum, we see that the one-loop wavefunction renormalisation becomes

$$
\frac{1}{Z_2^{(1)}} = -B_0 + i\frac{\mathrm{d}C}{\mathrm{d}p_0},
$$

(E.31)

since $m_{\text{tree}} = m_0 = 0$, $\epsilon_{\text{tree}} = 0$ and $Z_2^{(0)} = 1$.

Bibliography

[1] E. Gulez *et al.*, "B meson semileptonic form factors from unquenched lattice QCD," *Phys. Rev. D* **73** (2006) 074502.

[2] Heavy Flavor Averaging Group, "Averages of b-hadron and c-hadron properties at the end of 2007,". arXiv:0808.1297, online update: http://www.slac.stanford.edu/xorg/hfag.

[3] C.T.H. Davies *et al.*, "High–precision lattice QCD confronts experiment," *Phys. Rev. Lett.* **92** (2004) 022001.

[4] H. Trottier, "Higher-order perturbation theory for highly-improved actions," *Nucl. Phys. B (Proc. Suppl.)* **129** (2004) 142.

[5] A.G. Hart *et al.*, "The b quark mass from lattice nonrelativistic QCD," *PoS LAT2010* (2010) . arXiv:1010.6238.

[6] E. Follana *et al.*, "High precision determination of the π, K, D and D_s decay constants from lattice QCD," *Phys. Rev. Lett.* **100** (2008) 062002.

[7] A. Bazavov *et al.*, "The D_s and D^+ leptonic decay constants from lattice QCD," *PoS LAT2009* (2009) . arXiv:0912.5221.

[8] K. (Particle Data Group), "2010 Review of Particle Physics," *J. Phys. G* **37** (2010) 075021.

[9] M. Sevilla, "Semileptonic b and charm decays with babar," *EPS-HEP2011* (2011) . Talk given at EPS-HEP 2011, available at http://indico.in2p3.fr/contributionDisplay.py?sessionId=2& contribId=30&confId=5116.

[10] E. Gamiz, "B and D mesons on the lattice," *Nucl. Phys. B (Proc. Suppl.)* **187** (2009) 229.

[11] A. Lee Personal communication, 2011.

[12] M.A. Nobes *et al.*, "Second order perturbation theory for improved gluon and staggered quark actions," *Nucl. Phys. (Proc. Suppl.)* **106** (2002) 838.

[13] E.H. Mueller Personal communication, 2009.

[14] T.C. Hammant *et al.*, "Radiative improvement of the lattice NRQCD action using the background field method and application to the hyperfine splitting of the quarkonium states," *Phys. Rev. Lett.* **107** (2011) 112002.

[15] K. Wilson, "Confinement of quarks," *Phys. Rev. D* **10** (1974) 2445.

[16] L. Storoni, *Lattice gauge actions: non-perturbative simulations of heavy hybrid states and perturbative calculations of lattice parameters.* PhD thesis, University of Cambridge, 2002.

[17] R. Gupta, "Introduction to lattice QCD,". arXiv:hep-lat/9807028.

[18] H.B. Nielsen and M. Ninomiya, "Absence of neutrinos on a lattice," *Nucl. Phys. B* **185** (1981) 20.

[19] T. DeGrand and C. DeTar, *Lattice methods for quantum chromodynamics.* World Scientific, 2006.

[20] J. Smit, *Introduction to quantum fields on a lattice.* Cambridge lecture notes in physics. CUP, 2002.

[21] S. Sharpe, "Rooted staggered fermions: good, bad or ugly?," *PoS LAT2006* (2006) . arXiv:hep-lat/0610094.

[22] A. Bazavov *et al.*, "Full nonperturbative QCD simulations with 2+1 flavors of improved staggered quarks," *Rev. Mod. Phys.* **82** (2010) 1349.

[23] E. Follana *et al.*, "Highly improved staggered quarks on the lattice with applications to charm physics," *Phys. Rev. D* **75** (2007) 054502.

[24] M. Golterman, "QCD with rooted staggered fermions," *PoS CONFINEMENT2008* (2008) . arXiv:0812.3110.

[25] C. McNeile *et al.*, "High-precision c and b masses, and QCD coupling from current-current correlators in lattice and continuum QCD," *Phys. Rev. D* **82** (2010) 034512.

[26] E.B. Gregory *et al.*, "Precise B, B_s and B_c meson spectroscopy from full lattice QCD," *Phys. Rev. D* **83** (2011) 014506.

[27] G.P. Lepage, "Redesigning lattice QCD,". arXiv:hep-lat/9607076.

[28] M. Alford *et al.*, "Lattice QCD on small computers," *Phys. Lett. B* **361** (1995) 87.

[29] G.P. Lepage and P.B. Mackenzie, "On the viability of lattice perturbation theory," *Phys. Rev. D* **48** (1993) 2250.

[30] S.J. Brodsky, G.P. Lepage, and P.B. Mackenzie, "On the elimination of scale ambiguities in perturbative quantum chromodynamics," *Phys. Rev. D* **28** (1983) 228.

[31] K. Hornbostel, G.P. Lepage, and C. Morningstar, "Scale setting for α_s beyond leading order," *Phys. Rev. D* **67** (2002) 034023.

[32] M. Peter, "Static quark-antiquark potential in QCD to three loops," *Phys. Rev. Lett.* **78** (1997) 602.

[33] M. Peter, "The static potential in QCD - a full two-loop calculation," *Nucl. Phys. B* **501** (1997) 471.

[34] Y. Schroeder, "The static potential in QCD to two loops," *Phys. Lett. B* **447** (199) 321.

[35] M. Luescher and P. Weisz, "On-shell improved lattice gauge theories," *Commun. Math. Phys.* **97** (97) 59.

[36] M. Luescher and P. Weisz, "On-shell improved lattice gauge theories," *Commun. Math. Phys.* **98** (1985) 433.

[37] M. Luescher and P. Weisz, "Computation of the action for on-shell improved lattice gauge theories at weak coupling," *Phys. Lett. B* **158** (1985) 250.

[38] Zh. Hao *et al.*, "Unquenching effects on the coefficients of the Lüscher-Weisz action," *Phys. Rev. D* **76** (2007) 034507.

[39] G.P. Lepage, "Flavor-symmetry restoration and Symanzik improvement for staggered quarks," *Phys. Rev. D* **59** (1999) 074502.

[40] E. Braaten, "Introduction to the NRQCD factorization approach to heavy quarkonium,". arXiv:hep-ph/9702225.

[41] R.R. Horgan *et al.*, "Moving NRQCD for heavy-to-light form factors on the lattice," *Phys. Rev. D* **80** (2009) 074505.

[42] W.E. Caswell and G.P. Lepage, "Effective lagrangians for bound state problems in QED, QCD, and other field theories," *Phys. Lett. B* **167** (1986) 437.

[43] G.P. Lepage and B.A. Thacker, "Effective lagrangians for simulating of heavy quark systems," *Nucl. Phys. B (Proc. Suppl.)* **4** (1988) 199.

[44] B.A. Thacker and G.P. Lepage, "Heavy-quark bound states in lattice QCD," *Phys. Rev. D* **43** (1991) 196.

[45] G.P. Lepage *et al.*, "Improved nonrelativistic QCD for heavy-quark physics," *Phys. Rev. D* **46** no. 9, (1992) 4052.

[46] G.T. Bodwin, E. Braaten, and G.P. Lepage, "Rigorous QCD analysis of inclusive annihilation and production of heavy quarkonium," *Phys. Rev. D* **51** (1995) 1125.

[47] E.H. Mueller, *Heavy-to-light decays on the lattice.* PhD thesis, University of Edinburgh, 2009.

[48] C. Itzykson and J-B. Zuber, *Quantum field theory.* Dover, 1980.

[49] C.T.H. Davies and B.A. Thacker, "Heavy-quark renormalization parameters in nonrelativistic QCD," *Phys. Rev. D* **45** (1992) 915.

[50] M. Wingate *et al.*, "Heavy-light mesons with staggered light quarks," *Phys. Rev. D* **67** (2003) 054505.

[51] M. Beneke, "Renormalons," *Phys. Reports* **317** (1999) 1.

[52] G. 't Hooft, *Can we make sense out of "quantum chromodynamics"*, pp. 943–971. No. 15 in The subnuclear series. Plenum Press, 1977.

[53] E. Braaten and Y. Chen, "Renormalons in electromagnetic annihilation decays of quarkonium," *Phys. Rev. D* **57** (1998) 4236.

[54] F.J. Dyson, "Divergence of perturbation theory in quantum electrodynamics," *Phys. Rev.* **85** (1952) 631.

[55] I.I. Bigi and N.G. Uraltsev, "Anathematizing the Guralnik-Manohar bound for $\overline{\Lambda}$," *Phys. Lett. B* **321** (1994) 412.

[56] M. Beneke and V.M. Braun, "Heavy quark effective theory beyond perturbation theory: renormalons, the pole mass and residual mass term," *Nucl. Phys. B* **426** (1994) 301.

[57] M. Neubert and C.T. Sachrajda, "Cancellation of renomalon ambiguities in the heavy quark effective theory," *Nucl. Phys. B* **438** (1995) 235.

[58] M. Luke, A.V. Manohar, and M.J. Savage, "Renormalons in effective field theories," *Phys. Rev. D* **51** (1995) 4924.

[59] G.T. Bodwin and Y. Chen, "Renormalon ambiguities in NRQCD operator matrix elements," *Phys. Rev. D* **60** (1999) 054008.

[60] V.A. Novikov, M.A. Shifman, A.I. Vainshtein, and V.I. Zakharov, "Wilson's operator expansion: can it fail?," *Nucl. Phys. B* **249** (1985) 445.

[61] F. David, "The operator product expansion and renormalons: a comment," *Nucl. Phys. B* **263** (1986) 637.

[62] G. Martinelli and C.T. Sachrajda, "Renormalons and the heavy quark effective theory," *Phys. Lett. B* **354** (1995) 423.

[63] G.M. von Hippel, "Life on the lattice.". http://latticeqcd.blogspot.com/ Retrieved 23/09/2009.

[64] G.P. Lepage, "A new algorithm for adaptive multidimensional integration," *J Comp Phys* **27** (1978) 192.

[65] M. Luescher and P. Weisz, "Efficient numerical techniques for perturbative lattice gauge theory computations," *Nucl. Phys. B* **266** (1986) 309.

[66] A. Hart *et al.*, "Automatically generating Feynman rules for improved lattice field theories," *J. Comp. Phys.* **209** (2005) 340.

[67] A. Hart *et al.*, "Automated generation of lattice QCD Feynman rules," *Comp. Phys. Commun.* **180** (2009) 2698.

[68] S. Capitani and G. Rossi, "The use of schoonschip and form in perturbative lattice calculations,". arXiv:hep-lat/9504014.

[69] A. Bode and H. Panagopoulos, "The three-loop beta-function of QCD with the clover action," *Nucl. Phys. B* **625** (2002) 198.

[70] C. Christou *et al.*, "The three-loop β function of $SU(N)$ lattice gauge theories with wilson fermions," *Nucl. Phys. B* **525** (1998) 387.

[71] C.J. Morningstar, "Heavy quark self-energy in nonrelativistic lattice QCD," *Phys. Rev. D* **48** (1993) 2265.

[72] G.M. von Hippel, "TaylUR, an arbitrary-order diagonal automatice differentiation package for Fortran 95," *Comput. Phys. Commun* **174** (2006) 569.

[73] G.M. von Hippel, "TaylUR 3, a multivariate aribitrary-order automatic differentation package for Fortran 95,". arXiv:0910.5111.

[74] G. 't Hooft, "A property of electric and magnetic flux in non–abelian gauge theories," *Nucl. Phys. B* **153** (1979) 141.

[75] Q. Mason, "Treatise on colour factors." Unpublished, 2002.

[76] S. Weinberg, *The quantum theory of fields*, vol. II. CUP, 2005.

[77] M. Luescher and P. Weisz, "Background field technique and renormalization in lattice gauge theory," *Nucl. Phys. B* **452** (1995) 213.

[78] M. Luescher and P. Weisz, "Computation of the relation between the bare lattice coupling and the $\overline{MS}$ coupling in $SU(N)$ gauge theories to two loops," *Nucl. Phys. B* **452** (1995) 234.

[79] T.C. Hammant *et al.*, "Improved automated lattice perturbation theory in background field gauge," *PoS LAT2010* (2010) . arXiv:1011.2696.

[80] M. Luescher and P. Weisz, "Coordinate space methods for the evaluation of Feynman diagrams in lattice field theories," *Nucl. Phys. B* **445** (1995) 429.

[81] M. Luescher and P. Weisz, "Two-loop relation between the bare lattice coupling and the $\overline{MS}$ coupling in pure $SU(N)$ gauge theories," *Phys. Lett. B* **349** (1995) 165.

[82] S. Bethke, "The 2009 world average of α_s," *Eur. Phys. J. C* **64** (2009) 689.

[83] W. Celmaster and R. Gonsalves, "Quantum-chromodynamics perturbation expansions in a coupling constant renormalized by momentum-space subtraction," *Phys. Rev. Lett.* **42** (1979) 1435.

[84] C. Bernard *et al.*, "QCD spectrum with three quark flavors," *Phys. Rev. D* **64** (2001) 054506.

[85] A. Gray *et al.*, "The Upsilon spectrum and m_b from full lattice QCD," *Phys. Rev. D* **72** (2005) 094507.

[86] A. Hart, R.R. Horgan, and L.C. Storoni, "Perturbation theory vs. simulation for tadpole improvement factors in pure gauge theories," *Phys. Rev. D* **70** (2004) 034501.

[87] C.J. Morningstar, "Radiative corrections to the kinetic couplings in nonrelativistic lattice QCD," *Phys. Rev. D* **50** (1994) 5902–5911.

[88] L. Khomskii, *Perturbation theory for quarks and currents in moving NRQCD on a lattice.* PhD thesis, University of Cambridge, 2008.

[89] E. Gulez, J. Shigemitsu, and M. Wingate, "One-loop matching of the heavy-light A_0 and V_0 currents with NRQCD heavy and improved naive light quarks," *Phys. Rev. D* **69** (2004) 074501.

[90] E.H. Mueller *et al.*, "Radiative corrections to the m(oving)NRQCD action and heavy-light operators," *PoS LAT2009* (2009) . arXiv:0909.5126.

[91] E. Barberio, "Inclusive semileptonic b decays,". arXiv:hep-ex/0605098.

[92] K.G. Chetyrkin *et al.*, "Charm and bottom quark masses: An update," *Phys. Rev. D* **80** (2009) 074010.

[93] R. Dowdall, "Tuned mass and ground state energy for calculating m_b on coarse ensemble." Personal communication, 2011.

[94] W. Dimm, G.P. Lepage, and P.B. Mackenzie, "Nonperturbative 'lattice perturbation theory'," *Nucl. Phys. B (Proc. Suppl.)* **42** (1995) 403.

[95] Q. Mason *et al.*, "Accurate determinations of $alpha_s$ from realistic lattice QCD," *Phys. Rev. Lett.* **95** (2005) 052002.

[96] R. Horgan Personal communication, 2011.

[97] K.Y. Wong, H.D. Trottier, and R.M. Woloshyn, "Perturbative Wilson loops from unquenched Monte Carlo simulations at weak couplings," *Phys. Rev. D* **73** (2006) 094512.

[98] C.T.H. Davies *et al.*, "Precise determination of the lattice spacing in full lattice QCD," *Phys. Rev. D* **81** (2010) 034506.

[99] K. Melnikov and T. van Ritbergen, "The three–loop relation between the $\overline{MS}$ and the pole quark masses," *Phys. Lett. B* **482** (2000) 99.

[100] S. Narison, "Gluon condensates and precise $m_{b,c}$ from QCD-moments to order $alpha_s^3$,". arXiv:1105.2922.

[101] S. Narison, "Gluon condensates and $m_b(m_b)$ from QCD-exponential moments at higher orders,". arXiv:1105.5070.

[102] P. Dimopoulos *et al.*, "Lattice QCD determination of m_b, f_B and f_{B_s} with twisted mass Wilson fermions,". arXiv:1107.1441.

[103] B. Blossier *et al.*, "B meson spectrum and decay constant from nf=2 simulations," *PoS LAT2010* . arXiv:1012.1357.

[104] N. Cabibbo, "Unitary symmetry and leptonic decays," *Phys. Rev. Lett.* **10** (1963) 531.

[105] M. Kobayashi and T. Maskawa, "CP violation in the renormalizable theory of weak interaction," *Prog. Theor. Phys.* **49** (1973) 652.

[106] L. Wolfenstein, "Parameterization of the Kobayashi-Maskawa matrix," *Phys. Rev. Lett.* **51** (1983) 1945.

[107] S. Collins *et al.*, "Scaling and further tests of heavy meson decay constant determinations from nonrelativistic qcd," *Phys. Rev. D* **63** (2001) 034505.

[108] M. Wingate *et al.*, "The B_s and D_s decay constants in 3 flavor lattice QCD," *Phys. Rev. Lett.* **92** (2004) 162001.

[109] M. Wingate *et al.*, "Progress calculating decay constants with NRQCD and AsqTad actions,". hep-lat/0309092.

[110] R.Barlow, "Experimental status of $B \to \tau\nu$ and $B \to \tau\nu(\gamma)$," *CKM 2010* (2011) . arXiv:1102.1267.

[111] J. Shigemitsu, "Progress in lattice QCD relevant for flavor physics," *CKM 2010* (2011) . arXiv:1102.0716.

[112] C.J. Morningstar and J. Shigemitsu, "One-loop matching of lattice and continuum heavy-light axial vector currents using NRQCD," *Phys. Rev. D* **57** (1998) 6741.

[113] C.J. Morningstar and J. Shigemitsu, "Perturbative matching of lattice and continuum heavy-light currents with NRQCD heavy quarks," *Phys. Rev. D* **59** (1999) 094504.

[114] J. Shigemitsu, "HISQ selfenergy." Unpublished, 2006.

[115] I.T. Drummond *et al.*, "One loop calculation of the renormalized anisotropy for improved anisotropic gluon actions on a lattice," *Phys. Rev. D* **66** (2002) 094509.

[116] M.E. Peskin and D.V. Shroeder, *An introduction to quantum field theory.* Addison Wesley, 1995.

Publications

- "Radiative improvement of the lattice NRQCD action using the background field method and application to the hyperfine splitting of quarkonium states"

T.C. Hammant, A.G. Hart, G.M. von Hippel, R.R. Horgan and C.J. Monahan
Phys. Rev. Lett 107 (2011) 112002. arXiv:1105.5309

- "Improved automated lattice perturbation theory in background field gauge"

T.C. Hammant, R.R. Horgan, C.J. Monahan, A.G. Hart, E.H. Müller, A. Gray, K. Sivalingham and G.M. von Hippel
PoS **LAT2010** arXiv:1011.2696

- "The b quark mass from lattice nonrelativistic QCD"

A.G. Hart, G.M. von Hippel, R.R. Horgan, A. Lee and C.J. Monahan
PoS **LAT2010** arXiv:1011.2696

- "Radiative corrections to the m(oving)NRQCD action and heavy-light operators"

E.H. Müller, C.T.H. Davies, A.G. Hart, G.M. von Hippel, R.R. Horgan, I.D. Kendall, A. Lee, S. Meinel, C.J. Monahan and M. Wingate
PoS **LAT2009** arXiv:0909.5126